

Physik-Department
der Technischen Universität München
Lehrstuhl für Biophysik E22

Generic and Specific Cell Adhesion: Investigations of a Model System by Micro-Interferometry

Stefanie Gönnenwein

Vollständiger Abdruck der von der Fakultät für Physik der Technischen Universität München zur Erlangung des akademischen Grades eines

Doktors der Naturwissenschaften (Dr. rer. nat.)

genehmigten Dissertation.

Vorsitzender: Univ.-Prof. Dr. M. Kleber

Prüfer der Dissertation:

1. Univ.-Prof. Dr. E. Sackmann
2. Hon.-Prof. Dr. W. Baumeister

Die Dissertation wurde am 19.02.2003 bei der Technischen Universität München eingereicht und durch die Fakultät für Physik am 01.04.2003 angenommen.

für meine Eltern

Contents

Zusammenfassung	1
Introduction	5
1 Dual Wavelength Technique	9
1.1 Introduction, Motivation	9
1.2 RICM	9
1.2.1 Reflection Interference	9
1.2.2 Antiflex Technique	11
1.2.3 Reconstruction of the Height Profile	12
1.2.4 RICM Setup	14
1.2.5 Dual Wavelength Technique	16
1.3 Outlook	20
2 Fluctuations of Membranes	22
2.1 Introduction	22
2.2 Theory	24
2.2.1 Generic Forces	25
2.2.2 Total Interaction Potential	26
2.3 Materials and Methods	30
2.3.1 Giant Vesicles	30
2.3.2 Substrate Preparation	30
2.3.3 RICM	31
2.3.4 Evaluation	31
2.4 Results	36
2.4.1 Single-Component Membrane	36
2.4.2 Multi-Component Membrane	38
2.4.3 Change of the Specific Weight	43
2.4.4 Passivation of the Substrate	43
2.5 Discussion	44
2.6 Conclusions	46

3	Model System for Cell Plasma Membranes	48
3.1	Introduction	48
3.1.1	Integrins	51
3.1.2	RGD Peptides	52
3.1.3	Outline	53
3.2	Theory of Diffusion	53
3.2.1	The Hydrodynamic Model	54
3.2.2	Diffusion in Supported Membranes	55
3.3	Materials and Methods	56
3.3.1	Glass Substrates	57
3.3.2	Silanization of the Glass Substrates	57
3.3.3	Cellulose Films	57
3.3.4	Reconstitution of Integrins	58
3.3.5	Supported Planar Bilayers	59
3.3.6	Blocking Non-Specific Adhesion	60
3.3.7	RGD Lipid	60
3.3.8	Fluorescence Microscopy	60
3.3.9	Fluorescence Recovery After Photobleaching (FRAP)	60
3.3.10	Cryo-Electron Microscopy	62
3.4	Results	62
3.4.1	Reconstitution of $\alpha_{IIb}\beta_3$ Integrins into Lipid Bilayers	62
3.4.2	Determination of Integrin and Lipid Concentrations	63
3.4.3	Formation of Planar Membranes with Integrins	64
3.4.4	Tunable Model System	66
3.4.5	Determination of the Lateral Diffusion Constant D_T	67
3.4.6	Determination of the Frictional Coupling	70
3.4.7	Functionality of the Integrins	72
3.5	Conclusions	73
4	Cell Adhesion Studies	75
4.1	Introduction	75
4.2	State of Knowledge	76
4.3	Theory of Vesicle Adhesion	79
4.3.1	Bending Elastic Theory	79
4.3.2	Lock-and-Key Forces	83
4.3.3	Repulsion by Repellers and Ligands	84
4.4	Materials and Methods	86
4.4.1	Giant Vesicles	86
4.4.2	Adhesion Assay	86
4.5	Results and Discussion	87
4.5.1	Control Experiments	87
4.5.2	Free Adhesion Energy Determination for Giant Vesicles	88

4.5.3	Specific Adhesion Energy of the Integrin-RGD Binding	96
4.6	Conclusions on the Adhesion Studies	98
4.7	Outlook: Controlling the Adhesion Area	98
5	Magnetic Tweezers	101
5.1	Introduction	101
5.2	Magnetic Tweezers	102
5.2.1	Setup	104
5.2.2	Force transducers	104
5.2.3	Characterization	107
5.2.4	Calibration	107
5.3	Materials and Methods	108
5.3.1	RGD-containing Vesicles on Integrin-exhibiting Substrates . .	108
5.3.2	Sialyl-Lewis ^X -containing Vesicles on E-Selectin Substrates . .	109
5.3.3	Attachment of Beads	109
5.3.4	Laser Confocal Scanning Microscopy (LCSM)	110
5.4	Magnetic Tweezers Experiments	110
5.4.1	Membrane Tension	111
5.4.2	Contact Angle	112
5.4.3	Vertical Force	112
5.4.4	Unbinding Experiments	114
5.5	Conclusions	122
5.6	Outlook	123
	Appendix	125
	Bibliography	129
	Danke	143
	Curriculum Vitae	144
	List of Publications	145

Zusammenfassung

Ziel der Arbeit war die Entwicklung einer Methode zur Messung von Adhäsionskräften zwischen Rezeptoren und konjugierten Liganden unter bioanalogen Bedingungen. Das wesentliche Ergebnis ist eine Technik, die es erlaubt absolute Abstände zwischen Festkörperoberflächen und darüber schwebender oder spezifisch adhärrierender Membranen zu messen. Desweiteren konnte ein Modellsystem auf der Basis festkörpergestützter Membranen etabliert werden, das die Funktion der Rezeptoren und Liganden deutlich weniger stört als bisherige Systeme.

Im ersten Teil der Arbeit wird die Methode der Reflektions-Interferenz-Kontrast Mikroskopie (RIKM) eingeführt, die es ermöglicht, vertikale Abstände von Objekten wie Zellen, Vesikeln oder Kolloiden von Substratoberflächen zu messen. Durch Hinzunahme einer zweiten Wellenlänge konnte die Methode wesentlich verbessert werden, erstmals können absolute Abstände mit einer Genauigkeit von 5 nm bestimmt werden. Im Gegensatz zu der bisher etablierten, einfacheren RIKM mit nur einer Wellenlänge, muss die Form der zu analysierenden Objekte bei der Zweifarben-RIKM nicht bekannt sein, da die Randbedingungen eine eindeutige Phasenrelation ergeben. Durch diese Erweiterung konnten Höhen von Latexkugeln über einem Substrat zwischen 2 und ca. 1000 nm eindeutig gemessen werden. Das erlaubt etwa, die Dicken von weichen, durchsichtigen Filmen aus biologischen Polyelektrolyten zu bestimmen, indem Kolloide auf die Oberflächen gebracht werden und ihre Höhe gemessen wird. Weiterhin können Abstandsfluktuationen von Membranen schwach adhärrierter Vesikel direkt im Ortsraum analysiert werden. Solche Messungen ermöglichen eine detaillierte Untersuchung der physikalisch relevanten Aspekte der Adhäsion.

Riesenvesikel stellen ein relativ einfaches Modell einer Zelle dar, sie bestehen aus einer mit Flüssigkeit gefüllten Phospholipidmembran. Im Gegensatz zu Zellen kann die Membranzusammensetzung im Experiment gezielt kontrolliert und variiert werden. Daher können die Einflüsse der verschiedenen Membrankomponenten auf das Verhalten der Membran an Oberflächen aufgeklärt werden. Dies erlaubt es, den Einfluss der schwachen Adhäsion, also der durch generische Kräfte wie Gravitation und van der Waals Anziehung vermittelten Adhäsion, zu untersuchen.

Zusätzlich zu der Motivation von der biologischen Seite haben diese Modellmembranen eine Vielzahl von einzigartigen Merkmalen. Ihre Fluidität, Zweidimensionalität und Biegesteifigkeit machen sie zu einem Material mit faszinierenden Eigen-

schaften. Im Rahmen dieser Arbeit konnte gezeigt werden, dass die Helfrich Repulsion zu einer lateralen Phasentrennung in der Membran führt. Dabei wurde die Theorie des Phasenübergangs zwischen adhärenierten und freien Membranen erstmals durch Echtzeitexperimente an einkomponentigen Vesikeln (die Membran besteht nur aus Phospholipiden einer Sorte) bestätigt. Die Beobachtungen zeigen, dass sich die Membran statistisch um einen mittleren Höhenwert bewegt. Genau dieses Verhalten war für Membranen vorhergesagt worden, wobei sogar die Breite und Position der Höhenverteilung und das daraus rekonstruierte Wechselwirkungspotential zwischen Membran und Substrat übereinstimmen. Dahingegen wurde für mehrkomponentige Membranen, in die zusätzlich beispielsweise Lipopolymere mit Polyethylenglycol (PEG) Kopfgruppen oder Cholesterol eingebettet sind, eine bimodale Verteilung nachgewiesen. In solchen Vesikeln fluktuiert die Membran um zwei verschiedene Höhen, die ca. 30 bis 40 nm voneinander entfernt sind. An jeder Stelle hat die Membran eine andere momentane Höhe, wohingegen die Höhenverteilung von identischen Membranen über der Zeit vergleichbar ist. Die Koexistenz von zwei freien Zuständen zeigt einen Phasenübergang erster Ordnung an, der in bisherigen Theorien nicht berücksichtigt wurde. Als mögliche Ursache kommt eine dynamische Phasenseparation in Membranen aus Lipidmischungen (beispielsweise zwischen lipopolymerreichen und -armen Regionen der Vesikelmembran) in Betracht, die durch eine entropisch bedingte Abstoßung zwischen der Festkörperoberfläche und den fluktuierenden Vesikeln bedingt ist (Helfrich Repulsion).

Um die rezeptorvermittelte Zelladhäsion zu untersuchen, wurden im zweiten Teil der Arbeit die Bindungseigenschaften des Rezeptors Integrin $\alpha_{IIb}\beta_3$ mit einem Oligopeptid mit der zyklischen Aminosäuresequenz Arg-Gly-Asp (RGD) wieder mittels des Vesikel-Modellsystems untersucht. Dazu kann das RGD-Peptid, das über einen Abstandshalter an ein Lipid gekoppelt ist, frei beweglich in die Vesikelmembran eingebaut werden. Um die repulsive Zellglykokalix zu modellieren, wurden zusätzlich PEG-Lipopolymere in die Vesikelmatrix inkorporiert. Die aus dem menschlichen Thrombozyten gewonnenen Integrine wurden in eine substratgestützte Lipidmembran eingebaut. Dabei konnte gezeigt werden, dass die großen Integrine in der Substratebene beweglich bleiben, wenn sie von ultradünnen und weichen Filmen aus Zellulose gestützt werden. Auf reinem Glas ist diese Beweglichkeit, die eine grundlegende Eigenschaft biologischer Materialien ist, nicht gegeben.

Mit Hilfe der RIKM lassen sich nun die Adhäsionseigenschaften der Riesenvesikel untersuchen und die freien Adhäsionsenergien messen. Es wurde beobachtet, dass die Adhäsionsenergie auf den Substraten mit beweglichen Integrinen um den Faktor 30 größer ist als auf den Substraten mit unbeweglichen Integrinen. Der große Unterschied lässt vermuten, dass die Integrine auf Glas teilweise denaturiert sind. Dahingegen gelang auf den Polymerfilmen, durch die parallele Messung der Rezeptordichte, eine Abschätzung der Bindungsenergie der Rezeptor-Ligand Paare von $10 k_B T$, in guter Übereinstimmung mit der Bindungskinetik. Außerdem konnte nachgewiesen werden, dass bereits eine kleine Konzentration von Repellermolekülen

(PEG im Fall des Modellsystems) die Adhäsionsenergie drastisch reduziert. Dies lässt sich quantitativ als Folge der osmotischen Druckdifferenz zwischen PEG-reicher Membran und PEG-armer Adhäsionszone verstehen.

Schließlich wurde versucht, die Kraft zu analysieren, die man benötigt, um einzelne Rezeptor-Ligand-Paare am Rand der Adhäsionsfläche der Vesikel abzureißen. Dazu wurden sogenannte magnetischen Pinzetten angewendet. Das sind magnetische Kolloide, die an die Vesikel angeheftet sind, und mit einem Magneten normal zur Adhäsionsebene nach oben gezogen werden können. Die Veränderung der Adhäsionsfläche kann in Echtzeit im RIKM beobachtet und die vertikalen Kräfte analysiert werden. Besonders bemerkenswert ist dabei, dass die ermittelten Abreißkräfte relativ klein sind. Außerdem stellt sich trotz wirkender Zugkraft ein Gleichgewicht ein, das heißt die Adhäsionsfläche verkleinert sich nicht weiter.

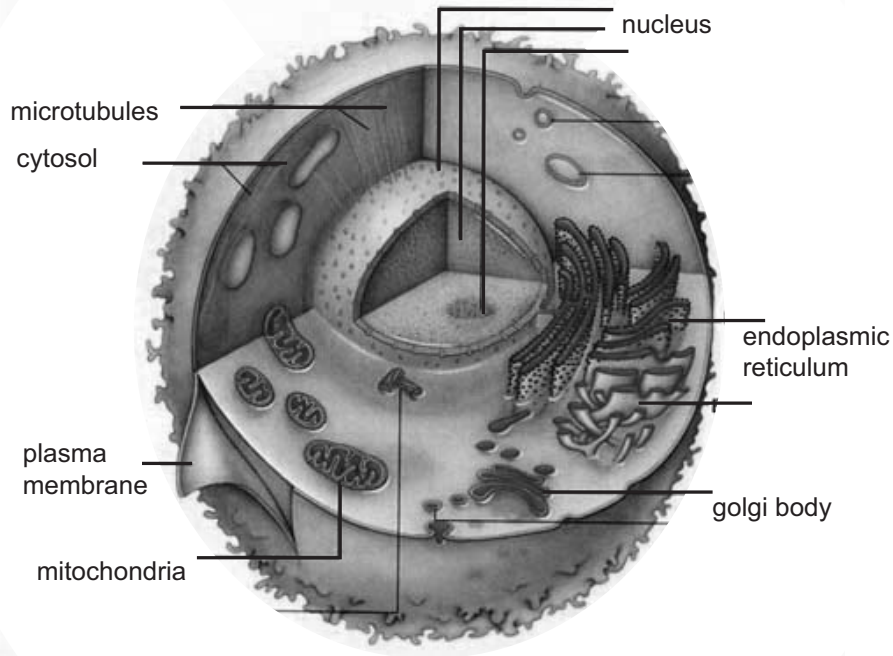
Introduction

Cells are the main building blocks of life. They are characterized by their ability to maintain an own metabolism and energy proliferation system. They can perform diverse functions such as differentiation, replication, signaling, self organization and adhesion (Lodish et al. 2000). All eukaryotic cells, no matter from which organism, are similar: they consist of a nucleus, many different organelles with well-defined functions, an intracellular liquid, the cytosol, and a cell plasma membrane (cf. Fig 1a). This flexible plasma membrane delimits the cell. It is made up of phospholipids, and hosts different glycolipids and proteins.

Cell adhesion is of vital importance in many processes in nature and will be the main focus in the following. For example, the formation of specific organs during the transformation of fertilized eggs into embryos or cycles of the immune response depend crucially on adhesion. Other examples are illnesses like cardiovascular diseases or the growth of metastases in cancer.

The perfection with which cells recognize target molecules is fascinating. For instance, the immune system can perfectly distinguish between "own" cells and "foreign" cells, since only the latter are attacked by antibodies upon their appearance in the human body. The high specificity of recognition between the receptors expressed at the cell surface and the adhesion molecules on the target cell is controlled by the lock-and-key force principle. This principle relies on a topologically and chemically complementary structure along the interfaces shared by the molecules (Wyman and Gill 1990). In addition to this specific attraction, a whole set of generic interactions is coming into play, e.g. van der Waals (vdW), electrostatic and polymeric interactions. To maintain the high adhesion specificity in spite of unspecific adhesion due to generic attractions, the cell is covered by a repulsive, brush-like polymer layer (Alberts et al. 1994). The so-called glycocalix is made up of carbohydrate-rich molecules which are reaching lengths of up to tens of nanometer. These molecules can diffuse freely on the surface of the cell, i.e. in the cell plasma membrane. They are surrounding or even hiding the specific receptors and cell adhesion molecules. A complex interplay between the above mentioned attractive and repulsive interactions as well as the elasticity of membranes leads to non-homogeneous adhesion areas between cells. Domains of weak adhesion, which are poor in receptor-ligand pairs, are coexisting with domains rich in adhesion molecules. Accordingly, the latter exhibit strong adhesion, forming so-called focal adhesion sites (FAS). These FAS

(a) eukaryotic cell



(b) model system of the giant vesicle

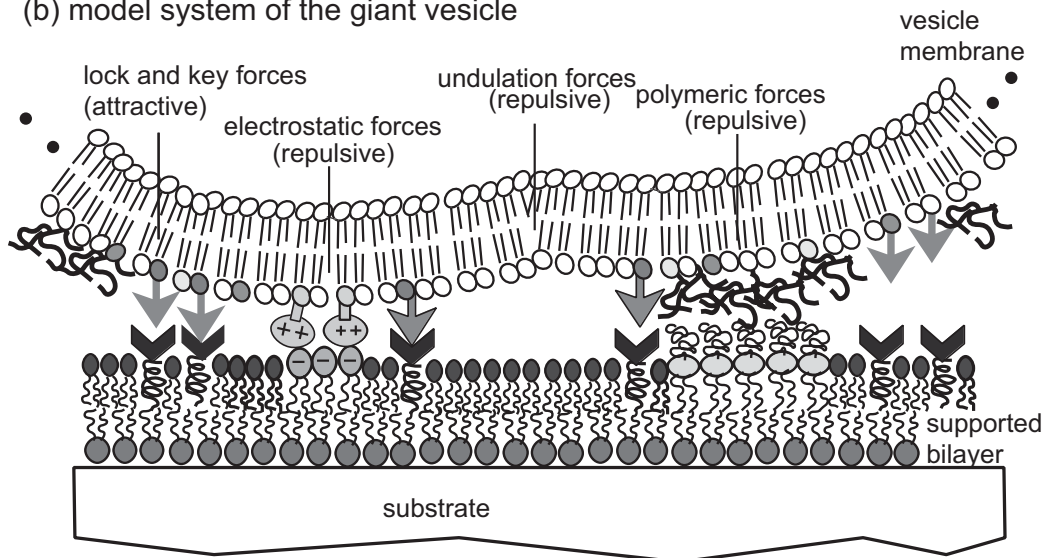


Figure 1: (a) Picture of an eukaryotic cell with nucleus, different organelles and the cell plasma membrane. (b) Schematic view of the model system of a giant lipid vesicle with incorporated ligands and lipopolymers. The substrate is covered by a solid supported bilayer, exhibiting receptors.

play a key role for cells, as they e.g. enable the signaling through the cell membrane in either direction: inside-out signaling and outside-in signaling. The signaling can be established by transmembrane proteins (for example integrins) which span the membrane, providing adhesion domains on either side of the membrane. The drastic reorganization of the membrane coupled actin-based cytoskeleton upon FAS appearance, such as the formation of actin bundles (stress fibers), further complicates the situation.

An amazingly large number of biological questions can be addressed from a physical point of view. For example, the two-dimensional lipid bilayers of the cell membrane exhibit a variety of unique properties like fluidity in two dimensions, elasticity, and fluctuation phenomena. The unbinding transition of a membrane from another membrane was shown to be governed by an interplay of molecular forces and entropic interactions (Helfrich 1978). Phase separations within the cell membrane occur in nature and the adhesion process of a cell can be described as a first order wetting transition (Guttenberg et al. 2001). Experimental variation of mechanical and thermodynamical properties shall help to elucidate their influence in the complex adhesion process. The application of mechanical loads on formed specific bonds and their resistance or adaption to the acting forces are further intriguing questions.

To study the physical basis of cell adhesion, model systems exhibiting key elements of the cell surface were designed. Giant phospholipid vesicles are a prominent example of such artificial test cells, allowing to observe the adhesion area in light microscopy. Lipid vesicles are a powerful tool because the composition of their membrane can be varied, allowing to elucidate the influence of different parameters on e.g. the adhesion process, cf. Fig. 1b. Since the vesicles are hollow capsules, filled with a liquid to stabilize them, all the observed processes occur without any active regulation of the cell or the cytoskeleton. Further, the model system for instance makes it possible to study the generic adhesion of fluid membranes, i.e. the interaction in absence of specific lock-and-key forces. This generic interaction is omnipresent and thus an important mosaic part in understanding the physics of cell adhesion.

To obtain a more realistic cell model, receptor or ligand proteins can be attached to the vesicle membrane. Thus, receptor mediated adhesion can be investigated on such test cells. The generic long range repulsion of the glycocalyx is typically modelled by embedding lipopolymers in the test cell membrane. Target cells or target tissues, i.e. the sites where the test cells are adhering to, are solid substrates, which can be build up to model a cell surface in a very realistic way (Dustin 1997). Solid supported bilayers with incorporated proteins have been demonstrated to be able to attach receptors in a biofunctional way and exhibit key characteristics of cell surfaces (Brian and McConnell 1984, Sackmann 1996), cf. Fig. 1b. Upon supporting these bilayers on ultrathin polymer films, the mobility of lipid anchored receptors within these layers can be increased (Kühner et al. 1994), and even the mobility of large transmembrane receptors like integrins can be accomplished as demonstrated in this thesis.

Integrins are a family of large cell surface receptors that attach cells to the extracellular matrix. The matrix exerts control over the cells and the signaling is primarily mediated by integrins. Integrins are found in many animal species, ranging from sponges to mammals. The specific integrin $\alpha_{IIb}\beta_3$ considered in the following is the main receptor of human blood platelets and can therefore be purified from human blood in large amounts. It plays a crucial role in thrombosis and haemostasis. Upon an injury of a blood vessel wall, blood platelets adhere. The thereon activated $\alpha_{IIb}\beta_3$ integrins trigger the adhesion of fibrinogen and fibronectin from the blood serum. Integrin $\alpha_{IIb}\beta_3$ binds specifically to the amino acid sequence Arg-Gly-Asp (RGD)-sequence of different serum proteins. From a medical point of view, a detailed understanding of the integrin-binding properties is extremely desirable, since blocking the binding opens up possibilities to treat cardiovascular diseases. On the other hand, controlling and promoting cell adhesion should help to improve medical issues such as prosthesis and implant acceptance in the human body.

Physical insights from the model system can be obtained by varying mechanical or thermodynamical properties of the vesicle membrane and studying their influence on the adhesion dynamics and strength. For example it could be shown that already small amounts of repeller molecules (1 mol%) in the vesicle membrane reduces the adhesion energy drastically. Further, the presented model system enables quantitative unbinding experiments of the vesicle from the substrate by magnetic tweezers. Thereby, an ensemble of receptor-ligand pairs in a bioanalogue environment is exposed to a counteracting point force. Cooperative phenomena, similar as those relevant in the unbinding of cells, are expected to play an important role there.

The membrane model studies presented here rely on micro-interferometry, which is a versatile technique to measure relative vertical distances h between the substrate and the vesicle membrane. By upgrading the existing setup, an unambiguous and absolute height determination down to the nanometer range could be obtained. This enables one to investigate heterogeneous adhesion domains of cells or vesicles and their lateral variation in time, or their response to an external force.

Chapter 1

Dual Wavelength Technique

1.1 Introduction, Motivation

Micro-interferometry is a versatile technique to visualize vertical distances from a few to a few hundred nanometers between two surfaces. The method of the reflection interference contrast microscopy (RICM) can be used to observe the behavior of colloidal probes close to a wall as well as the adhesion of cells or vesicles (Rädler and Sackmann 1992, Kühner and Sackmann 1996, Albertsdörfer et al. 1997). The combination of 0.2 micron lateral resolution and nanometer vertical resolution makes micro-interferometry a powerful tool to study the heterogeneous structure of an adhesion disc. Abercrombie and Ambrose (1958) and Curtis (1964) first applied this technique to the study of cells. A major improvement was the introduction of the antiflex technique by Ploem (1975). Later, the development of digital image processing opened up the possibility to access much better temporal and spatial resolutions (Schilling 1999).

In the following chapter we will first give a brief introduction to conventional RICM. Next, we shall discuss the constraints of the technique resulting from the periodicity of the interference pattern. By introducing a second wavelength to the setup, these problems can be solved for the height ranges relevant to membrane studies. In the last paragraph of this chapter, we will demonstrate that the new technique enables us to determine the height of the contact area of a vesicle.

1.2 RICM

1.2.1 Reflection Interference

The reflection interference technique is depicted in Fig. 1.1 where an object (in this case a colloidal bead) immersed in buffer and hovering on a glass substrate is illuminated by monochromatic light from underneath. The image is formed by the interference of the light reflected at the glass-buffer interface (denoted by 1 in the

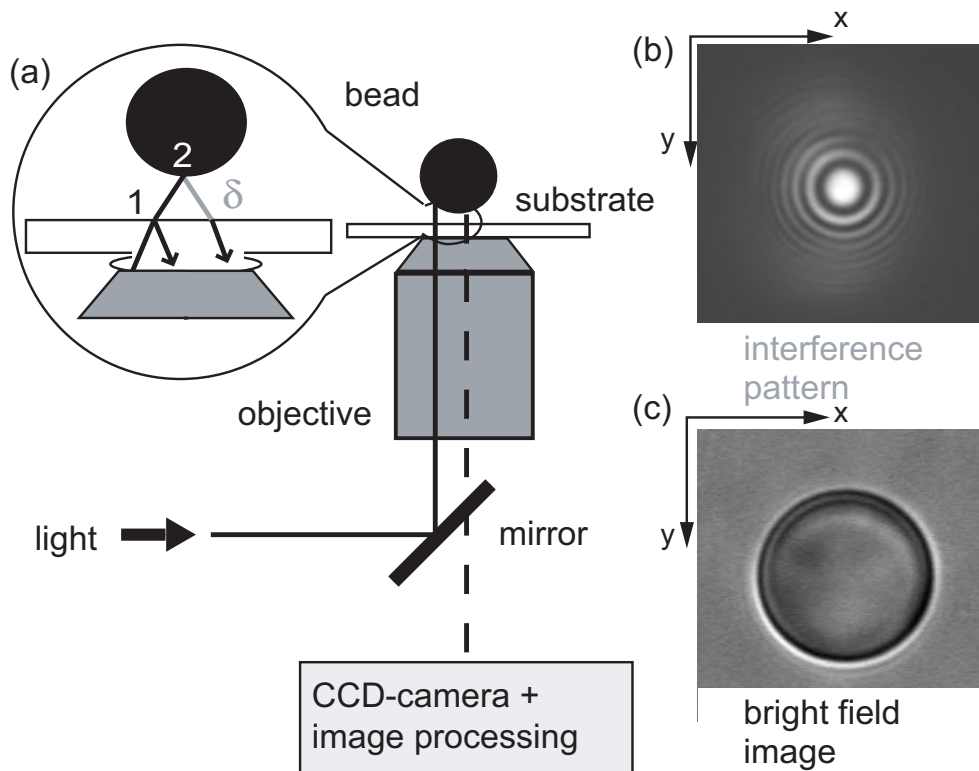


Figure 1.1: (a) Systematic sketch of the Reflection Interference Contrast Microscopy (RICM) setup. The micrographs show a colloidal bead in RICM (b) and bright field technique (c).

figure) and the buffer-object interface (denoted by 2), respectively. The resulting interferogram (cf. Fig. 1.1b) contains information about the vertical distance h of the object above the substrate. The circular fringes in Fig 1.1b are Newton rings, which indicate the bending off of the bead surface from the flat glass substrate. A size comparison with the bright field image shows, that light reflected from only a small area near the bottom of the bead contributes to the interferogram, cf. Fig. 1.1b and c.

The observed intensity $I(\vartheta)$ of the interfering beams with intensities I_1 and I_2 is:

$$I(\vartheta) = I_1 + I_2 + 2\sqrt{I_1 I_2} \cos [2kh(x, y) \cos \vartheta + \phi], \quad (1.1)$$

where ϑ is the angle of incidence, $h(x, y)$ is the distance between the substrate and the object as a function of the lateral position (x, y) , and $k = \frac{2\pi n}{\lambda}$ is the wave vector corresponding to the wavelength λ . The constant phase ϕ accounts for the phase shift between the two reflected beams, which depends on the angle of incidence as well as the polarization of the light.

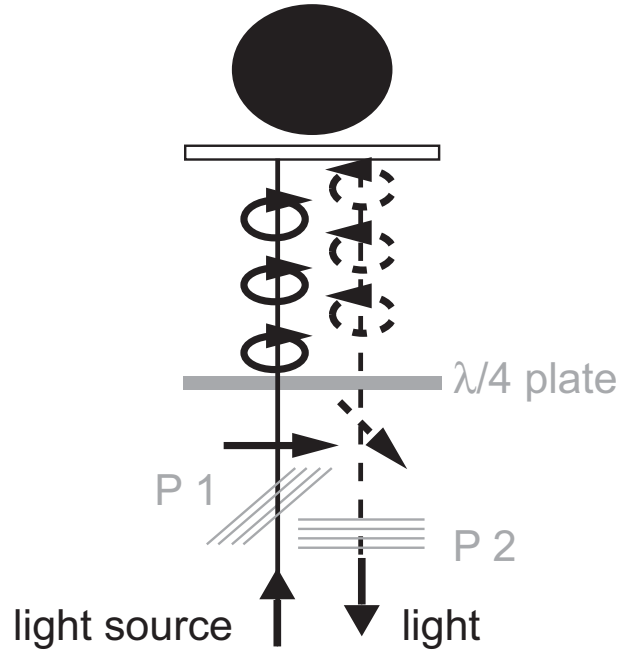


Figure 1.2: Principle of the antiflex-technique. The light is circularly polarized by an polarizer P_1 and a quarter-wave plate. Subsequently, the polarization of the light is shifted by 90° upon reflection and passes the analyzer P_2 , which is orientated perpendicularly to P_1 .

1.2.2 Antiflex Technique

The reflectivity of biological relevant interfaces like water based buffers, polymers and membranes are very low. The reflective coefficient r is given by

$$r = \frac{(n_1 - n_2)^2}{(n_1 + n_2)^2}, \quad (1.2)$$

and can be calculated to $r_1 \simeq 4.0 \times 10^{-3}$ for light reflected at the glass/buffer interface and $r_2 = 6.5 \times 10^{-4}$ for light reflected at the buffer/membrane interface with $n_{\text{glass}} = 1.51$, $n_{\text{buffer}} = 1.34$ and $n_{\text{membrane}} = 1.4$ (Born and Wolff 1999). Light reflected by any component within the microscope is more intense. To overcome this problem, Ploem (1975) developed the antiflex technique. Two polarizers (P_1 , P_2) and a quarter-wave plate are placed in the path of light rays, as shown in Fig. 1.2. The monochromatic light from the microscope light source (typically a mercury lamp with a monochromator) is linearly polarized by the polarizer P_1 . Upon passing through quarter-wave plate the light is transformed into circularly polarized light and reflected at the various interfaces. Every reflection of circularly polarized light at an optical interface - no matter whether the second material is optically denser or less dense with respect to the first - switches the direction of polarization (Hecht 1987). The light passes the quarter-wave plate a second time and is transformed back to

linearly polarized light, but with the direction of polarization perpendicular to the incident direction. An analyzer P_2 , oriented perpendicular to P_1 allows only light which passes the quarter-wave plate twice to exit the microscope.

1.2.3 Reconstruction of the Height Profile

For the reconstruction of the height profile of the object from the RICM intensity distribution, three different approaches exist:

- The simple theory that considers only light which enters the sample in direction normal to the plane of the substrate. Thus, any divergence of the incident beam or the reflected beam is neglected. This approach gives surprisingly good results for relative height differences smaller than 100 nm and permits precise shape reconstructions up to 800 nm if the height is continuously increasing or decreasing (Wiegand et al. 1998).
- The finite-aperture theory (Gingell and Todd 1979, Rädler and Sackmann 1993) accounts for all angles appearing in the illumination cone. The angles can be calculated from the diameter of the aperture diaphragm of the microscope. The height of an object can not be expressed in terms of an analytical function of the intensity. However, a correction factor for the wavelength and therefore the height can be calculated. For the present setup the factor is 0.97, which gives a variation of less than 4 nm for heights of 100 nm (Rädler and Sackmann 1993).
- The non-local theory, developed by Kühner and Sackmann (1996) is the most exact theoretical description of the RICM image. It takes the finite illumination aperture angle and the reflection of rays at curved interfaces into account. The main advantage is the exact determination of absolute object-substrate distances (2 nm) for objects with known shapes. The disadvantages are the time consuming numerical procedures and the need of knowing the geometry of the object. For a bead the shape is given, whereas for the contact domain of a giant vesicle this is not the case (cf. below). By the introduction of correction factors (Wiegand et al. 1998), a reduction of time for the analysis can be achieved.

For the experiments in this thesis, the height reconstruction according to the simple theory will be considered. Since the main focus is the analysis of vesicle membranes, a defined shape is not given and additionally the scatter of the data will be about 5...10 nm (cf. section 2.3.4), making a correction in the sub-scatter range not reasonable.

Next, the reconstruction procedure will be discussed taking the example of a bead which lies on a glass substrate. Since the bead has spherical symmetry, it is

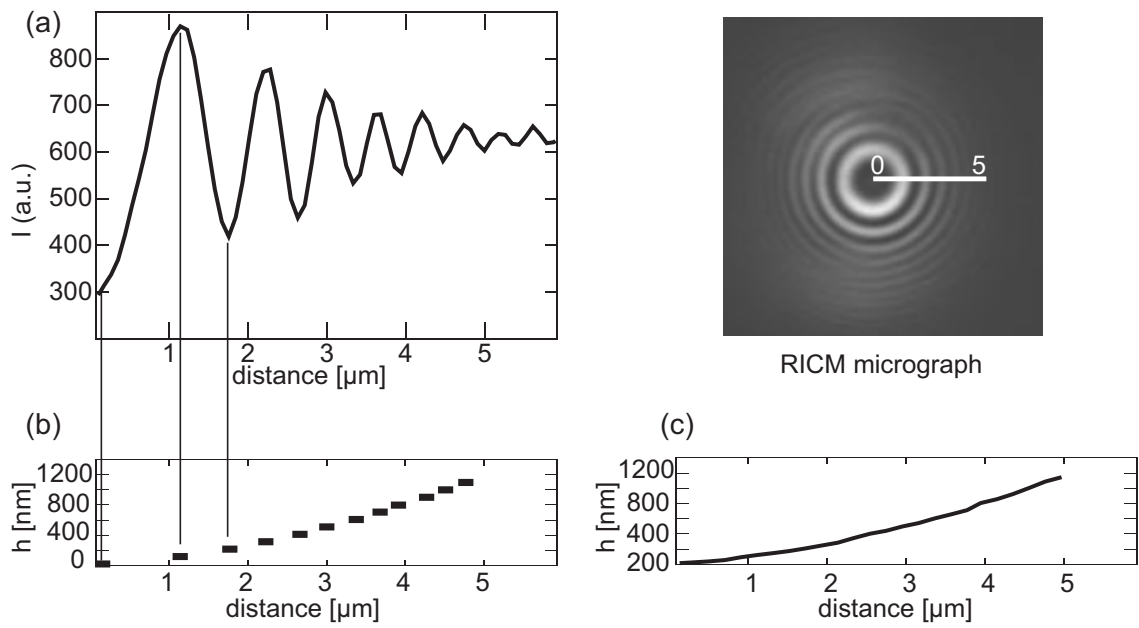


Figure 1.3: a) Intensity profile I along the white line in the RICM micrograph. b) From the extremal values single heights h can be reconstructed according to Eq. (1.3). c) By an inverse cosine function the height profile within the intervals can be analyzed, yielding a continuous height reconstruction of the object, cf. Eq. (1.4).

sufficient to consider the intensity profile along a line (a line profile), which starts at the center of the bead. The intensity profile is a curve alternating between maxima and minima, as shown in Fig. 1.3a. The optical path difference between an adjacent interference minimum and maximum is $\delta = \frac{\lambda}{2n}$, and therefore the height difference Δh is determined by:

$$\Delta h = \frac{\delta}{2} = \frac{\lambda}{4n}. \quad (1.3)$$

Single values for the height reconstruction are obtained as shown in Fig. 1.3b. The contour within these intervals is given by an inverse cosine function, according to Eq. (1.1), with the constant phase shift $\phi = 0$:

$$h(x) = \frac{\lambda}{4\pi n} \arccos(I(x) - I_1 - I_2), \quad (1.4)$$

where I_1 and I_2 are the minimal or maximal intensity I_{min} or I_{max} , depending on whether the evaluated interval starts with a minimum or maximum intensity value. The inverse cosine transformation is calculated for each interval, leading to a complete height reconstruction.

In analogy to the example of the bead, the contour of a vesicle can also be reconstructed. A giant vesicle is a simple cell model consisting of a phospholipid bilayer formed as spherical shell and a inner liquid, which stabilizes the vesicle. By deflating the vesicle, i.e. generating excess area (cf. section 2.3.2), the vesicle forms a rather circular contact area with a flat substrate of about 5...10 μm diameter. The height within that contact area can be measured by RICM, as shown in Fig. 1.4. Domains of tight adhesion are dark, because the lipid bilayer height above the substrate is small compared to the wavelength of light ($\sim 2...5$ nm (Marra and Israelachvili 1985)), whereas areas of bright intensity have a distance of 100 nm. The free contact area of the vesicle fluctuates and exhibit intensities changing between dark and bright in time.

Further the contour of the vesicle can be analyzed, similar to the contour of a bead. However, the shape of the vesicle lacks spherical symmetry and therefore the height has to be measured at different points along the contact area.

1.2.4 RICM Setup

The setup consists of a modified inverted microscope Axiomat or Axivert 200 (Zeiss, Germany), which is illuminated by a high pressure mercury lamp (HBO 103W/2, Osram, Germany) cf. Fig. 1.5. A band-pass filter (BP, transmission from 400-800 nm) is used directly after the mercury lamp in order to protect all subsequent filters and optical components against heat. After this the illumination spectrum is reduced to the 546.1 nm line (green) by an interference filter (IF_g 546.1 nm, 85% transmission, 12 nm waveband). The angle of the illumination cone is controlled by an adjustable aperture diaphragm (AD), which is closed to its minimum in order to reduce the divergence. This gives the most parallel light possible in the plane of the object.

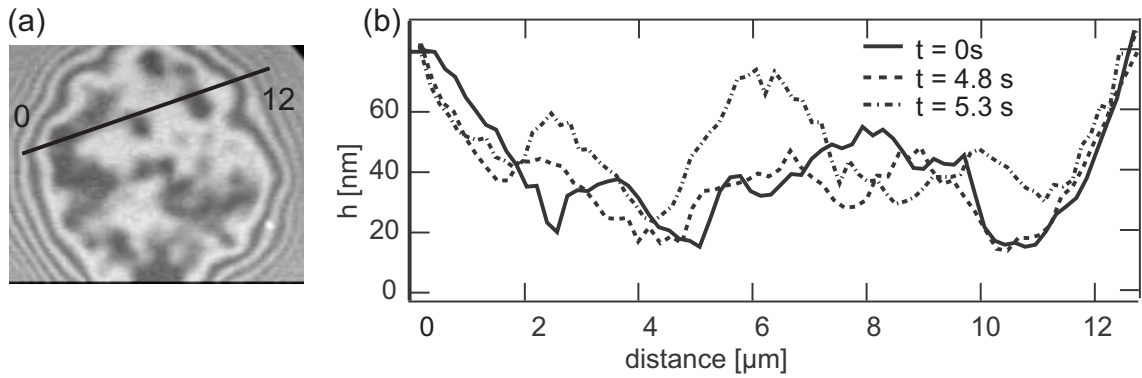


Figure 1.4: a) RICM micrograph of the contact area of a giant vesicle hovering above a glass substrate b) Line profile of the membrane height h in the contact area along the indicated line at three different times.

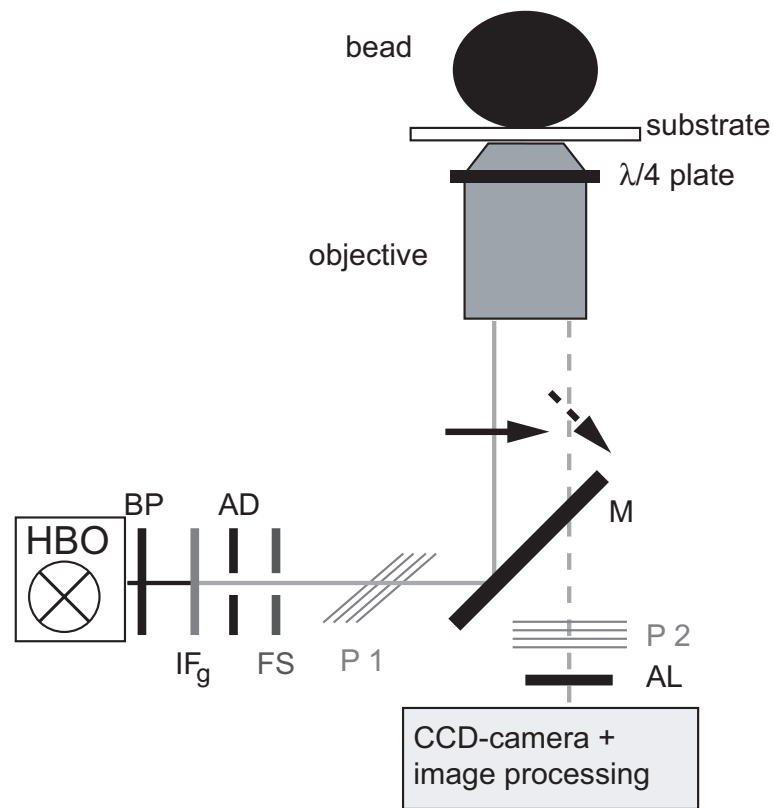


Figure 1.5: Systematic setup of the RICM, with HBO for mercury lamp, BP for band pass filter, IF_g the green interference filter, AD for aperture diaphragm, and FS for field stop. P_1 , P_2 are the two polarizers, M a mirror, and AL achromatic lens.

Further the microscope needs to have a second diaphragm, the field stop (FS), which delimits the illuminated field and defines the plane of the object precisely. To apply the antiflex technique, two polarizers (P_1 , P_2) with perpendicular polarization directions are in the path of the light. A neofluoar objective (antiflex, 63x, oil immersion, N.A.=1.3, Zeiss, Germany) equipped with a wavelength-independent quarter-wave plate was used. The interferograms are focused by an achromatic lens (AL, Achromat $f = 250\text{mm}$, Linos AG, Germany) onto a Peltier-cooled 10-bit camera (C 4880-85, Hamamatsu, Japan), recently adapted to the microscope.

The data collection is carried out through a real time image processing software Open BOX (Schilling 1999). By a wavelet transformation, the size of the data recorded (typically 10 min at 100 Hz amounts to 5 GB) can be reduced to 10% of the initial size. Thereby no considerable loss of information occurs as confirmed by an identical height determination from the original and the compressed data. The reduced data is easier to handle and to store.

The major advantage of digital image processing with respect to the previously installed analog video recording is the accessibility of time resolutions up to 100 Hz. Additionally, the data loss due to storing the data on a video tape is omitted.

1.2.5 Dual Wavelength Technique

A serious limitation of the RICM technique is the ambiguity in the height determination. Since the interference pattern displays a periodic series of constructive and destructive interference according to Eq. (1.1), for $\lambda = 546.1\text{ nm}$ and $n = 1.34$ heights above $\frac{\lambda}{4n} = 101.9\text{ nm}$ can not be determined unambiguously. One intensity value can belong to multiple heights, as depicted in Fig. 1.6a.

In order to overcome this limitation, we devised a new technique where the

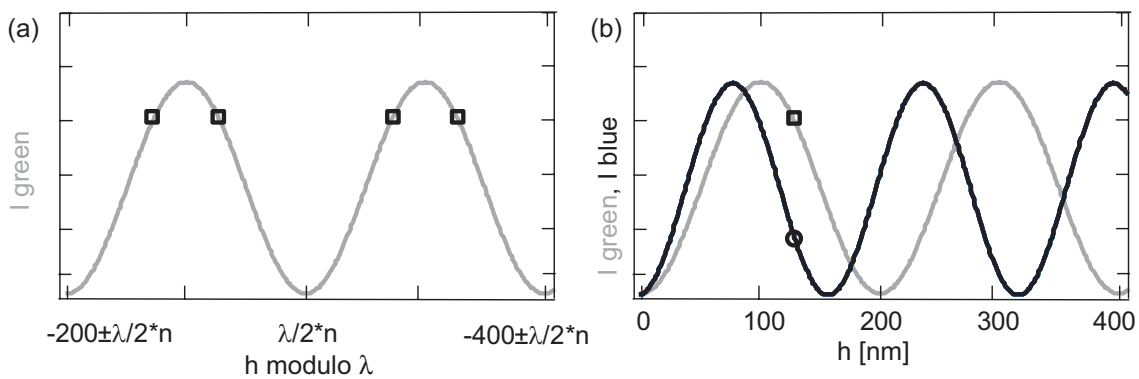


Figure 1.6: a) Intensity of the green wavelength I_{green} plotted versus the height h modulo lambda, i.e. the distance between the object and the substrate. b) Intensity of the green and the blue wavelength I_{green} and I_{blue} , plotted versus the absolute height.

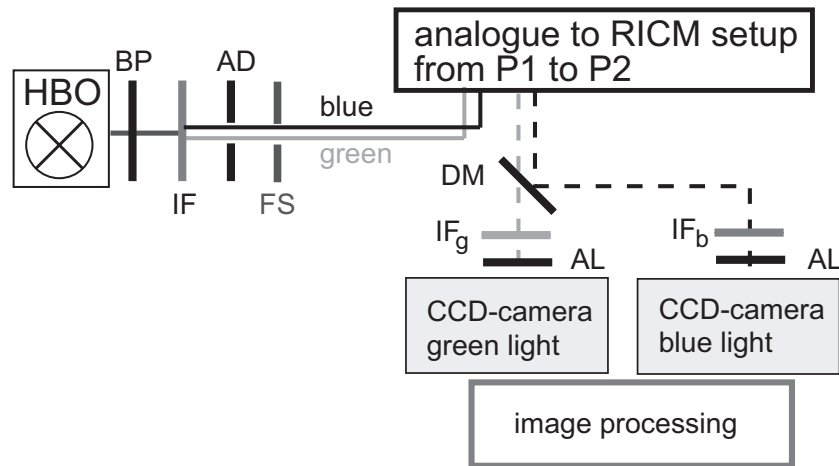


Figure 1.7: In the dual wavelength RICM setup the RICM micrograph is recorded simultaneously using two different wavelengths (green and blue). The interferometric filter (IF) transmits both wavelengths. After passing through the usual RICM setup, cf. Fig. 1.5, the two wavelengths are separated by a dichroic mirror (DM). With an interference filter (IF) and achromatic lens (AL) for each color the image is focused on a camera and an image processing unit.

principal idea is to illuminate the object with a second wavelength $\lambda_2 = 436$ nm (blue). The intensities of the interference pattern for each wavelength are measured independently and simultaneously. The interference pattern for the blue line is again a cosine function, but with a different periodicity. Additionally, the boundary condition for both intensities requires zero intensity at zero height, what gives rise to a phase relation between the two wavelengths and thus an unambiguous height determination, cf. Fig. 1.6b. Measuring the intensity value marked by the black square for the green wavelength and simultaneously the black circle for the blue wavelength lead to an unambiguous height determination.

To realize the above idea in the setup of the microscope a filter transmitting both at 546.1 nm and 486 nm (blue) (IF interference filter, 85% transmission, 12 nm waveband, Analysetechnik, Germany) is inserted as shown in Fig. 1.7. At the end of the path of rays, the blue and green line are separated by a dichroic mirror (DM) and finally an interference filter in each optical path cuts off undesired wavelengths. The two separated beams are focused onto two different digital cameras and recorded by two image processing systems, which have to be synchronized in time and position (cf. below).

In the following the dual wavelength technique is shown to give unambiguous results for the height of a vesicle membrane above a substrate, cf. Fig. 1.8a and b. From the green wavelength, the height reconstruction is calculated as described

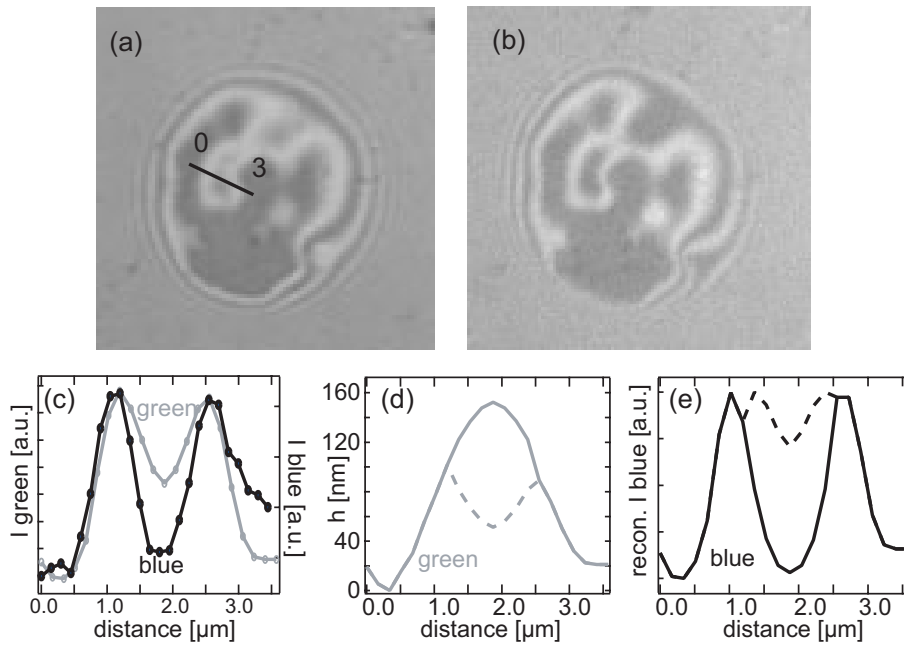


Figure 1.8: RICM micrograph of a giant vesicle in contact with a glass substrate. (a) Intensity I_{green} of the green wavelength and (b) of the blue wavelength I_{blue} . In (c) the intensity of the green (I_{green}) and blue wavelength (I_{blue}) along the line displayed in (a) are given. (d) Ambiguous height reconstruction from the green wavelength, with two possible profiles given as a solid line or dotted line. (e) Calculated intensity of the blue wavelength from the reconstructed profiles given in (d). Since the solid line agrees with the measured intensity profile, displayed in (b), this height reconstruction is the correct one.

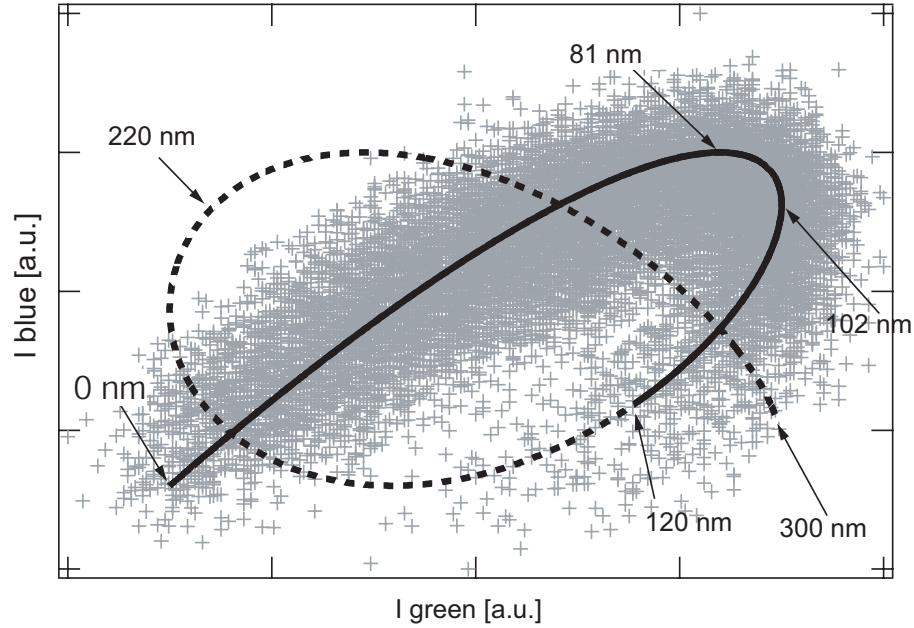


Figure 1.9: The markers display the measured intensity of the blue wavelength versus the intensity of the green wavelength. The line is the theoretically calculated curve.

previously. According to Fig. 1.8 at the height $h = 100$ nm, a decrease in the intensity of the green wavelength between 1.5 and $2.5 \mu\text{m}$ in Fig. 1.8c can result either from an upward or downward deflection of the membrane. This is indicated by the solid and dotted line in the height reconstruction, Fig. 1.8d. By calculating the intensity distributions of the blue wavelength (Fig. 1.8e) from the two reconstructed height profiles and comparing them to the measured one, displayed in Fig. 1.8c, it is evident that the solid line is the correct reconstruction. The dotted line gives an incorrect intensity profile.

Further, the dual wavelength technique makes it possible to determine absolute heights at which a free membrane fluctuates above a substrate. In the RICM these out of plane fluctuations of the membrane are observed as changes in intensity. For a membrane patch A of about $1 \mu\text{m}^2$ lateral size within the contact area one observes successively low and high intensities. Plotting now the intensity measured for the blue wavelength versus the intensity measured for green wavelength yields the curve given in Fig. 1.9. The absolute height can be determined, since this plot gives a unique functional relationship. From a comparison of the data to the calculated curve (black line), the height interval in which the membrane patch A is moving can be determined to $0 \dots 120$ nm. The large scatter of the data will be discussed in section 2.3.4. It is important to evaluate exactly the same positions of the membrane on the two different cameras. Consider A_{green} the membrane patch analyzed from the green wavelength. In order to find exactly the corresponding

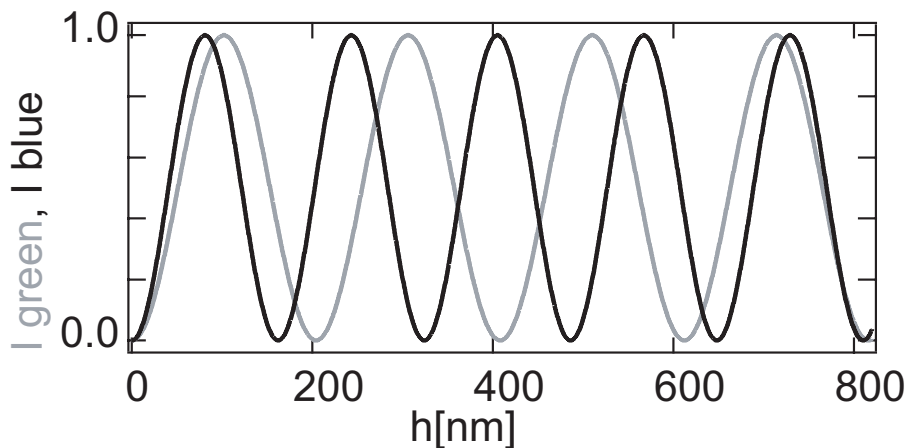


Figure 1.10: The intensities I_{green} and I_{blue} of the green and the blue wavelength plotted versus the height h . The phase relation between the two curves is ambiguous for heights above 400 nm.

patch A_{blue} in the camera recording the blue wavelength an approximate position of \tilde{A}_{blue} is determined from comparing for example the diaphragms in single images of the green and blue wavelength. Subsequently, the correlation of a matrix of patches around \tilde{A}_{blue} (typically 11 x 11) with A_{green} is analyzed. The exact position A_{blue} exhibits a maximum in the correlation function, since for identical points the membrane motion is identical. Further, a time correlation of A_{green} and A_{blue} determines the exact time difference between the two recorded time series.

The determination of absolute heights is unambiguous for heights below 400 nm. Above that height the phase relation between the two wavelengths is ambiguous since the phase relation of the two wavelengths is symmetrical to about 400 nm, cf. Fig. 1.10. Theoretically the unambiguous height determination range can be enlarged by choosing different wavelengths. However in order to have reasonable intensities only the spectral lines of the mercury lamp can be used. Switching to laser illumination could solve these difficulties. Further, the use of a third wavelength from the mercury lamp can also enlarge the range of unambiguous height determination (Schilling 2003).

1.3 Outlook

The ability of measuring absolute heights can not only be used for the study of giant vesicles, but also to determine the height of colloidal beads. Polystyrene beads perform Brownian motion in an aqueous solution. These up and down motions can be used to determine the interaction potential between the bead and the underlying substrate (Kühner and Sackmann 1996). The substrate can be for example, a glass slide in order to investigate the electrostatic interaction in dependence of the salt

concentration of the surrounding buffer. Further, colloids can be deposited on biocompatible films supported by glass surfaces, and their thickness can be analyzed by measuring the height of the bead. This enables measurements of the thickness of soft brushlike grafted polymers on glass. These thickness measurements are extremely difficult with other techniques such as ellipsometry since the refractive index of the polymer film is comparable to that of the aqueous phase.

The measurement of the motion of the beads allows at the same time to probe the lateral homogeneity and the viscoelastic properties of the films (Sengupta et al. 2003). Especially glycolipid molecules are particularly well suited to support vesicles or cells. Due to their strong swelling behavior and soft viscoelastic behavior of entangled polymers in solution they do not alter the natural structure of proteins or cells under study and might be an important prerequisite for cell studies.

Chapter 2

Fluctuations of Membranes

2.1 Introduction

Phospholipid membranes consist of two ultrathin and highly flexible sheets made up of amphiphilic molecules. In aqueous solutions they self-assemble due to the hydrophobic effect. Thereby, the hydrocarbon chains are in close contact and the hydrophilic headgroups of the molecules point towards the water on both sides of the bilayer, cf. Fig. 2.1. Interest in biological membranes, such as the lipid-rich cell surface, has been an important motivation for the study of surfactant bilayers. Apart from their significance as model systems of biological membranes, surfactant bilayers exhibit a variety of unique properties like phase transitions, elasticity, and fluctuation phenomena. The adhesion of membranes to other membranes or to substrates is governed by an interplay of molecular forces and entropic interactions.

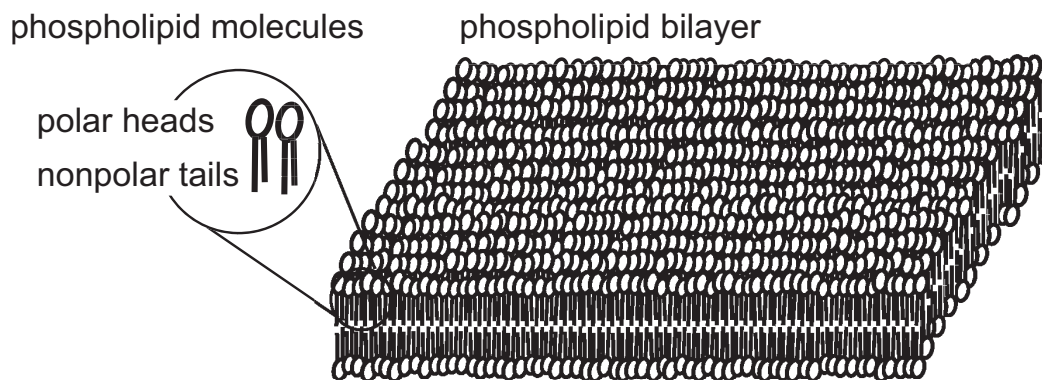


Figure 2.1: Schematic view of phospholipid molecules with a polar headgroup and two nonpolar hydrocarbon chains. The bilayer is assembled from these molecules and forms a large structure.

The entropic interactions arise from the thermally excited shape fluctuations of membranes.

The "bare" bilayer-bilayer interaction energy per unit area - denoted by $V(h)$ - is repulsive for spacings or heights h in the sub-nanometer range. Here, the hydration interaction between the polar headgroups of the lipid molecules is repulsive. At larger spacings the attractive van der Waals forces (vdW forces) compete with electrostatic repulsion (Israelachvili 1991). In the biologically relevant range where the salt concentration of the surrounding medium is about 150 mM, $V(h)$ has got a single minimum. This "van der Waals minimum" has a depth $W = -V(h^*)$ of about $10^{-4} \dots 10^{-5} \text{ J m}^{-2}$ at a spacing $h^* \approx 2 \dots 3 \text{ nm}$. An elegant method to investigate the bare bilayer-bilayer interactions of rigid bilayers are surface force apparatus measurements using two mica surfaces onto which the membranes are immobilized (Marra and Israelachvili 1985).

In addition to the bare bilayer-bilayer interaction free membranes undergo thermally excited shape fluctuations, so-called undulations. These out of plane fluctuations result in a repulsion when the motion of the free membrane is confined in space. Helfrich (1978) was the first to consider this entropic repulsion which renormalizes the interaction energy $V(h)$ and reduces the energy W . Later he reported that membranes initially attached together were observed to unbind upon a change in temperature (Mutz and Helfrich 1989). The unbinding is characterized by a divergence of the mean spacing h between the membranes. Lipowsky and Leibler (1986) derived from functional group renormalization theory that this unbinding should be a continuous phase transition with a critical value W_{cr} of the interaction energy of $W_{cr} = 10^{-5} \dots 10^{-6} \text{ J m}^{-2}$. In a subsequent work, the mean spacing $\langle h \rangle$ was predicted to be a universal number for $W > W_{cr}$, independent of both the internal structure of the membrane and the details of the form of the wall potential (Leibler and Lipowsky 1987). Later, a numerical expression for the Helfrich repulsion could be deduced (Seifert 1995) and Monte Carlo simulations confirmed the numerical description (David and Leibler 1990, Gompper and Kroll 1989, Netz 1995). Small-angle X-ray diffraction studies (SAXS) of stacked lamellar bilayers were the first experiments to quantify this calculated dependency, albeit with a discrepancy in a constant value (Safinya et al. 1986). All these experiments and theoretical considerations demonstrate that Helfrich repulsion has become a central concept in analyzing the phase behavior of lipid bilayer systems.

More recently, interest has focused on the closed lipid bilayers - known as vesicles or liposomes, cf. Fig 2.2. These vesicles normally contain additives such as low concentrations of polyethylene glycol lipid (PEG lipid), a lipopolymer that prevents vdW aggregation between bilayer membranes through steric repulsion (Lasic 1993). A second important additive is cholesterol, which acts as a stabilizing and anti-freeze agent (Nielsen et al. 2000). Both lipopolymers and cholesterol are highly soluble in lipid membranes (Gennis 1989). Since the collision energy is a universal quantity that does not depend on the details of the membrane structure, the LL

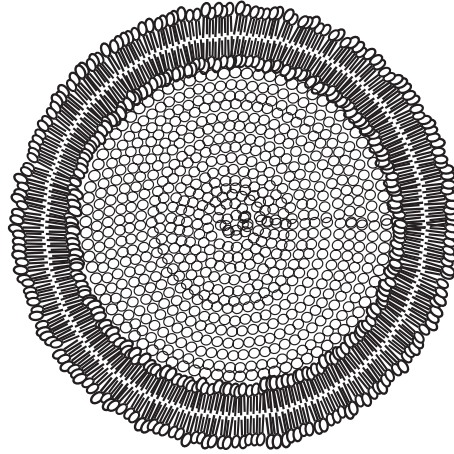


Figure 2.2: Section of a pure phospholipid vesicle, made up of lipid molecules in the form of a closed bilayer.

theory should retain its validity for multi-component systems. However, an earlier SAXS study of stacked bilayers containing PEG-lipid additives found an unexpected singular dependence of the Helfrich Repulsion on the surface concentration of the additives (Castro-Roman et al. 1999).

The following chapter reports on a study of the applicability of the LL theory to multi-component bilayers, containing PEG-lipid and cholesterol additives. With the reflection interference contrast microscopy (RICM, cf. chapter 1) a real-space observation of the fluctuating substrate membrane spacing is possible. Due to the recently developed high resolution in vertical direction (5 nm) and time (> 100 Hz), the RICM provides a powerful setup which enables insights into the complex interplay of entropic and molecular forces.

2.2 Theory

In order to describe the existing theories for the unbinding of membranes we shall first elucidate the individual forces acting on a membrane in close contact to a substrate. The description will be delimited to vesicle membranes, since the following experiments are done on this system.

Here, we will consider generic forces such as the vdW forces or gravity. In the case of water suspended bilayers on casein coated glass substrates, these interactions will be attractive but weak and therefore we refer to them as weak adhesion. The attraction is mainly counterbalanced by the entropic Helfrich repulsion. In contrast, an additional specific interaction between receptors and conjugated ligands will be referred to as strong adhesion. The specific interaction relies on the so-called lock-and-key force principle and shall be discussed in chapter 4.

2.2.1 Generic Forces

Gravitation

Gravitation is acting on the vesicles, since they are filled with a solution of higher density with respect to the outer medium. The deflated vesicle has some excess membrane area with respect to its volume and can therefore form a contact area A_C with a flat surface. According to Boulbitch et al. (2001) the gravity of a deflated vesicle on a supporting substrate is:

$$V_{\text{grav}} = \frac{\Delta\rho}{A_C} V_V g h, \quad (2.1)$$

with $\Delta\rho$ the difference in density between the inner and outer medium of the vesicle, the volume of the vesicle V_V , the acceleration due to gravity g , and the height h of the membrane above the substrate. The mass of the phospholipid membrane is neglected since its volume is three orders of magnitude smaller than the volume of the sucrose solution.

Van der Waals Force

The vdW force is a generalized electrostatic interaction which results from the following different dipole-dipole interactions:

- the Keesom interaction describes the attraction between permanent dipoles,
- the Debye interaction accounts for the potential between permanent and induced dipoles in opposing molecules or surfaces,
- the Dispersion interaction (London interaction), stems from the interaction between non-polar molecules. Due to the charge fluctuations within each molecule, temporary dipoles appear or are induced.

Since at least one of these interactions act between every possible pair of molecules, the generalized vdW force is omnipresent (Israelachvili 1991). For two interacting molecules all three components have the same distance dependence $\propto \frac{1}{h^6}$, where h is the distance between the molecules. In the geometry of a flat membrane on top of a planar solid surface the integration over all molecules leads to (Lipowsky 1989):

$$V_{vdW}(h) = -\frac{A_H}{12\pi} \left[\frac{1}{h^2} - \frac{1}{(h + \delta)^2} \right], \quad (2.2)$$

where δ is the membrane thickness. A_H is the Hamaker constant, a material constant, which describes the resultant dipole-moments. Different theories predict the value of the Hamaker constant (Israelachvili 1991). Within the simplest model all interactions with the nearest neighbor molecules are summed up. In a more complex theory the retardation of the \vec{E} -field is included. This leads to a decrease in the

Hamaker constant at distances further than 100 nm. Moreover, the reduction of the van der Waals force by the presence of ions in the solution has to be taken into account (Dzyaloshinskii et al. 1961). This model predicts the Hamaker constant for lipid membranes on glass separated by a water film to be $A_H = 10^{-21} - 10^{-22}$ J. The values are confirmed with surface force apparatus measurements by Israelachvili (1991).

Helfrich Repulsion

Free, fluid membranes perform out of plane fluctuations which are induced thermally. In the vicinity of a substrate these fluctuations generate an entropic repulsion. This effect arises as the membrane is bumping repeatedly against the substrate. In other words the presence of the substrate cuts off the area in which the membrane can undulate freely. Not only a rigid substrate, but also a second membrane sterically hinders the fluctuations and gives rise to a repulsive force. Helfrich (1978) was the first to include an entropic term in the interaction potential, while he considered a tensionless membrane:

$$V_{He} = c_{fl} \frac{(k_B T)^2}{\kappa \langle h \rangle^2}, \quad (2.3)$$

with the bending stiffness of the membrane κ , a dimensionless pre-factor c_{fl} , the height of the membrane $\langle h \rangle$, and the thermal energy $k_B T$.

Polymeric Repulsion

A steric stabilization force arises because cell membranes are coated with a hydrated layer of long-chain polymer molecules (the so-called glycocalix). If such polymer-coated surfaces approach each other, the polymer layers overlap and are squeezed together. Since this requires energy it is more favorable to push the polymers out of the contact area. The resulting depletion force limits the pushing out of polymers from the contact area. This force will be discussed in detail in section 4.3.3.

2.2.2 Total Interaction Potential

Superposition

To determine the total interaction potential of a membrane in the vicinity of a substrate the superposition of the following generic interactions is considered as a first approach:

$$V(h) = V_{grav}(h) + V_{vdW}(h) + V_{He_{tensed}}(h) + V_{glycocalix}(h), \quad (2.4)$$

with V_{grav} and V_{vdW} according to Eq. (2.1) and Eq. (2.2), respectively with $V_V = 3.35 \times 10^{-14}$ m³, $A_C = 1.2 \times 10^{-10}$ m², $g = 9.81$ m s⁻², $\Delta\rho = 50$ kg m⁻³, $\delta = 38$ Å,

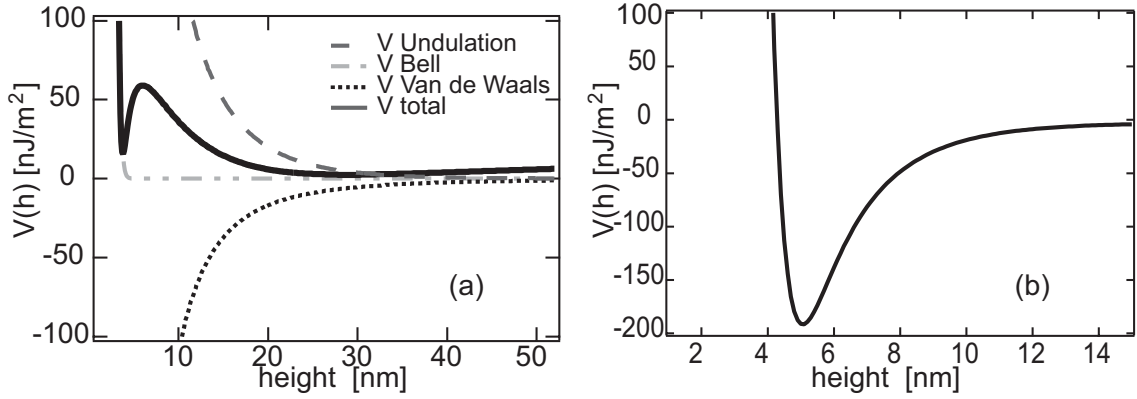


Figure 2.3: Superposition of different interactions acting on a membrane van der Waals force, Helfrich repulsion and polymer repulsion

and $A_H = 8.7 \times 10^{-22}$ J. The undulation or Helfrich repulsion of a tensed membrane is given by Seifert (1995)

$$V_{He\ tensed}(h) = \frac{6(k_B T)^2}{(2\pi)^2 \kappa} \left[\frac{\Omega}{\sinh \Omega h} \right]^2, \quad (2.5)$$

where $k_B T = 4 \times 10^{-21}$ J at room temperature, $\kappa = 25 k_B T$ and $\Omega = \sqrt{\frac{\pi\gamma}{2k_B T}}$ with the tension $\gamma = 1,7 \times 10^{-5}$ Jm $^{-2}$ for a pure phospholipid giant vesicle. The last term in Eq. (2.4) accounts for a steric repulsion of the protein passivation layer on the glass slides and the lipopolymers in the membrane (Bell et al. 1984).

$$V_{glycocalix}(h) = \frac{\zeta}{h} \exp\left[-\frac{h}{\tau}\right], \quad (2.6)$$

where $\zeta = 10^{-8}$ N measures the stiffness of the polymer layer and $\tau = 2$ Å is the size of the adsorbed proteins.

For the given set of parameters we obtain the potential shown in Fig. 2.3a. It exhibits a sharp minimum at a height $h = 3 \dots 4$ nm and a broad minimum at $h = 20 \dots 30$ nm. The double well minimum arises from the counteraction of V_{vdW} and V_{He} . It is important to note that for example by slightly increasing the vdW attraction from 8.7×10^{-22} to 1.3×10^{-21} a single minimum potential equal to Fig. 2.3b arises.

For the unbinding of a membrane in these potentials a first order phase transition is found (Milner and Roux 1992, Swain and Andelman 1999). Since the position of the minimum \bar{h} is chosen as the order parameter and the Hamaker constant A_H as a state variable, one finds a non-continuous behavior of the ordering parameter \bar{h} at the critical value $A_{H_{cr}}$: from a defined value for $A_H < A_{H_{cr}}$ \bar{h} jumps to a much higher value, a behavior characteristic for a discontinuous transition (first order transition).

Since Lipowsky and Leibler (1986) predicted a second order unbinding transition (continuous phase transition) from functional renormalization group considerations,

the simple superposition approach is not adequate to describe the situation. The failure arises as the Helfrich repulsion was originally derived under the assumption that membranes do not interact with anything else, which obviously does not hold for the complex situation here.

Renormalization Group Theory

Lipowsky and Leibler (1986) developed an elaborate theory for the unbinding of membranes under the action of the Helfrich repulsion. By the use of group renormalization theory they found a second order transition between a bound state and an unbound state of membranes as a function of the Hamakar constant A_H . The value of the minimum height between the membranes, which is now chosen as a state parameter, diverges as the Hamakar constant approaches a critical value from above. This behavior determines a second order transition following the Landau criteria.

In a following work Leibler and Lipowsky (1987) theoretically analyzed the fluctuations of a membrane in the unbound state. They found that the fluctuations $\Phi(\vec{r}, t) = h(\vec{r}, t) - \langle h \rangle$, where \vec{r} is the lateral position and h the height of the membrane should be governed by a Gaussian Hamiltonian:

$$H(\Phi) = \frac{1}{2}\kappa \int d^2r [(\nabla^2\Phi)^2 + 4\xi_{\parallel}^{-4}\Phi^2]. \quad (2.7)$$

Here, κ is the bending stiffness of the membrane and ξ_{\parallel} is the in-plane correlation length defined by:

$$\xi_{\parallel} = \frac{8}{C_{\parallel}} \sqrt{\frac{2\kappa}{k_B T}} \langle h \rangle, \quad (2.8)$$

where $C_{\parallel} \approx 5.83$ is an universal amplitude ratio (Netz 1995). The probability distribution $P(h)$ resulting from Eq. (2.7) is a single peak gaussian with a root mean square (rms) width $w = \langle \Phi \rangle$ proportional to the mean spacing

$$w = \frac{\langle h \rangle}{C_{\perp}}, \quad (2.9)$$

where $C_{\perp} = \sqrt{5}$ is another universal amplitude ratio (Netz 1995).

Flory-Huggins-like Theory

Milner and Roux (1992) suggested a mean field approach to construct a simple picture for the unbinding transition calculated by Lipowsky and Leibler (1986). They introduced as order parameter the volume fraction $\tilde{v} = \delta/h$, where δ is the thickness of the membrane. In analogy to the Flory-Huggins description of polymers (deGennes 1980), the Helfrich estimate for the entropy is taken into account accurately, whereas the other interactions are approximated via a second virial term χ .

The free energy of the introduced interaction potential was calculated to:

$$f(\tilde{v}) = \frac{b(k_B T)^2}{\kappa \delta^2} \tilde{v}^3 - k_B T \chi \delta \tilde{v}^2. \quad (2.10)$$

The free energy expression implies a second-order transition between a bound state ($\tilde{v} \neq 0$ for $\chi > 0$) and an unbound state ($\tilde{v} = 0$ for $\chi < 0$), because the order parameter \tilde{v} is continuously going to zero upon approaching the critical point. An infinitesimal change in the state variable χ from a positive value to a negative value, which is equivalent to a variation in the interaction energy, can define the transition from a bound to a free membrane. In the phase diagram of unbinding transitions presented by Milner and Roux a tricritical point appears, which separates the line of first order transitions from the line of critical points, where second order transitions take place. Along the first order transition line a coexistence of bound and unbound phases appears.

Mean Field Approach

In the work of Komura and Andelman (2002) a mean field approach for the unbinding of multi-component membranes is reported, taking into account multi-component membranes within a Flory-Huggins like approach.

Multi-component membranes are mixed systems of lipids and additives like cholesterol or lipopolymers. The concentration \tilde{C} of the inclusions is hereby $0 \leq \tilde{C} \leq 1$. For the case in which the interaction between two inclusions is attractive, the system may undergo a lateral phase separation. Since an additive poor phase coexists with an additive rich phase below a critical temperature, the phase transition is discontinuous (Keller et al. 1998).

Therefore, in the ansatz of Komura and Andelman (2002) the following different states can appear: a bound state (B1) which is poor in additives, a bound state rich in additives (B2) and two unbound states (U1) and (U2), again poor and rich in additives, respectively. The calculated phase diagram (cf. Fig. 2.4) shows indeed all these phases. In addition to the coexistence between two bound phases, a new two-phase region between two unbound states appears for a well defined interaction strength, denoted by an interval of the virial coefficient. The two unbound states are found to be separated by a first order transition. The bound state (B2) is separated from the unbound state (U2) by a second order transition as predicted by earlier theories. In contrast to the theory of Milner and Roux, here the line of second order phase transitions is ending in a line of first order phase transitions, marking a critical endpoint.

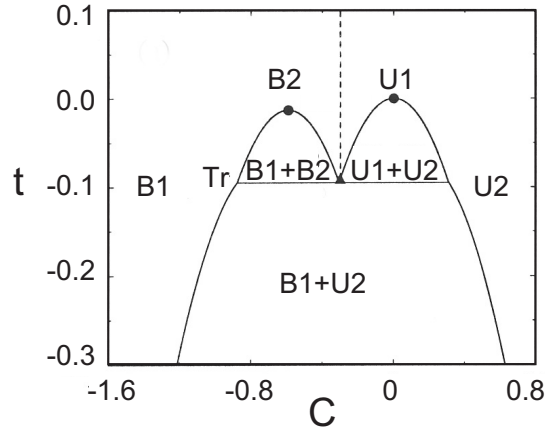


Figure 2.4: Phase diagram for $\chi = -0.3$ as a function of inclusion concentration C and reduced temperature t taken from Komura and Andelmann (2002). B1 is a bound state and poor in additives, B2 a bound state rich in additives, and U1 and U2 are two unbound states again poor and rich in additives, respectively. Tr is a triple point, whereas the critical endpoint is denoted by a filled triangle and the two critical points are denoted by filled circles.

2.3 Materials and Methods

2.3.1 Giant Vesicles

Giant vesicles are prepared by the electroswelling method, cf. the Appendix. 1,2-dielaidoyl-sn-glycero-3Phosphocholine (DEPC, purchased from Avanti Polar Lipids, Inc.) is used as matrix lipid, since the membranes are fluid at room temperature. The additives are added to the solubilized DEPC molecules. For free monolayers it is reported that DEPC is perfectly miscible with PEG lipids and with cholesterol in the concentrations used in the following (Cevc and Marsh 1987).

2.3.2 Substrate Preparation

Glass substrates are subsequently sonicated in acetone and methanol for 2 min. Then, the substrates are immersed into a 1:1:5 (v:v) solution of $\text{H}_2\text{O}_2:\text{NH}_4\text{OH}:\text{H}_2\text{O}$ at 60°C for 30 min. After rinsing the substrates intensively with pure water¹, the slides are dried. To prevent non-specific adhesion of the giant vesicles to the substrate, the substrate is incubated in the measuring chamber with a 3 wt.% solution of casein (from bovine milk, vitamin free, Bio-Rad, Germany) in buffer C for 1 h. After incubation the sample is rinsed carefully with buffer C to remove non-adsorbed

¹Water from a Millipore Q 50 purification system, Millipore SA, Molsheim, France (resistance $R > 18 \text{ M}\Omega \text{ cm}$).

material, and is kept in the buffer. 100 μl of the freshly prepared vesicle solution is added to 1000 μl buffer in the measuring chamber. Hereby, an osmotic pressure difference of 33...37 mOs acts across the vesicle membrane, which deflates the vesicles. This deflation creates excess area of the membrane with respect to the enclosed volume and enables the spherical vesicles to form a planar contact area with a flat substrate.

2.3.3 RICM

The Reflection Interference Contrast Microscopy (RICM, cf. previous chapter) is used to examine the height h of the bilayer above the substrate. For the experiments the ambiguity in the determination of h turned out to be a severe drawback. This ultimately triggered the development of the dual wavelength technique. However, most of the data have been taken with a single wavelength. The validity of the evaluation was checked using dual wavelength technique for a few representative cases.

2.3.4 Evaluation

Height-Series

The displacement field $h(\vec{r}, t)$ of the bilayer above the substrate is sampled as a function of time and lateral position using the RICM method (cf. Fig. 2.5). Based on the idea of independently fluctuating membrane patches of the size ξ_{\parallel}^2 (postulated by Helfrich (1978)), multiple patches within the contact area of a vesicle are analyzed, as denoted for one patch in Fig. 2.5a. The patch size is chosen to 0.12 μm^2 , since this is about the square of the in-plane correlation length $\xi_{\parallel} < 1070$ nm according to Eq. (2.8) with $\kappa = 100 k_B T$. The mean intensity of the patch is measured as a function of time.

The positions of the patches analyzed are chosen arbitrarily. However, the distance to the boarder of the contact area is always chosen larger than 2ξ , so that perturbations by the free membrane region can not be effective. Further, the smallest distance between two adjacent patches is at least 3ξ to guarantee the measurement of independently fluctuating membrane patches.

According to Eq. (1.4), the obtained different intensity series can be transformed into height-series, assumed that the maximum and minimum intensities, I_{min} and I_{max} is fixed. To determine the extreme values the intensity distributions of entire RICM micrographs as shown in Fig. 2.6 are analyzed. A value at the lower and higher end of these distributions is determined to I_{min} and I_{max} , respectively. Note that single values of the intensity trace can exceed the extremal values due to the motion of the membrane (cf. below), which will lead to an undefined value in Eq. (1.4). Setting those values to I_{min} or I_{max} , respectively, yields a well defined time series

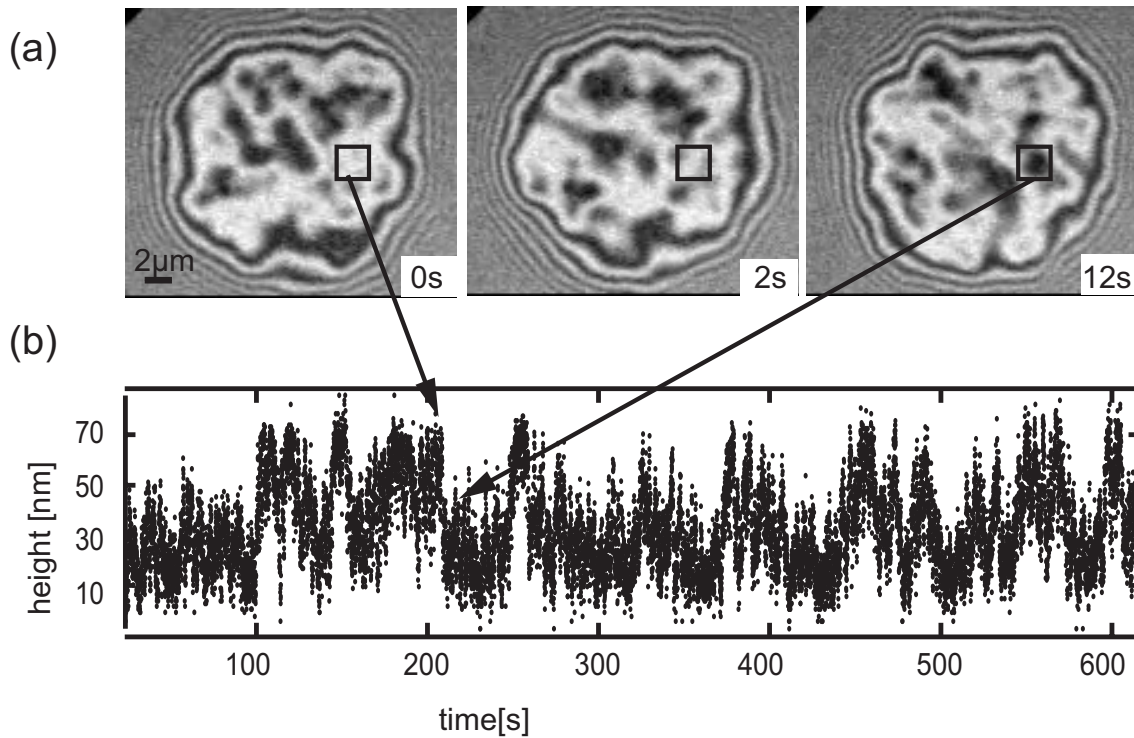


Figure 2.5: a) RICM interferograms of a giant vesicle (50 mol% DEPC, 50 mol% cholesterol) at three consecutive times. The grey scale pattern is changing in time due to fluctuations of the substrate-membrane distance (cf. framed area) b) Time series of the height of the membrane above the substrate, as obtained from Eq. (1.4) for the RICM interferogram within the framed area in (a).

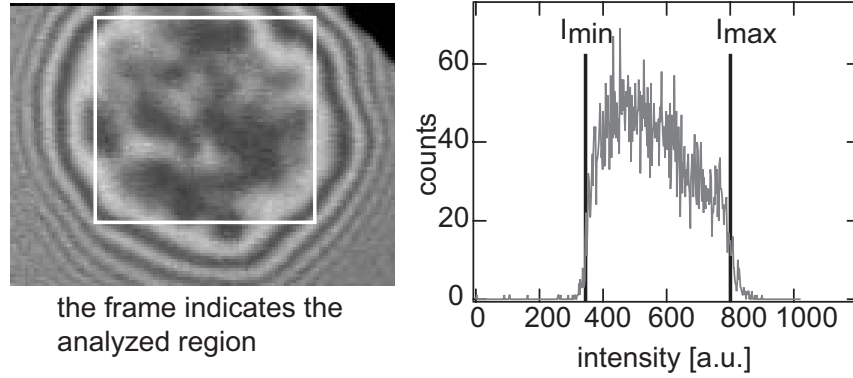


Figure 2.6: From a square of the contact area in the RICM micrograph (left hand side), the intensity distribution is analyzed (shown in the graph on the right). The upper and lower values of the distribution determine the intensity minimum value I_{min} and the intensity maximum value I_{max} .

of the membrane height $h(t)$, i.e. the height of the membrane as a function of time (cf. Fig. 2.5b).

Probability Distributions

In order to compare height-traces at different positions of the contact area and from different vesicles, the histogram of the height series was calculated. The probability distribution $P(h)$ obtained enables us to compare our data with theoretical predictions of the interaction potential.

In the evaluation we fitted each height distribution to Gaussian curves $y = \frac{W}{w} \exp\left[-\frac{1}{2} \frac{(h-h_0)^2}{w^2}\right]$. Each of the values obtained for the weight $\frac{W}{w}$, the rms width w and the position of the height h_0 were subsequently averaged to obtain a mean distribution. Finally in order to compare height-series with different numbers of data points the area of the distribution was normalized to one. In a control evaluation, we superimposed the different histograms first, in such a way that the increase in height for the different histograms was congruent. We fitted Gaussian curves to the mean histogram, which agreed well with the mean curve obtained from the fitting routine described earlier.

A difficulty arises in calculating the histogram around the height of 100 nm. Since a decrease in intensity can result either from an increase or a decrease in the membrane height, the intensity values are ambiguous due to the periodicity of the interference technique as discussed in the previous chapter. To avoid the misassignment of intensity values we confirmed that the height fluctuations are below 100 nm by a careful observation of the time series in the RICM micrographs. Measurements of the intensities by two different wavelengths, as discussed before, confirmed this in a set of reference experiments. However, in some exceptional cases the membrane

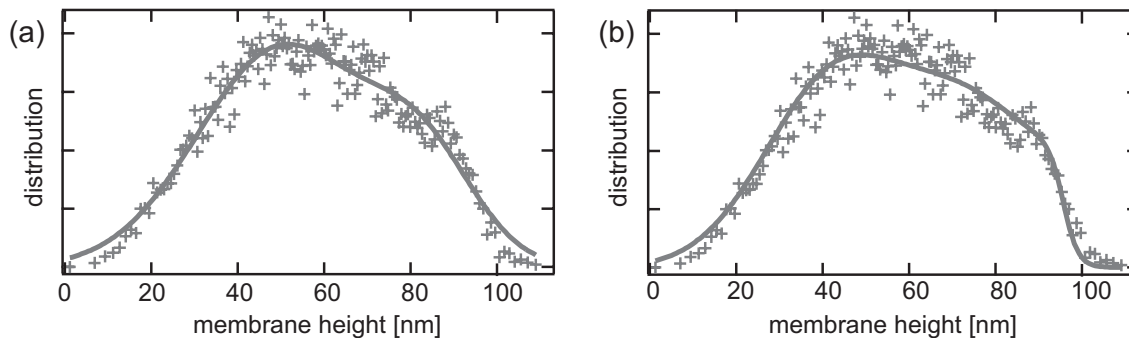


Figure 2.7: a) Fitting of a double Gaussian curve to the measured height histogram. b) Double Gaussian fit to the data with the corrected fitting routine.

is still deflected by more than 100 nm, and the height h is consequently assigned to an incorrect value. The assignment to the smaller h leads to a sharper decay of the height histogram at the height of about 100 nm than it would appear by a proper assignment of the data points. This mistake can be accounted for by the fitting routine and a much better fitting of the Gaussian curve to the data could be obtained as shown in Fig. 2.7b. Details of the fitting routine are given in the PhD thesis of Schilling (2003).

Experimental Constraints

Noise The noise of the camera and the light source can be determined by reading out the intensity of the substrate, i.e. an area with no membrane. The "height-trace" of the substrate is given in Fig. 2.8a and the "histogram" in Fig. 2.8b. Since the substrate is not moving, the height variations measured are attributed to the noise of the signal which is about ± 2.6 nm. Therefore, the error in determining the membrane height is at least as large as the signal noise.

Since the membrane is moving during the time a single picture is taken, the measured height is a mean value with a noise due to the membrane velocity. This velocity will be discussed below.

Further constraints in the accuracy of the height determination occur from the membrane reflectivity which may change by density fluctuations within the membrane or by the membrane curvature. However, due to the quite similar refraction indices of lipids and cholesterol it is not expected that a possible phase separation between lipids and cholesterol will lead to a large change in the reflectivity. Also, concentration fluctuations of the PEG lipid are expected to have a negligible effect on the reflectivity of the membrane since PEG polymers in water have a similar refraction index as water. The influence of the slope m on the interferogram can be neglected as long as $m \leq 30^\circ$, according to Wiegand et al. (1998). Within the

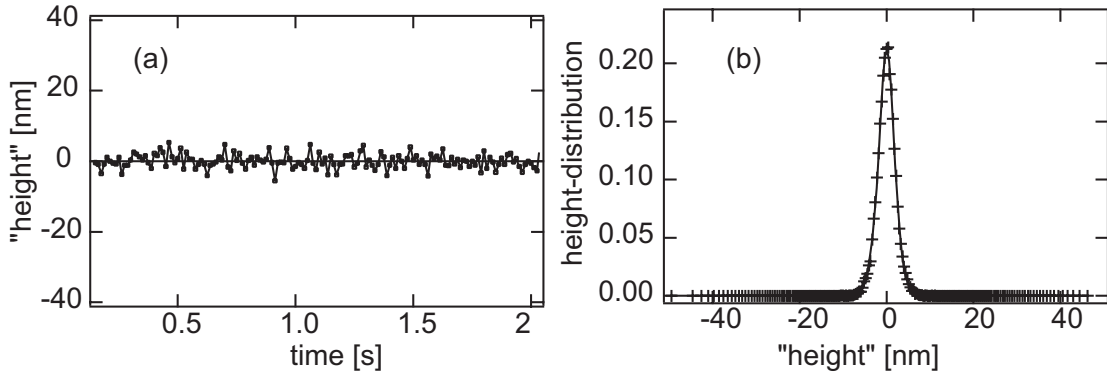


Figure 2.8: a) Time series of the recorded intensity changes of an area of the substrate. Since the substrate is not moving, the changes are due to lamp and camera noise of the setup. b) Histogram of the "height distribution" calculated from the "height-trace" shown in (a). The rms width is equal to ± 2.6 nm

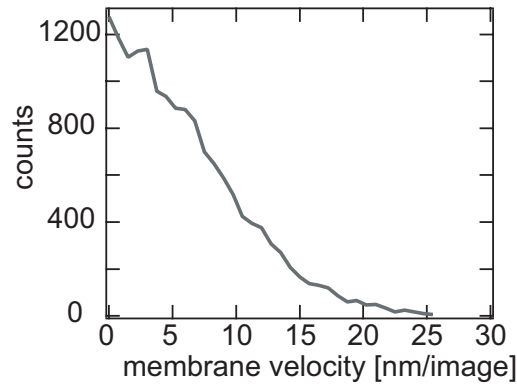


Figure 2.9: Histogram of the membrane velocity of a weakly adhering vesicle within the contact area with a substrate. The velocity is calculated as height change per image (recording frequency 71.9 Hz).

contact area the macroscopic slope is estimated to be smaller than $m = (14 \pm 2)^\circ$ which corresponds to approximately 100 nm height per 400 nm lateral distance. However, microscopic rafts within the bilayer may exhibit slopes larger than that and consequently give rise to a perturbation which is difficult to estimate. Clearly, it will increase the noise on the data.

Time Resolution

The time resolution of the setup is mainly determined by the sensitivity and the read out process of the camera. By limiting the read out region of the chip (approximately 6000 pixel) and integrating over 4 adjacent pixels (2 fold binning), a time resolution

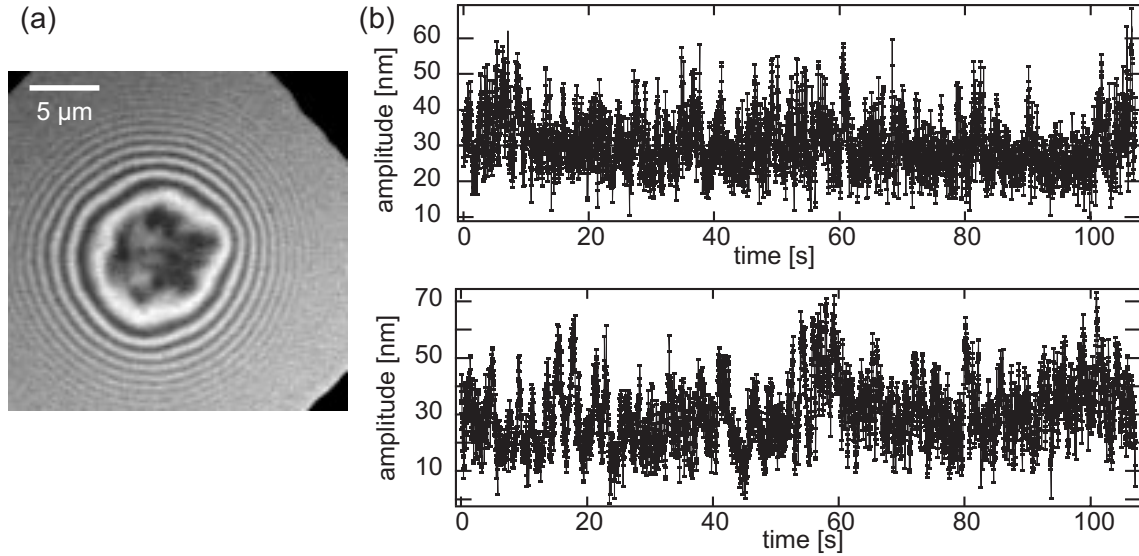


Figure 2.10: a) RICM micrograph of a pure DEPC vesicle adhering weakly on a glass substrate. b) Two different height-traces of two membrane patches within the contact area of the vesicle recorded over time.

of 100 Hz is obtained with the present setup. In order to confirm that the recording frequency is fast enough to follow the fluctuations of the membrane, the velocity v of the membrane is determined by analyzing the height change between two subsequent micrographs. The obtained distribution $P(v)$ shown in Fig. 2.9 has a mean velocity of $\bar{v} = 6.4$ nm per image = $0.71 \mu\text{m s}^{-1}$. Since the rms width of the measured potentials is expected to be around 25 nm (according to Eq. 2.9), the membrane can be resolved at multiple positions, while it is moving around in the potential well. Therefore the time resolution is fast enough to probe the potential. However, the measured potential is expected to be some nanometer wider than the real interaction potential due to the velocity of the membrane.

2.4 Results

2.4.1 Single-Component Membrane

Fig. 2.10a shows a RICM micrograph of a weakly adhering single component vesicle (pure DEPC membrane) to a glass substrate. The contact area is nearly circular and exhibits a rather homogeneous gray intensity. In Fig. 2.10b the time series of the membrane height over the substrate is displayed for two membrane patches within the contact area of the vesicle. From these height-traces the histogram of Fig. 2.11 is calculated, showing the probability distribution of the heights for the lower time series in Fig. 2.10b. By fitting a Gaussian curve to the measured histogram, the rms width is determined to $w = (25 \pm 6)$ nm and the mean spacing $\langle h \rangle$ from the substrate

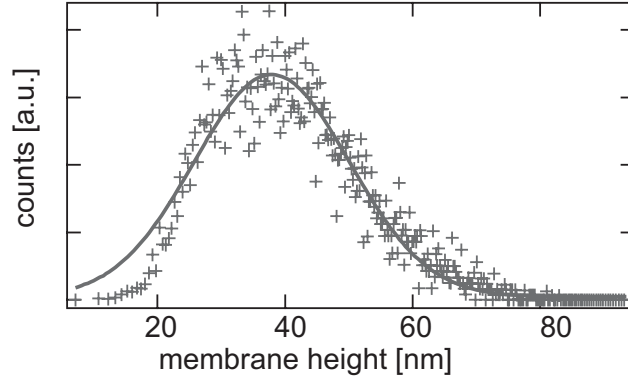


Figure 2.11: Histogram of the height distribution of a pure DEPC vesicle adhering weakly to a glass substrate. The crosses show the data, whereas the line is a Gaussian fit. The histogram was calculated from the lower height-trace in Fig. 2.10.

which is equal to the membrane height is $\langle h \rangle = (50 \pm 15)$ nm. In the following a comparison between these measured values with theoretical predicted ones will be considered. The predicted mean spacing $\langle h \rangle$ can be determined by equating the gravitational force on the vesicle with the Helfrich force (derivative from Eq. 2.1 and from Eq. (2.3), respectively):

$$g\Delta\rho V_V = -A_C \left[\frac{dV_{He}(h)}{dh} \right]_{h=\langle h \rangle}, \quad (2.11)$$

where A_C is the contact area with the substrate. By solving this equation for the mean height $\langle h \rangle$ one obtains:

$$\langle h \rangle = \sqrt[3]{\frac{2c_{fl}(k_B T)^2 A_C}{\kappa g \Delta\rho V_V}}, \quad (2.12)$$

with the dimensionless collision energy $c_{fl} = 0.116$ (Lipowsky and Zielinska 1989) and the density difference $\Delta\rho = 50 \text{ kg m}^{-3}$. The volume of the vesicle, which is assumed to be spherical, can be calculated from the radius $r_V = (17 \pm 2) \mu\text{m}$. This is measured by bright field microscopy. The contact area A_C is determined in the RCM micrograph from the measured contact radius $r_C = (5 \pm 0.5) \mu\text{m}$. Inserting these values into Eq. (2.12) gives the mean height $\langle h \rangle = (65 \pm 5)$ nm of the membrane. This theoretical prediction is reasonably consistent with the measured value of the height distribution $\langle h \rangle = (50 \pm 10)$ nm.

Further the theoretically predicted rms width $w = 1/\sqrt{5} \langle h \rangle$, cf. Eq. (2.9), is determined to $w = 28$ nm, with $\langle h \rangle = (65 \pm 5)$ nm, which is consistent to the experimentally determined value $w = (25 \pm 6)$ nm. These estimates show that our experimental results for a single-component lipid bilayer appear consistent with the theory of Leibler and Lipowsky (1987).

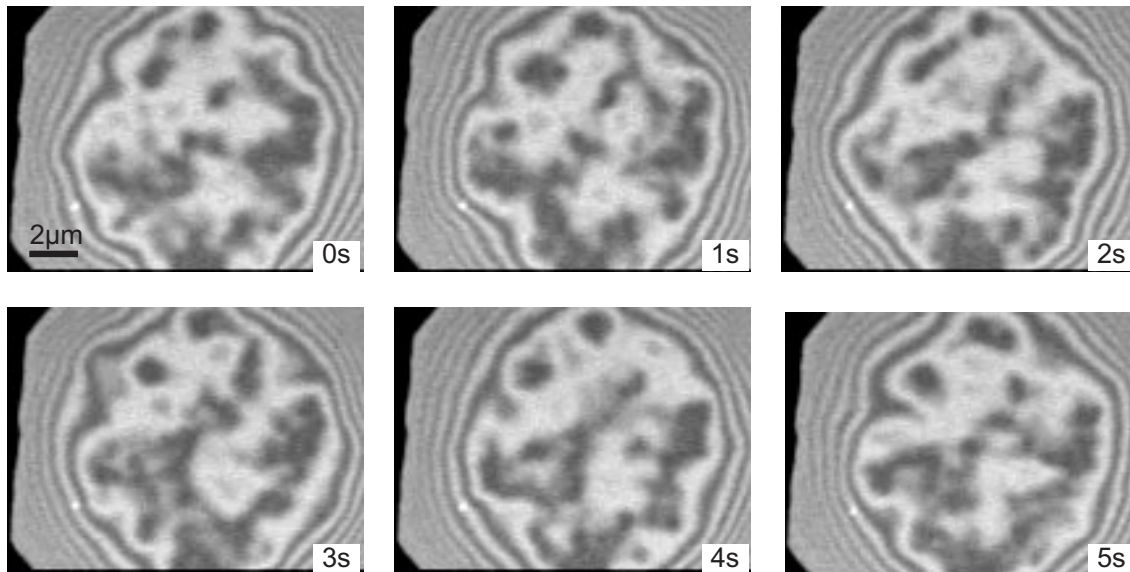


Figure 2.12: Time series of subsequent RISM micrographs, which show a change in the interference pattern within the contact area – i.e. the changes in height due to the undulations of the membrane. The vesicle membrane is composed of 99 mol% DEPC and 1 mol% PEG lipid and is weakly adhering to glass. The pictures have been taken from a sequence, which was recorded with 100 Hz for 6 min.

It should be noted, that the experiments where no additional PEG was added to the membrane to suppress unspecific adhesion of the vesicles are difficult to perform. Often unspecific adhesion occurs and attaches the vesicle locally to the substrate, which leads to a perturbation of the free flickering of the membrane. Another problem arises from the budding of vesicles. The vesicle loses some excess area by small buds which can form within the vesicle membrane and finally disconnect from the vesicle. The budding probability is observed to increase if the vesicles adhere locally. Unfortunately, the formed buds might be too small to be resolved in the RISM. However, the formation of many of them results in a higher tension of the vesicle membrane. The ratio Q of the diameter of the vesicle to the diameter of the contact area increases with increased tension and is a simple check for the tension. Only vesicles exhibiting a ratio between $Q = 2 \dots 3.5$ are analyzed and effects of budding are thus tried to be excluded from the experiments.

2.4.2 Multi-Component Membrane

In Fig. 2.12 RISM micrographs of a giant vesicle, composed of 99 mol% DEPC and 1 mol% PEG lipid are shown at consecutive times. In the contact area a "leopard-skin" like texture (black-and-white regions) is observed with a characteristic length scale Δx of about 1 to 2 microns. The black and white texture in the contact area

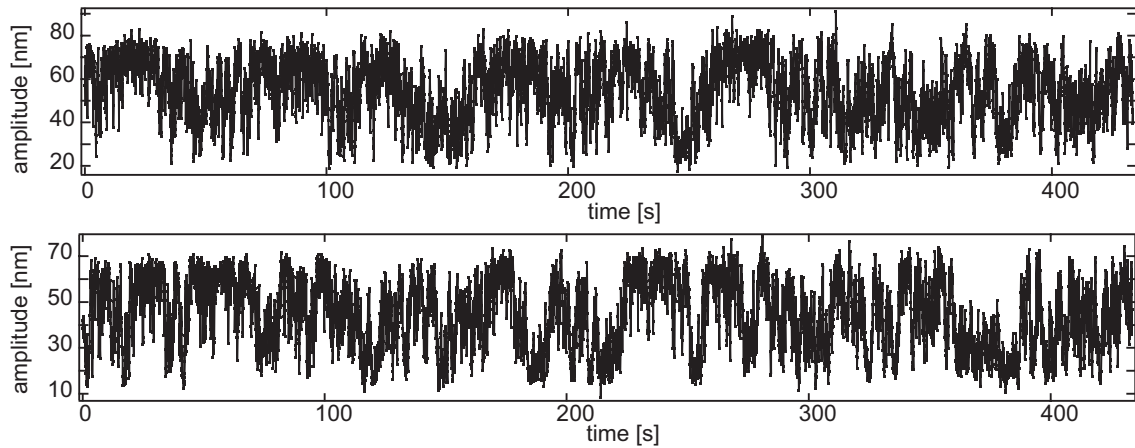


Figure 2.13: Time series of the spacing between substrate and membrane obtained by an inverse cosine transformation of the intensity of membrane patches from the RICH interferogram of Fig. 2.12. The multi-component vesicle membrane consists of 99 mol% DEPC and 1 mol% PEG lipid.

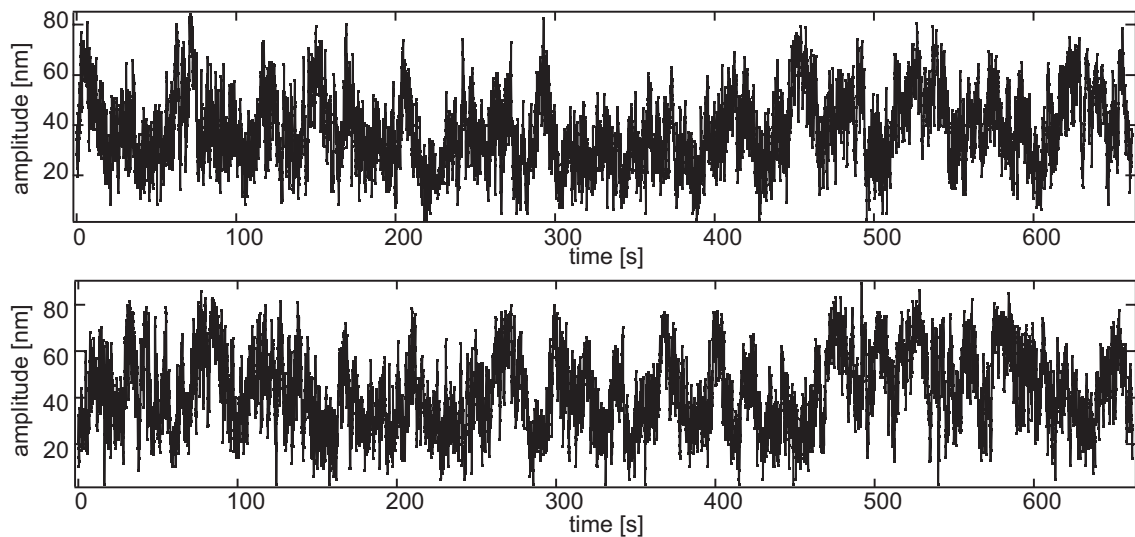


Figure 2.14: Time sequence of height fluctuations of membrane patches from a vesicle above a glass substrate. The vesicle membrane consists of 49,5 mol% DEPC, 49,5 mol% cholesterol and 1 mol% PEG lipid.

is totally different from the grey contact area observed for a pure DEPC membrane (cf. Fig. 2.10a) and the appearance of a length scale of one micron is unexpected since the in-plane correlation length is $\xi_{\perp} = 540$ nm for fluid DEPC membranes with a bending stiffness $\kappa = 25 k_B T$, according to Eq. (2.8) (Gennis 1989).

Fig. 2.13 shows the time series of the membrane height for two different membrane patches consisting of a 99 mol% DEPC and 1 mol% PEG lipid. In Fig. 2.14 the height-trace of a vesicle with 49,5 mol% DEPC, 49,5 mol% cholesterol and 1 mol% PEG lipid is given. For all time series the vesicle membrane appears to stay mainly in two height regions, a lower one between 10 to 40 nm and the higher one ranging from 50 to 80 nm. Within these two "sub-states" rapid fluctuations take place, while the membrane switches slowly between the two sub-states. By calculating the height fluctuations δh within a sub-state one finds $\delta h \sim 30 \dots 40$ nm. A comparison with the typical size of the height fluctuations in a bound state of $\delta h \sim 3 \dots 5$ nm at heights h^* , demonstrates that the bilayer is in an unbound state in both "sub-states" (Bruinsma et al. 2000). A more detailed comparison between the time series of Fig. 2.13 and Fig. 2.14 reveals that in the first figure, where the membrane is free of cholesterol the two sub-states are more separated in height and appear therefore more pronounced than in the latter.

To compare different time series, the height distributions were plotted in histograms. Exemplary in Fig. 2.15 the height distribution $P(h)$ for a vesicle consisting of 50 mol% DEPC and 50 mol% cholesterol is shown. It is clear that this distribution cannot possibly be fitted by a Gaussian curve. The behavior of the membrane is clearly different from fluctuations around one mean value $\langle h \rangle$ as observed for a single component membrane (cf. Fig. 2.11) and suggested by the theoretical approach of Leibler and Lipowsky (1987) for an unbound membrane. The broad bimodal height distribution corresponds to the two sub-states observed in the height traces and the black and white texture exhibited in the contact area of the RICM micrograph.

In fact, none of the probability distributions associated with the multi-component systems could be fitted by a single Gaussian, as shown in the mean histograms of different membrane compositions plotted in Fig. 2.16. The measured distributions could however be fitted by the sum of two Gaussian curves:

$$P(h) \propto \frac{W_I}{w_I} \exp \left[-\frac{1}{2} \frac{(h - h_I)^2}{w_I^2} \right] + \frac{W_{II}}{w_{II}} \exp \left[-\frac{1}{2} \frac{(h - h_{II})^2}{w_{II}^2} \right], \quad (2.13)$$

where the fitting parameters $h_{I,II}$ and $w_{I,II}$ correspond to the mean height and the rms width of the two states, respectively, while the $W_{I,II}$ are the corresponding statistical weights. It is important to emphasize that the two peaks, denoted by I and II, can be identified both with the black-and-white regions of Fig. 2.12 and with the two sub-states in the time-series of Fig. 2.13 and Fig 2.14. The fitting to a double Gaussian curve is a general method to compare different height traces. Additionally, the fit does not depend on any limit or offset added during the evaluation and accounts for the behavior of a membrane in each sub-state.

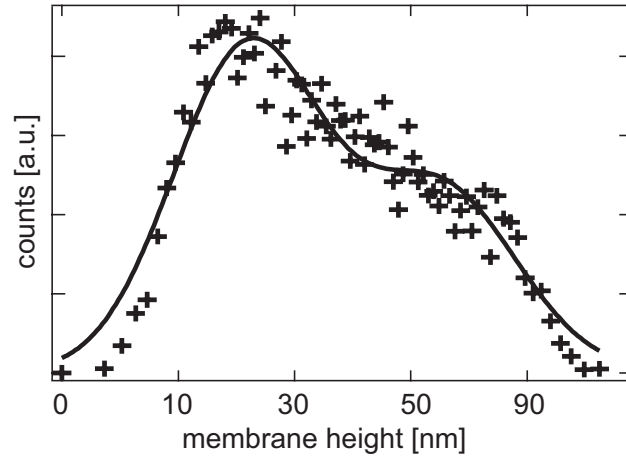


Figure 2.15: A typical probability distribution $P(h)$ of the substrate-membrane spacing obtained from time series of a DEPC bilayer with 50 mol% cholesterol and 0 mol% PEG. The markers are the data points and the line is a fit to the data using Eq. (2.13).

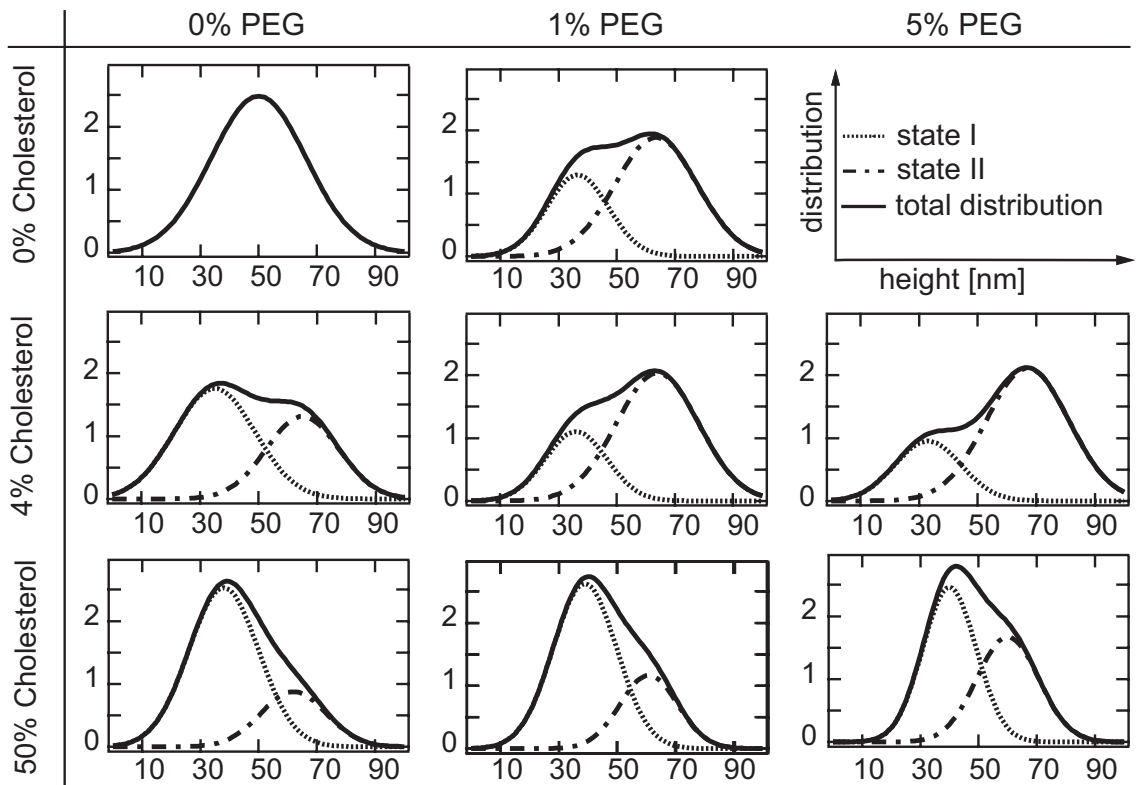


Figure 2.16: Fitted probability distributions $P(h)$ of the substrate-membrane spacing for various values of the PEG-lipid concentration (0 mol%, 1 mol% and 5 mol% PEG) and the cholesterol concentration (0 mol%, 4 mol% and 50 mol%) in a DEPC bilayer.

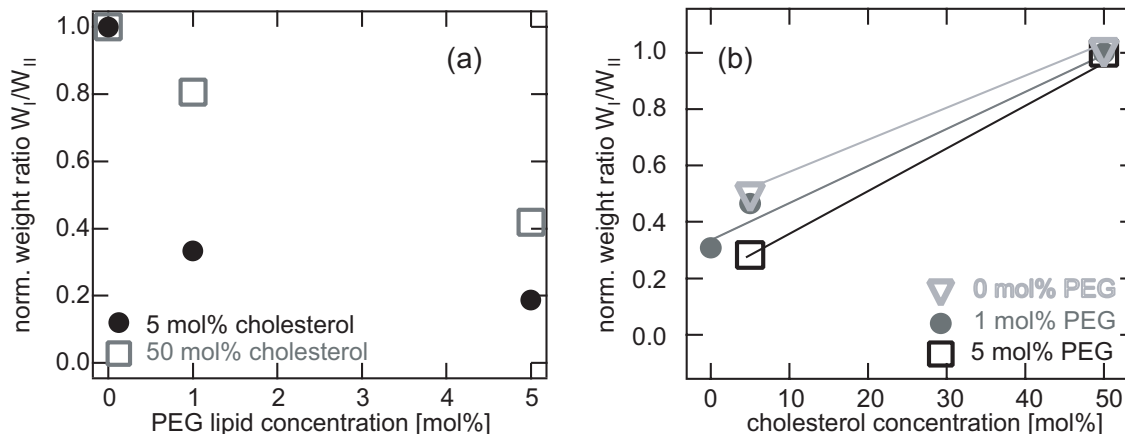


Figure 2.17: a) Normalized weight ratio of the two Gaussian peaks versus the PEG concentration for 5 mol% cholesterol and 50 mol% cholesterol. b) Weight ratio displayed versus the cholesterol concentration for the three different PEG concentrations (0 mol%, 1 mol% and 5 mol%).

To elucidate the influence of the different additives the membrane composition was changed systematically. As shown in Fig. 2.16, the peak positions of h_I and h_{II} always straddle the mean spacing of the single-component bilayer and are relatively independent of composition. For the first and second row, the widths also do not vary significantly, and remain comparable to the rms width of $P(h)$ for the single-component bilayer (about 25 nm).

However, the weight ratio W_I/W_{II} of states I and II is very sensitive to the membrane composition. Consider first the case of fixed cholesterol content (4 mol%, second row of Fig. 2.16) and varying lipopolymer fraction. The relative weight W_I/W_{II} of the first peak is reduced to 0.25 of its initial value by a 5 mol% increase in lipopolymer fraction, cf. the black circles in Fig. 2.17a. This indicates that there exists distinct lipopolymer-poor (I) and lipopolymer-rich (II) states, such that increasing the lipopolymer fraction increases the relative weight of state II over state I.

For fixed PEG-lipid contents and varying cholesterol contents (cf. columns of Fig. 2.16), we observe a similar scenario, except that the weight ratio W_I/W_{II} dramatically increases with cholesterol content, as shown in Fig. 2.17b. Therefore it is now state I that is enriched in cholesterol.

The different effect of the two additives is physically reasonable since lipopolymers act as repellers that favor a state with a larger spacing whereas the increased stiffness of a cholesterol-rich section makes thermal fluctuations energetically more costly and hence favors a state with a smaller spacing.

A difference in the overall width of the height histograms is clearly observed: for the first two lines in Fig. 2.16 the distribution is about 70 nm wide, whereas for the third line the width is only about 50 nm. This finding was already noticed by

comparing the two time series of Fig. 2.13 and 2.14, since for the membrane without cholesterol the two sub-states appeared more separated in height. The difference can be understood in terms of the change of the bending stiffness κ . For high cholesterol contents κ increases by a factor of 4 to $\kappa = 100k_B T$, which results in a stronger damping of the fluctuations (Cevc and Marsh 1987).

2.4.3 Change of the Specific Weight

In a different set of experiments we reduced the specific weight of the vesicles to control the influence of gravity on the height distribution of the membrane. This could be achieved by swelling the vesicles in a glucose solution, which has a lower density than the sucrose solution used before. Thereby the density difference between the inner and outer liquid is reduced to ($\Delta\rho = 20 \text{ kg m}^{-3}$). In the micrographs of weakly adhering "light" vesicles one observes again the leopard like texture, suggesting a phase separation between inclusion rich and inclusion poor regions. From a time sequence of those micrographs it is noticed that the vesicles is flickering around a higher mean spacing compared to the previous experiments, making a non-ambiguous height determination with the single wavelength technique impossible. This observation is consistent with the theoretically expected estimate of the mean-height $\langle h \rangle = 89 \text{ nm}$ according to Eq. (2.12).

2.4.4 Passivation of the Substrate

Further we changed the thickness and the quality of the passivating film on the surface. By reducing the incubating time of the BSA solution with the substrate, one expects to obtain a less dense layer of proteins on the surface and therefore an increased vdW attraction. Fig. 2.18 shows the mean height histogram of a membrane consisting of 94 mol% DEPC, 5 mol% cholesterol and 1 mol% PEG lipid on a substrate passivated for 10 s. On the right hand side of the figure the mean histogram for vesicle of identical composition adhering on a surface passivated for 1 h. A comparison reveals that for the shorter incubation time, the ratio W_I/W_{II} is large since state I is dominant, whereas for the longer incubation time the ratio is small as state II outweighs I. Additionally, the width of the two Gaussian curves are reduced for the shorter incubation time. Both observation can be explained intuitively by the stronger vdW interaction which results from the reduced incubation time. By increasing the vdW interaction, the membrane is expected to be more often in the lower sub-state and the flickering is reduced by the stronger attraction, which results in a more narrow potential.

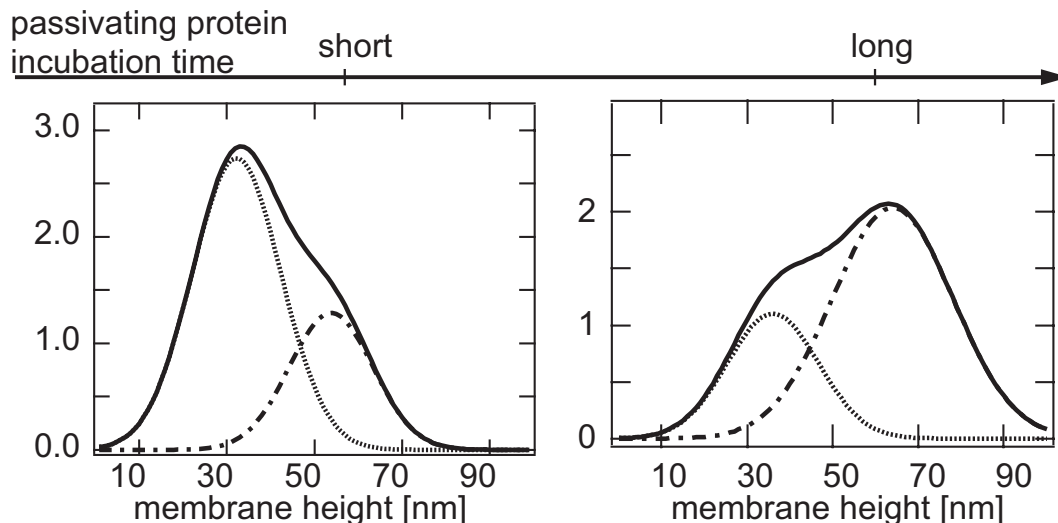


Figure 2.18: Averaged histograms of the heights of identical vesicles consisting of 94 mol% DEPC, 5 mol% cholesterol and 1 mol% PEG lipid, adhering weakly to substrates which have been passivated for different periods. The short incubation time was about 10 s whereas the long incubation time was an hour.

2.5 Discussion

The flickering analysis in the RICM provides a technique to probe the interaction potential of a membrane and a substrate. The real time observation of the membrane heights enables one to investigate in detail the behavior of the membrane.

For the single component bilayers the observed Gaussian distribution of the height can be explained by a second order transition between a bound and an unbound state. As in the experiment the interaction between the single component membrane and the substrate is not changed, the phase transition is not crossed. The shape of the distribution as well as the specific values for the single component bilayer are consistent with the theory of Leibler and Lipowsky (1987) (LL).

However, for all the multi-component vesicles, the appearance of a the leopard-skin texture, the time-series switching between two sub-states, and the double-peak structure are rather unexpected (cf. Figs. 2.12-2.16). Because of the universal nature of the collision energy, the predicted single-peak distribution of LL should apply to multi-component bilayers as well, provided the bilayer is homogeneous at sufficiently large length and time scales. Even in the presence of lateral phase separation within the membrane the mean spacing of the bilayer depends only on an effective, renormalized bending energy $\kappa(C)$, with C the surface concentration of the additives. For a symmetric lipopolymer layer with additives exhibiting a radius of gyration $R_g = 3$ nm it is predicted that κ changes to $\kappa(C) = \kappa + k_B T C R_g^2$ (Hiergeist and Lipowsky 1996). Assuming lateral phase separation of C , one finds a change in κ

smaller than 0.5% (for $\kappa = 25 k_B T$). According to Eq. (2.12) the resulting difference of 1 nm in the peak position is much too small to explain the observed probability distribution. Therefore, the continuous unbinding transition can not describe the experimental observations.

The observed coexistence of the two unbound states within the membrane is a strong suggestion for a first order phase transition. Additionally, a first order scenario for the phase transition is required to account for the characteristic length-scale $\Delta x \approx 1 \mu\text{m}$ of the leopard-skin texture and the multiple time scales in the time series of the multi-component membrane. While the presented experiments were performed there existed two studies of the unbinding transition, based, respectively, on the renormalization group method (Netz and Pincus 1995) and a Landau Free Energy expansion (Milner and Roux 1992), indicating that the phase-diagram may contain a line of first-order transitions ending at a tricritical point, where the region of second order transition starts. Our observations could be interpreted assuming that the single-component bilayers are in a regime of continuous unbinding transitions while multi-component systems are characterized by thermal fluctuations between an unbound state and a large $\langle h \rangle$ bound state, as expected close to the tricritical point. The observation of two large correlation lengths - the parallel correlation length ξ and the characteristic length-scale Δx of the dynamical phase separation - also may be consistent with tricritical behavior, as is the observation of multiple time-scales in the time series. If the Landau theory is extended by including the additive concentration as a second degree of freedom that is coupled to the bilayer concentration one finds that this indeed generically favors the first-order transition scenario. However, this interpretation assumes that the experiments are performed very close to the tricritical point. Confirmation of this interpretation would require a more extended experimental study - since two thermodynamic parameters must be independently varied to fully investigate a tricritical point - as well as more theoretical insight in the nature of spacing fluctuations near an unbinding tricritical point.

A simpler explanation for the observed situation might arise from the Helfrich interaction. Since in the used concentrations of the PEG lipids and cholesterol the additives are found to be soluble in free lipid monolayers (Gennis 1989) with no tendency to phase-separate, the observed coexistence of two states, must be attributed to the Helfrich repulsion. Possibly the Helfrich repulsion mediates a long-range interaction if the additives couple to the membrane curvature or bending stiffness as depicted in Fig. 2.19. In the figure the depicted cholesterol additives assemble at domains of a smaller membrane substrate spacings.

A theoretical study of Helfrich repulsion in multi-component bilayers by Netz (1995) indeed predicted that the coupling between membrane curvature and the concentration C of foreign inclusions leads to a lateral phase separation, even at extremely low concentration. In contrast to these studies, we did not find that the statistical properties of the times-series depend on the position chosen within

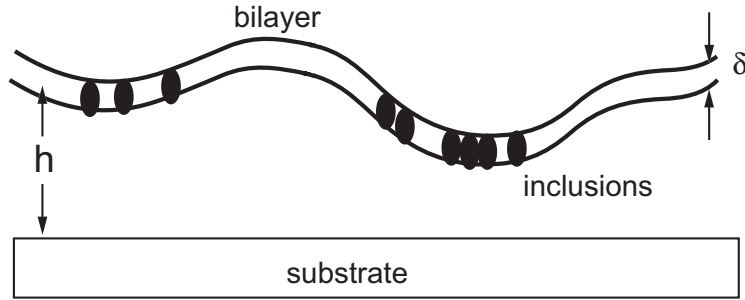


Figure 2.19: A fluid membrane with additives (black filled ovals) adhering to a substrate. The height of the membrane is denoted by h and its thickness by δ .

the contact area. This shows that there is no true, macroscopic or static phase-separation between inclusion rich and inclusion poor regions. Therefore a "dynamical" phase-separation between the different states induced by Helfrich repulsion could be a possible explanation. The recently published theory of Komura and Andelman (2002), which combines the unbinding transition and the lateral phase separation in multi-component membranes supports this idea. The lateral phase separation of inclusions affects the second virial coefficient of the unbinding transition, which accounts for the interaction between the membrane and the substrate. It was shown that the phase separation is enhanced by the adhesion of membranes compared to free membranes. The theory can successfully describe a first order phase separation between two unbound states for a given interval of temperature and interaction energy as observed in our experiments. The phase separation between the bound and unbound membrane remains of second order above a critical temperature T_{cr} as predicted by Lipowsky and Leibler (1986). Below T_{cr} the transition is discontinuous as predicted in the work of (Milner and Roux 1992, Netz 1995). However, the gravitation is not included into the theory so far and it is not yet clear, whether the two unbound states would be expected to be at two different heights.

2.6 Conclusions

In summary, we find that multi-component lipid bilayers near a substrate exhibit a dynamical form of phase-separation and that the classical theory of unbinding unambiguously is not sufficient to account for our observations. The collision energy of a multi-component bilayer is not a universal quantity, since we find that the fluctuation spectrum is characterized by two length-scales and multiple time-scales. This is reminiscent of the type of fluctuations encountered close to a tricritical point, where a line of continuous transitions changes into a line of first-order transitions. Another possible origin of the breakdown of the universality of the collision en-

ergy might arise from the Helfrich collisions which can possibly mediate an effective long-range interaction between concentration fluctuations. The coupling between membrane curvature and the additive concentration C , as proposed in the theoretical approach of Komura and Andelman (2002) can be a possible mechanism, cf. Fig. 2.19.

Apart from the challenge to describe the experiments within the existing theoretical framework of the unbinding transitions, the results of this chapter might have interesting applications for biomembranes. The plasma membrane of cells is homogeneously covered by a coat of (mobile) lipopolymer repeller molecules (Lodish et al. 2000). It is known that very low concentrations of adhesion molecules are able to produce tight adhesion between two cells, without being interfered by the polymer coat. The surprising ability of Helfrich collisions to produce local phase separation in multi-component membranes, which otherwise are thermodynamically stable, might provide a mechanism for the spontaneous formation of contact sites free of lipopolymers.

Chapter 3

Model System for Cell Plasma Membranes

3.1 Introduction

Cells are the main building blocks of the biological universe. They are the smallest self-sufficient and basic unity of all life. Cells are delimited by an outer boarder, called cell plasma membrane. It keeps the interior content from leaking out into the surrounding environment and has important functions such as carrying functional proteins, releasing signal molecules, and storing energy (Alberts et al. 1994, Voet et al. 1995). A widely accepted understanding of the cell plasma membrane is the *fluid mosaic model* introduced by Singer and Nicolson (1972) (cf. Fig. 3.1). In this model the cell plasma membrane is represented by a lipid bilayer of phospholipid and cholesterol molecules. The word *mosaic* describes the made up of membranes

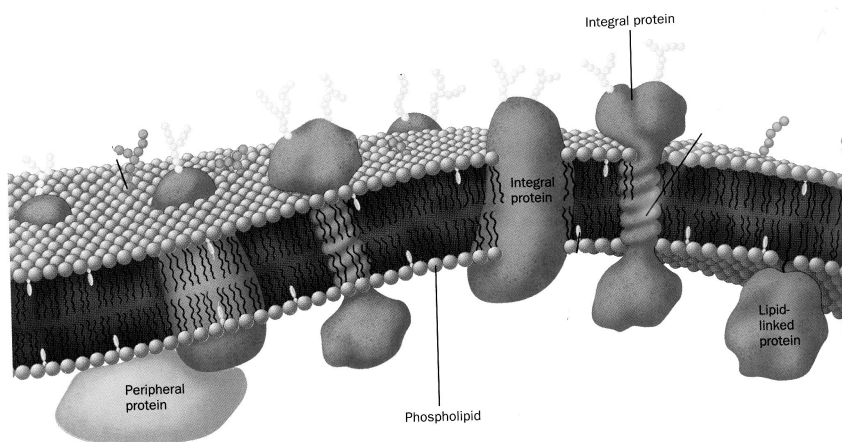


Figure 3.1: Sketch of a cell plasma membrane as described in the fluid mosaic model by Singer and Nicolson, Voet (1995). The phospholipids form a two-dimensional bilayer where the proteins are incorporated or attached to.

of numerous different lipids and proteins and *fluid* emphasizes the ability of lipids and proteins to diffuse within the membrane. Therefore proteins can reach regions where e.g. signal molecules are released, which provides a higher efficiency for local biochemical reactions. Over the years the fluid mosaic model has been improved taking lateral phase separation of the multi-component membrane and aggregation of proteins into account.

To understand the properties of the cell plasma membrane, cell models are developed which mimic the plasma membrane. One simple model is a lipid bilayer of an artificial vesicle, which is fluid in two dimensions at the appropriate temperature range. The vesicle membrane - as the cell plasma membrane - may consist of different lipid molecules mixed with cholesterol. Proteins can be anchored by various techniques to the artificial membranes. A summary of the different possibilities to attach proteins is given in the following (Sackmann and Tanaka 2000): (1) Proteins can be coupled through linkers and spacers to the bilayer. A classical linker is the biotin-streptavidin system. However, since streptavidin has four binding pockets for biotin, these complexes tend to cluster and hinder the diffusion. More elaborated linkers are the reversible coupling via histidine tags and chelating groups (Schmitt et al. 1994). In these systems the mobility and density of proteins can be well controlled. (2) Transmembrane proteins possess a phospholipid binding domain enabling a direct reconstitution into lipid bilayers by adding surfactant-solubilized proteins to the lipids in an aqueous phase (Tank et al. 1982). (3) A recently developed strategy is to prepare specific binding domains for large proteins by genetic engineering or organic synthesis (Kantlehner et al. 1999), which allows an attachment of proteins to bilayers. Proteins anchored to the vesicle membranes by the techniques (1)-(3) are mostly mobile and can diffuse freely upon the vesicle membrane (Peters and Cherry 1952) - similar to proteins in the cell plasma membrane.

Despite all promising similarities between cell plasma membranes and artificial models, there is one serious drawback: experimental methods for studying a free membrane in 3 dimensions are quite limited. In contrast, if membranes are restricted to flat surfaces, a large variety of surface sensitive optical techniques and electrical measurements would be available, e.g. measurements of the diffusion constant in the bilayer, determination of the protein-protein binding energy and of the binding strength between binding partners, as well as the design of biosensors (Watts et al. 1986, Salafsky et al. 1996, Gritsch et al. 1998, Wong et al. 1999). Therefore, the development of planar artificial membranes - the so-called solid supported bilayers - was a big achievement (Brian and McConnell 1984, Sackmann 1996). There, the lipid bilayer is supported and stabilized by a solid substrate and separated from it by a thin, lubricating water layer. Flat bilayers can be assembled by spreading small unilamellar vesicles onto solid surfaces (Kalb et al. 1992). The only prerequisite for such a process is a smooth and hydrophilic surface. Thus supported bilayers can be formed on many surfaces like glass, plastic and semiconductor substrates (Boxer 2000, Keller et al. 2000, Hillebrandt and Tanaka 2001, Nissen 2001). Unfor-

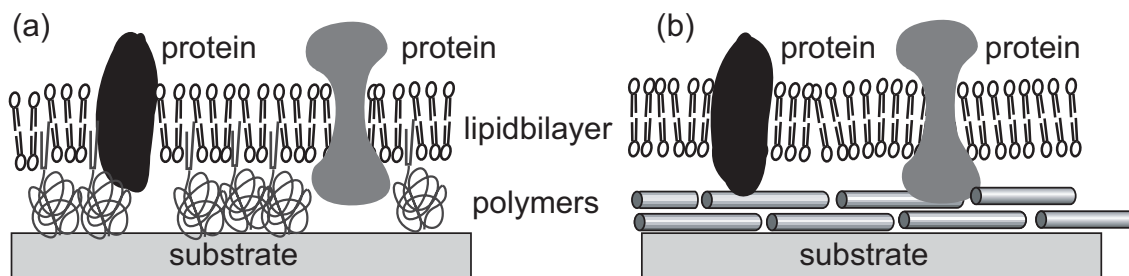


Figure 3.2: a) Cartoon of a lipid bilayer with incorporated transmembrane proteins supported by polymer coils. b) Sketch of a lipid bilayer with transmembrane proteins supported by a polymer film.

tunately, the fluidity of supported bilayers is preserved to lipids and small incorporated proteins, since the membrane is separated from the substrate only by a thin water layer (thickness ~ 1 nm). Incorporated proteins with larger domains sticking out off the membrane are immobile. Additionally, proteins often lose their functionality due to the contact with the hard inorganic support and denature. These problems are serious limitations for the model system, since adhesion molecules like glyco-proteins have domains up to 40 nm sticking out of the plasma membrane (cf. Fig. 3.1) (Bongrand 1999). To maintain the fluidity and functionality of large transmembrane proteins, different strategies have been proposed and are still under current study (Wegner 1993, Sackmann 1996). The general idea is to separate the membrane from the substrate by intercalating water swelling polymers. The supported membrane is then carried on such polymer coils or on polymer films, as shown in Fig. 3.2a and Fig. 3.2b, respectively. In order to obtain a thermodynamically stable polymer/lipid composite on solid substrates the wetting conditions have to be controlled carefully. The complete wetting of the polymer on the solid substrate and of the bilayer on the polymer has to be established (Rädler and Sackmann 1997). Since these conditions are not easily fulfilled the number of possible polymers is quite limited. It can be increased by reducing the number of layers that can perform a dewetting e.g. through a chemical grafting of the polymers onto the substrate.

There are mainly three successful methods reported for the preparation of stable polymer/membrane composites. (1) The chemical grafting of a film of highly water soluble polymers, such as dextran or hyaluronic acid, to the solid surface and subsequent deposition of a lipid bilayer (Kühner et al. 1994, Kühner and Sackmann 1996). (2) Reconstitution of lipopolymers (water soluble polymers covalently linked to lipids) into the bilayer. In aqueous solutions these polymers swell and separate the bilayer from the substrate (cf. Fig. 3.2a) (Baeckmark et al. 1995, Heyse et al. 1995). (3) Deposition of multilayers of amphiphilic molecules (e.g. cellulose with alkyl side chains, so-called hairy rods) and the subsequent transfer of lipid layers, as depicted in Fig. 3.2 (Wegner 1992, Sigl et al. 1997).

To the obtained polymer supported membranes, proteins can be attached or incorporated, providing a versatile and promising model for cell plasma membranes. Accordingly, such supported membranes are used in a remarkable variety of fields:

- as a model for studying protein-protein interaction mechanisms (Brian and McConnell 1984, Tamm and McConnell 1985, Sivasankar et al. 1998),
- as target cells¹ to study the cell adhesion mechanism, (Sackmann 1996, Dustin 1997, Bruinsma et al. 2000)
- for the design of biosensors on electrical devices (Gritsch et al. 1998, Hillebrandt et al. 1999).

In this thesis we will focus on the use of supported membranes as model target cells to study the physical process of cell adhesion, namely the adhesion mediated by integrins.

3.1.1 Integrins

The family of integrin proteins are cell adhesion proteins and play a key role in many processes of life (Clark and Brugge 1995, Yamada and Geiger 1997, Horwitz 1998). Integrins are large transmembrane glyco-proteins consisting of one α subunit (molecular mass 120...180 kD) and one β subunit (molecular mass 90...120 kD). So far 22 different integrins have been identified. They are combinations of 15 different α and 8 different β subunits (Buck and Horwitz 1987, Hynes 1992, Alberts et al. 1994). Fig. 3.3 shows a schematic view of an integrin molecule. Both subunits have a large extracellular domain which binds to proteins of the extracellular matrix (ECM). The intracellular domain of the integrin receptor is very small and couples to proteins of the cytoskeleton². The coupling is regulated by transmitting signals upon the attachment of a ligand to the extracellular domain. The signaling cascade can also be triggered from the intracellular domain and thus control the adhesion of cells.

The ligand specificity of the integrins is quite complex, since one integrin can bind to more than one ECM protein. Additionally, a single ECM protein can bind to different ligands. Moreover, one cell normally expresses a manifold of different integrins, which demonstrates the high flexibility of integrins. Consequently members of the integrin family are involved in nearly all adhesion processes occurring in nature.

¹A model for the extracellular domain of cells. The model exhibits key properties of the cell surface, such as softness of the surface, fluidity, and functionality of extracellular proteins or protein fragments. It is best suited if all relevant properties of a cell surface are modelled.

²The cytoskeleton is an array of fibrous proteins inside the cell, which gives the cell rigidity, and helps to maintain the cell shape.

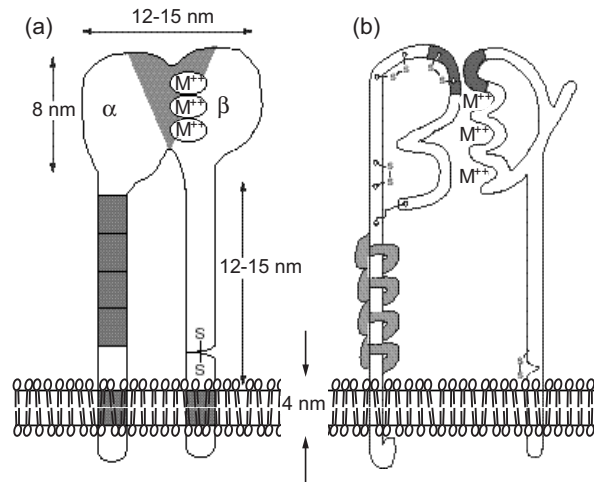


Figure 3.3: (a) Schematic view of an integrin receptor. The drawing is to scale, showing the size differences between the large extracellular domain and the small intracellular region. The lipid bilayer indicates the domain, where the receptor is penetrating the cell membrane. The gray area in the extracellular domain shows the ligand binding regions. The alpha and beta domain are linked via divalent ions (M^{2+}). b) Schematic view of the secondary structure of the integrin protein. The picture is taken from Hynes (1992).

For the following work the specific integrin $\alpha_{IIb}\beta_3$ is studied. It is the main receptor on human blood platelets and plays a critical role in thrombosis and haemostasis (Weisel et al. 1992, Craig et al. 1995). The protein has a molar mass of 230 kD and bears specific binding sites for fibrinogen, fibronectin, von Willebrand's factor and vitronectin (Hynes 1992). Integrin $\alpha_{IIb}\beta_3$ binds specifically to the amino acid sequence Arg-Gly-Asp (RGD)-sequence of these ligands. The binding constant of integrins is relatively weak ($k_D = 10^{-6}$ M). Thus for tight adhesion many integrins have to be involved.

3.1.2 RGD Peptides

The amino acid sequence Arg-Gly-Asp (RGD) is a basic recognition unit of adhesion proteins, which was first discovered in fibronectin and later in many different adhesion proteins (Pierschbacher and Ruoslahti 1984, Gardner and Hynes 1985, Ruoslahti 1996). Meanwhile many small RGD containing peptides have been demonstrated to bind specifically to integrin receptors. It could be shown, that artificial RGD sequences which are constrained to a cyclic geometry or which are flanked by D-

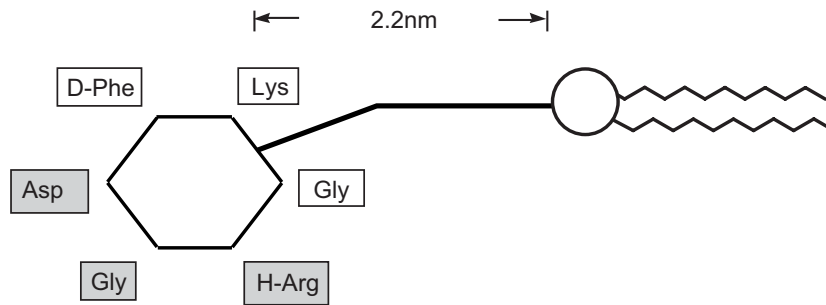


Figure 3.4: Schematic view of a cyclic RGD peptide coupled via a 2.2 nm spacer to a lipid.

amino acids, yield especially high binding affinities, which reach the affinity of natural ligands, cf. Fig 3.4 (Cheng et al. 1994, Kessler et al. 1996). These artificial RGD sequences are tested as therapeutic compounds. Either they act as agonists to promote the interactions of cells and tissues with implanted artificial materials like prostheses, or they act as antagonists to impede cell-cell and cell-ECM interactions. Diseases targeted by the RGD antagonist are highly diverse and include cardiovascular diseases, cancer, osteoporosis, and inflammations (Craig et al. 1995).

3.1.3 Outline

In the following chapter the design of a biomimetic substrate will be described. To this end integrin $\alpha_{IIb}\beta_3$ are isolated from blood platelets and reconstituted into lipid vesicles. These proteoliposomes are spread onto solid surfaces covered by films of cellulose (Wegner 1992). The cellulose is shown to be a suitable support enabling the lateral mobility of large receptors. We will study the mobility of receptors and surrounding lipids in detail to gain insights into the structural properties of the designed biomimetic substrates. In contrast, spreading of proteoliposomes on bare glass substrates impedes the formation of homogeneous lipid bilayers and the receptors are found to be immobile. To confirm the binding ability of the incorporated integrin receptors, a binding test of fluorescently labelled RGD peptides is reported in the last paragraph of this chapter.

3.2 Theory of Diffusion

The ability of different components of cellular membranes to diffuse laterally in the plane of the membrane is described in the fluid mosaic model. This intriguing property has been studied in different theoretical models, namely the *hydrodynamic model*, the *free volume theory*, *lattice (Monte Carlo) studies* and *continuum theories*, reviewed by Scalettar and Abney (1991), and Almeida and Vaz (1995).

Taking these theories together a realistic picture for the diffusion of large proteins in a lipid membrane can be obtained. For low protein concentrations the motion is dictated by the interaction of each protein with the lipid molecules. For large proteins this interaction is satisfactorily described by the diffusion constant D_T of the early hydrodynamic model of Saffman and Delbrück. However, small proteins (molecular mass ≈ 5 kD) behave differently and are better described by the free volume model (Galla et al. 1978). For higher protein concentrations or longer observation times the diffusing protein encounters other proteins. The interactions between the proteins result in a reduction of the initial diffusion constant D_T . The reduction increases with an increasing protein concentration, which is modelled by the three latter and more complex theories. However, viscosity changes in the membrane due to protein crowding as well as interactions between proteins are not considered in any of these models, since the effects are poorly understood so far.

For the model system of solid supported membranes discussed in this work, the diffusion of lipids and proteins is completely different than the diffusion in a free membrane. Here, frictional coupling to the substrate reduces the mobility of lipids and proteins by orders of magnitude. Therefore, effects of intra-protein interaction as addressed by the more complex theories can be neglected for supported membranes and the discussion will be restricted to the hydrodynamic model and to changes of diffusivity through frictional coupling.

3.2.1 The Hydrodynamic Model

In the hydrodynamic model the friction coefficient f is derived from the time independent Navier Stokes equation for creeping flow (low Reynolds number) of an incompressible fluid,

$$\frac{\delta \vec{v}}{\delta t} + (\vec{v} \cdot \nabla) \vec{v} = -\frac{1}{\rho} \text{grad } p + \mu \Delta \vec{v}, \quad (3.1)$$

where \vec{v} is the velocity field of the fluid, ρ the density, μ the viscosity of the fluid and p the pressure within the fluid. In the work of Landau and Lifschitz (1970) and Saffman and Delbrück (1975) the membrane (m) is modelled as an infinite viscous fluid which separates a less viscous fluid (l). The proteins are represented as cylinders of height h_C and radius R_C perpendicular to the plane of the membrane (cf. Fig 3.5). Their translational and rotational motions in the sheet of the membrane are thermally driven (Brownian motion). The lateral diffusion coefficient D_T is given by the Einstein Relation, $D_T = \frac{k_B T}{f_T}$ with the drag coefficient f_T . A logarithmic dependence of the translational diffusion coefficient D_T on the particle radius R_C is found:

$$D_T = \frac{k_B T}{4\pi \mu_m h_m} \left(\log \frac{\mu_m h_m}{\mu_l R_C} - \gamma \right), \quad (3.2)$$

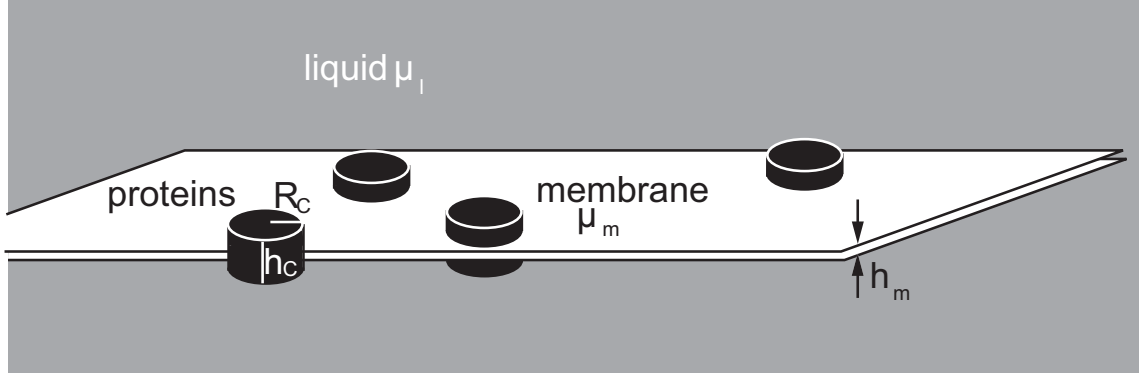


Figure 3.5: Hydrodynamic model of the membrane as infinite sheet and the proteins as cylinders with height h_C and radius R_C moving in the membrane by Brownian motion.

where μ_m is the three-dimensional viscosity, h_m the height of the membrane, μ_l is the viscosity of the outer liquid, and $\gamma = 0.5772$ the Euler constant. Due to the logarithmic dependence of the diffusion constant, large integral membrane proteins can diffuse nearly as fast as the much smaller lipid molecules. This theory is shown to adequately describe the lateral mobility of reconstituted proteins in free membranes (Peters and Cherry 1952, Poo and Cone 1974, Fahey and Webb 1978).

3.2.2 Diffusion in Supported Membranes

The diffusion of proteins and lipids in solid supported membranes is drastically reduced due to their frictional contact to the solid substrate. In the work of Evans and Sackmann (1988) the effects of a weak coupling of a membrane to an adjacent solid support are studied by modelling the slowing down of proteins by an interfacial drag b_s . Two frictional forces arise: first, a frictional shear stress f_m , produced by diffusants (proteins) in the membrane and the friction of the membrane with the substrate, and second a direct friction force f_p between the diffusants and the solid substrate. The diffusion constant is calculated to:

$$D_T = \frac{k_B T}{f_m + f_p},$$

$$f_m + f_p = 4\pi\eta_m \left[\frac{1}{4}\varepsilon^2 + \varepsilon \frac{K_1(\varepsilon)}{K_0(\varepsilon)} \right]. \quad (3.3)$$

Here, $\eta_m = \mu_m R_C$ is the two-dimensional viscosity of the free bilayer in an aqueous medium, K_0 and K_1 are modified Bessel functions of zero and first order. The argument ε is the dimensionless particle radius given by

$$\varepsilon = R_C \sqrt{\frac{\mu_l}{\eta_m h}} = R_C \sqrt{\frac{b_s}{\eta_m}}, \quad (3.4)$$

where h is the thickness of the coupling layer between the membrane and the substrate. Depending on ε two limiting cases can be discussed. For weak coupling $\varepsilon \ll 1$, the classical Saffman-Delbrück law holds (cf. Eqs. 3.2), whereas for $\varepsilon \gg 1$ one obtains

$$D_T = \frac{k_B T h}{\pi \eta R_C^2}. \quad (3.5)$$

In the latter case D_T depends on the size of the lipids and proteins diffusing and the thickness h of the lubricating layer between membrane and supporting substrate.

Since the frictional coupling b_s depends on properties such as the size of the diffusants, it provides a quantity which allows to compare different diffusants and different systems. The interfacial drag b_s can be extracted from the diffusion constant D_T by determining ε from Eqs. (3.3 – 3.5). The values of the two-dimensional viscosity η_m and η_l are: $\eta_m = 2.8 \times 10^{-10}$ Ns m⁻¹ for a DMPC bilayer at 27 °C (fluid phase) and $\eta_l = 1 \times 10^{-12}$ Ns m⁻¹ for the surrounding aqueous phase, the size of a diffusion DMPC molecule is assumed to be $R_C = 4$ Å (Pohl 1969, Gennis 1989, Merkel et al. 1989).

To give an idea of the size for the interfacial drag coefficient in bilayers we will summarize shortly some experimental results reported. For a free DMPC bilayer the frictional coupling to the liquid is calculated to $b_s = 6 \times 10^2$ Ns m⁻³. If the same lipid bilayer is supported by a glass substrate the drag coefficient reported is $b_s = 2.7 \times 10^6 \dots 1.5 \times 10^7$ Ns m⁻³ (Merkel et al. 1989). By supporting the DMPC bilayer by a soft and water uptaking polyacrylamide film the frictional coupling is reduced to $b_s = 7 \dots 8.5 \times 10^4$ Ns m⁻³ (Kühner et al. 1994). The decrease by two orders of magnitude in the absolute value of the interfacial drag demonstrates the power of biocompatible substrates: the supported membrane's fluidity approaches the value obtained for a free membrane.

Measurements of the coupling coefficient b_s for proteins are rarely reported. For a small protein (molecular mass 3.4 kD) which is coupled to a bilayer, the diffusion constant on a polyacrylamide film is measured (Kühner et al. 1994). The interfacial drag is determined to $b_s = 1.4 \times 10^8$ Ns m⁻³ and $b_s = 3.8 \times 10^5$ Ns m⁻³ for the protein in the proximal and the distal leaflet, respectively. A comparison with the interfacial drag measured for lipids reveals the strong influence of the diffusant's size on the diffusion constant and thus the interfacial drag. In contrast, the size dependence of proteins in free membranes is less strong, since it is governed by a logarithmic law, cf. Eq. (3.2).

3.3 Materials and Methods

As discussed in the introduction, solid supported membranes with incorporated integrin proteins are used as biomimetic model systems. The artificial membranes are supported either on bare glass substrates or on hydrated cellulose films, as

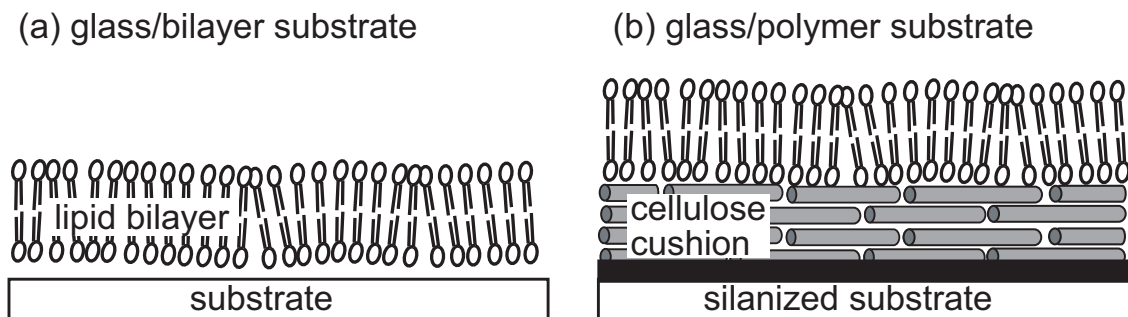


Figure 3.6: Schematic sketch of two different supported bilayers. In (a) the membrane is supported by a cleaned and hydrophilic glass substrate, whereas in (b) the membrane is deposited on a soft, hydrated film of cellulose molecules.

depicted in Fig. 3.6. Since the preparation of these systems is a multi-step process, it will be described stepwise in the following.

3.3.1 Glass Substrates

Glass substrates are cleaned as described previously, cf. section 2.3.2. The slides are dried and stored under vacuum for at least 12 h.

3.3.2 Silanization of the Glass Substrates

For the deposition of the polymer films the cleaned substrates have to be hydrophobic. Therefore they are immersed into a 5 vol% solution of octadecyltrimethoxysilane (ODTMS) in dry toluene, adding 0.5 vol% butylamine as catalyst (Mooney et al. 1996, Hillebrandt and Tanaka 2001)³. The samples are sonicated for 60 min at a controlled temperature of 13 °C, and soaked for another 30 min. To remove physisorbed ODTMS from the surface, the samples are carefully rinsed and sonicated for 2 min in dry toluene. The silanized substrate is hydrophobic, exhibiting a contact angle with water droplets between 90° and 100°.

3.3.3 Cellulose Films

The polymer cushions used as soft support for the membranes are ultrathin films of cellulose, which are converted from deposited trimethylsilyl cellulose (TMSC) molecules. The molecules have a hydrophilic cellulose backbone surrounded by flexible, hydrophobic side-chains (cf. Fig. 3.7). These hairy rod like molecules are synthesized as previously reported (Schaub et al. 1993). Due to the amphiphilic prop-

³(ODTMS, purchased from ABCR, Karlsruhe, Germany. Toluene absolute and n-butylamine are purchased from Sigma, Germany.)

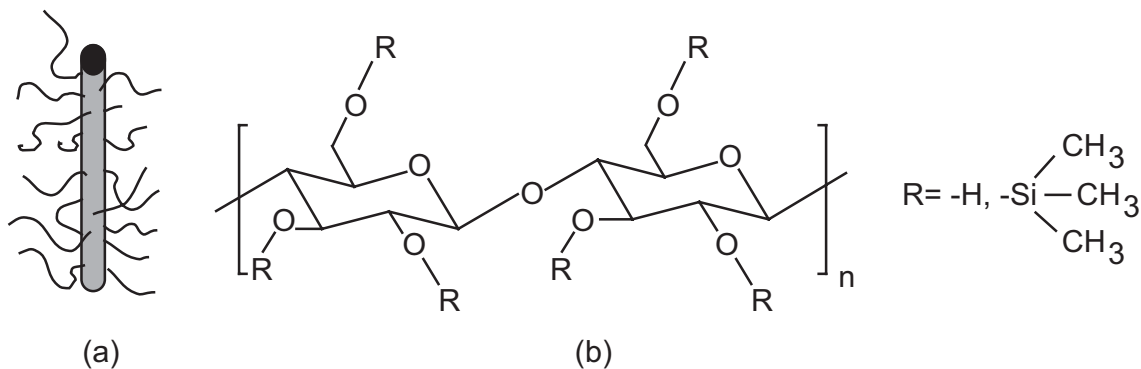


Figure 3.7: (a) Cartoon of a hairy rod molecule with the rigid cellulose backbone surrounded by flexible side-chains. (b) Chemical formula of a repeat unit of the cellulose backbone. The side-chains are represented by the rest-groups (R) in the graph.

erty of the TMSC molecules they can be deposited by the Langmuir Blodgett (LB) technique (Schaub et al. 1993). From a Langmuir trough 10 layers of TMSC are transferred onto the previously silanized glass substrates at a constant lateral pressure of 30 mN m^{-1} and a water subphase temperature of $17 \text{ }^\circ\text{C}$. Subsequently, the samples are dried in a vacuum chamber over night. In order to regenerate original cellulose by cleavage of silyl side groups the substrates are exposed to a saturated vapor of concentrated HCl for $15 \dots 30 \text{ s}$. The thickness of the dry regenerated film is approximately 5 nm , its swelling coefficient 2.2 under 86% relative humidity (Rehfeldt and Tanaka 2003).

3.3.4 Reconstitution of Integrins

Integrin $\alpha_{IIb}\beta_3$ is extracted from human blood platelets, by using Triton X-100 (Sigma-Aldrich, Germany), following the protocol of Fitzgerald et al. (1985). The functionality of the purified receptors is checked by enzyme-linked immunosorbent assay (ELISA) tests. The reconstitution of integrins into lipid bilayers is reported by Müller et al. (1993) and established in our laboratory by Hu (2001). Basically, the reconstitution of detergent solubilized proteins is a self-assembled process. In aqueous solutions the hydrophobic parts of lipids and proteins aggregate to minimize the contact between hydrophobic surfaces and water. DMPC and DMPG are mixed at equal molarities in chloroform (each 1 M) and the solvent is evaporated completely by storage in a vacuum chamber for some hours. Then, the lipids are resuspended in 1 ml of buffer A (cf. the Appendix) containing $0,5 \text{ mg}$ of integrin - solubilized by $0.01 \text{ mol}\%$ of Triton X-100. The Triton detergent is removed by Bio-Beads SM2 (Bio-Rad, Germany) and the proteosomes are separated from pure lipid vesicles and pure protein aggregates by centrifugation in a sucrose gradient. Finally, the vesicles

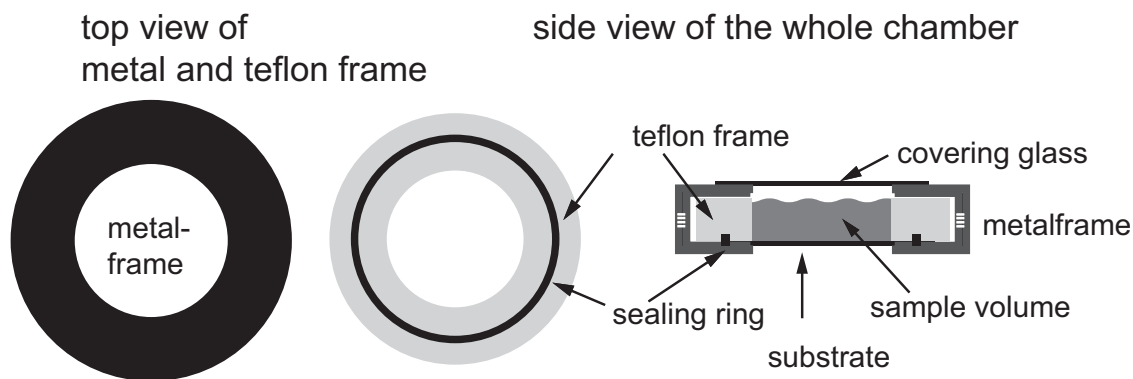


Figure 3.8: Sketch of the measuring chamber. The substrate forms the bottom of the chamber and the teflon frame plus the sealing-ring prevents the liquid to leak out. The surrounding metal frame squeezes the teflon frame to the substrate and assist its stability.

with the reconstituted integrins are dialyzed against buffer *A* to remove remaining sugar. The vesicles are shock frozen by using liquid nitrogen, and stored at $-70\text{ }^{\circ}\text{C}$.

For fluorescence experiments the integrins are labelled with 5(6)-TAMRA (Molecular Probes, Inc.) by slowly adding dyes to the integrins, which are detergent-solubilized in buffer *A*. The labelling efficiency is determined by UV absorption spectroscopy to be 1:1. These labelled proteins are mixed at a ratio of 1:10 with unlabelled ones.

3.3.5 Supported Planar Bilayers

Solid supported planar bilayers are formed by direct spreading of integrin-loaded vesicles onto bare glass slides or onto ultrathin cellulose films (Kalb et al. 1992, Müller et al. 1993, Sigl et al. 1997). The measuring chamber is assembled by a glass slide, which forms the bottom of the chamber and a teflon frame sealed by a rubber o-ring. The teflon frame is pressed against the substrate by means of two metal frames, which can be screwed tightly (cf. Fig. 3.8). The chamber is filled with $200\text{ }\mu\text{l}$ of vesicle suspension, which wets the whole substrate. To reduce the evaporation of the liquid, the chamber is covered by a glass slide and kept for 2.5 h at $37\text{ }^{\circ}\text{C}$. Then, by adding $125\text{ }\mu\text{l}$ of buffer *A1* the osmolarity of the solution is increased by 25 mOsm with respect to the intra-vesicular medium (cf. the Appendix). After another hour of incubation, the sample is rinsed carefully with buffer *A* to remove physisorbed vesicles.

In order to label the lipid moiety of the supported bilayer, NBD-PC (cf. the Appendix) is purchased from Molecular Probes, Inc., OR, and added to the chloroform solution of pure solubilized lipids at a concentration of 1 to 2 mol%.

3.3.6 Blocking Non-Specific Adhesion

To prevent non-specific adhesion of the giant vesicles to the bilayer, the substrate is incubated with a 3 wt.% solution of album bovine serum (BSA, Sigma, Germany) in buffer *B* for 1 h. After incubation the sample is rinsed carefully with buffer *B* to remove non-adsorbed material.

3.3.7 RGD Lipid

For this thesis a cyclic RGD-peptide (c[Arg-Gly-Asp-D-Phe-Lys(NBD)-Gly-]) is used. The synthesis is performed by D. Finsinger⁴ following the protocol by Gurrath et al. (1992). The coupling of the RGD sequence to DMPE (1,2-dimyristoyl-sn-glycero-3-phosphoethanolamine) is done by A. Escherich⁵ and reported elsewhere (Hu et al. 2000). The fluorescently labelled RGD peptide is synthesized by K. Behrendt⁶ as published in Goennenwein et al. (2003).

3.3.8 Fluorescence Microscopy

The homogeneity and the lateral distribution of labelled lipids and proteins are checked with an inverted microscope Axiovert 200 (Zeiss, Germany) which is equipped with a neofluar objective (antiflex, 63x, oil immersion, N.A. = 1.3) or an achroplan objective (40x, LD, N.A. = 0.75). The dyes in the membrane are excited with a high pressure mercury lamp combined with fluorescence filters that transmit at 510 . . . 560 nm for TAMRA and at 450 . . . 490 nm for NBD. Fluorescence emission is detected above 590 nm (TAMRA) or 515 nm (NBD) respectively with a cooled 12 bit CCD camera (Orca-ER, Hamamatsu, Japan). The data collection is carried out with the real-time imaging software *OpenBOX*.

3.3.9 Fluorescence Recovery After Photobleaching (FRAP)

The lateral mobility in the bilayer is measured by fluorescence recovery after photobleaching (FRAP) (Axelrod et al. 1976). FRAP relies on destroying all fluorescence dyes inside a small area (some 10 μm^2 size) by an intensive laser pulse. Then, the diffusion of new dyes into the bleached area is monitored by measuring the recovery of the fluorescence intensity with time. The fluorescence recovery is probed with the same laser as before, working now at a 1000 fold lower intensity, since it is important that a further bleaching of the area is negligible during the probing. The recovery is analyzed by a photomultiplier operated in the linear response regime⁷. In Fig. 3.9,

⁴Lehrstuhl für Organische Chemie 2, Prof. H. Kessler, Technische Universität München.

⁵Arbeitsgruppe für Bioorganische Chemie, Prof. L. Moroder, MPI für Biochemie, Martinsried.

⁶Arbeitsgruppe für Bioorganische Chemie, Prof. L. Moroder, MPI für Biochemie, Martinsried.

⁷The linear response is an important pre-requisite for the FRAP analysis and therefore measurements carried with CCD cameras should be considered with care, unless the linear regime is proofed for the whole sensitivity range.

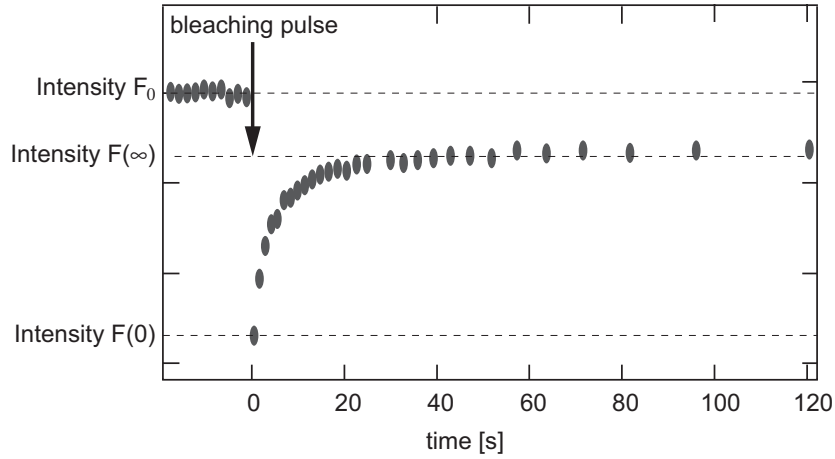


Figure 3.9: Typical fluorescence intensity recovery curve after a bleaching flash at $t = 0$ s.

a typical FRAP experiment is shown. The setup used for our experiments is an Ar^+ -Laser (Innova 70, Coherent, CA, USA) and the circular bleaching spot has a diameter of $9.3 \mu\text{m}$. The fluorescence signal is monitored by a RCA 31034-04 photomultiplier (Merkel et al. 1989, Kühner 1994). To eliminate effects of drift of the optical paths, the quality of the focus (in lateral and horizontal plane) is checked after each measurement with a camera.

The lateral diffusion constant D_T is obtained by analyzing the fluorescence recovery according to the theoretical model of Soumpasis (1983) which holds for a rectangular intensity profile of the bleaching light

$$D_T = \frac{r^2}{4\tau}. \quad (3.6)$$

Where r is the bleaching spot radius and τ the time constant which is obtained by fitting the experimental recovery curve to the analytical expression for the intensity:

$$F(t) = F(\infty) - [F_0 - F(0)](1 - \exp^{-\frac{2\tau}{t}}(I_0(\frac{2\tau}{t}) + I_1(\frac{2\tau}{t}))), \quad (3.7)$$

with F_0 the initial fluorescence intensity integrated over the bleaching area, $F(0)$ the intensity measured directly after the bleaching pulse, and $F(\infty)$ the intensity recovered at the end of the experiment (cf. Fig. 3.9). I_0 and I_1 are spherical Bessel functions of first and second order, respectively. Additionally, the fraction of mobile dyes in the sample can be determined from FRAP measurements. It is called the relative fluorescence recovery R and obtained by calculating the ratio of the final intensity $F(\infty)$ to the initial one F_0 :

$$R = \frac{F(\infty) - F(0)}{F_0 - F(0)}. \quad (3.8)$$

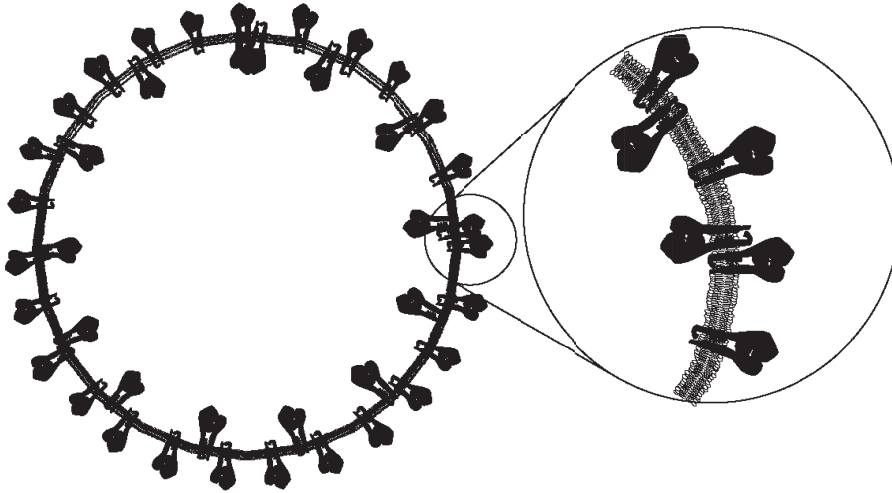


Figure 3.10: Cartoon of reconstituted $\alpha_{IIb}\beta_3$ proteins in a lipid vesicle. The drawing is to scale, assuming a vesicle size of 80 nm.

3.3.10 Cryo-Electron Microscopy

The electron microscopy measurements are done in cooperation with Friedrich Förster at the MPI für Biochemie, Martinsried (Abteilung für Molekulare Strukturbiologie, Prof. Baumeister). The sample - in our measurements proteoliposomes - is applied to a carbon coated copper grid (200 mesh, R2/2 Quantifoil Micro Tools GmbH, Jena, Germany), blotted and frozen via fluid ethane without any applied contrast method. Under liquid nitrogen condition, the sample is mounted and inserted into a Philips CM 120 Biofilter electron microscope (FEI Company, OR, U.S.). Images are visualized or projected onto a CCD camera. For a detailed description of the specific setup and further literature see PhD thesis of Böhm (2001).

3.4 Results

3.4.1 Reconstitution of $\alpha_{IIb}\beta_3$ Integrins into Lipid Bilayers

The reconstitution of integrins in lipid vesicles (cf. Fig. 3.10) is confirmed by cryo electron micrographs. In Fig. 3.11a, the reconstituted $\alpha_{IIb}\beta_3$ receptors are visible as small protrusions on both sides of the vesicle membrane. Closer inspection of many samples shows that these protrusions have a quite uniform size of about 20 nm, which is in good agreement with other studies (Erb et al. 1997, Weisel et al. 1992). The receptors are rather evenly distributed over the vesicle surface. Unfortunately, it was not possible to obtain tomography pictures of the integrin-loaded vesicles,

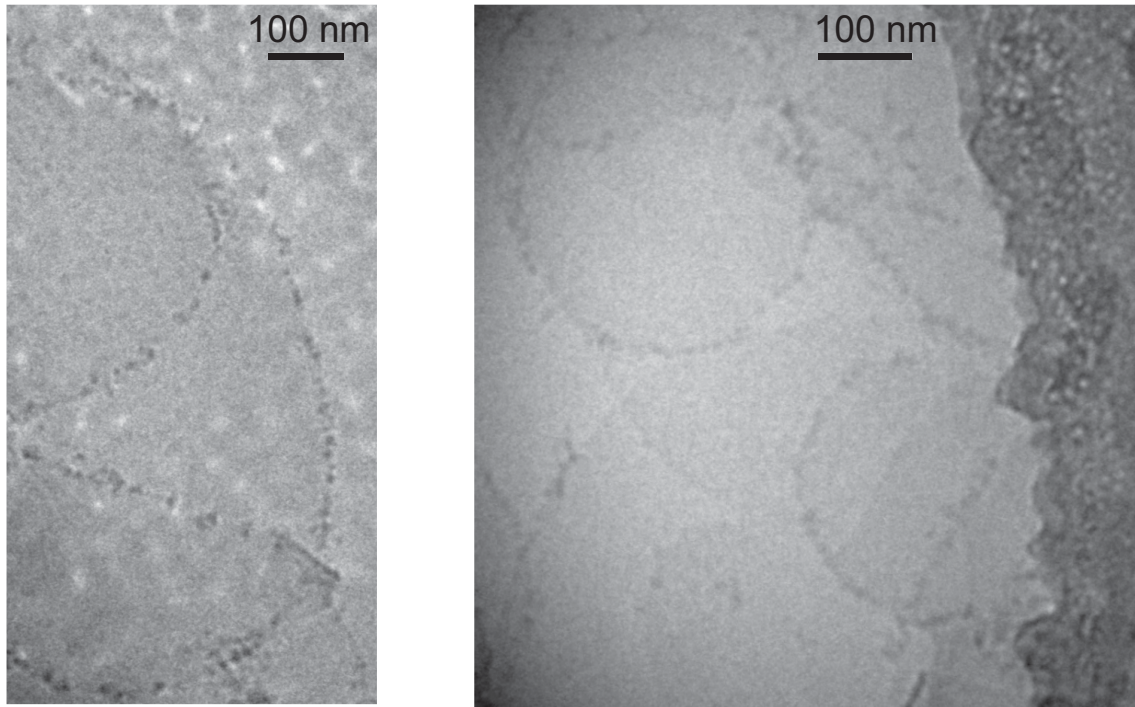


Figure 3.11: Cryo Electron Microscopy micrographs of reconstituted $\alpha_{IIb}\beta_3$ proteins in lipid vesicles. The tiny black protrusions in the vesicles membranes are integrins. Note that the density of the integrins in the membrane appears higher than it is, since the EM image is a projection of the three-dimensional image to the plane. Integrins which are in different heights are imaged in one plane and appear thus closer together. The large dark area in the image on the right hand side is a part of the sample supporting carbon film.

which allow for a three-dimensional reconstruction. With their help, a distinction between integrins sticking with their extracellular matrix inside or outside the vesicle might have been possible. In lack of detailed experimental results, a homogeneous distribution of the two orientations in the membrane is assumed in the following.

3.4.2 Determination of Integrin and Lipid Concentrations

It is important to characterize the concentration of proteins and lipids within the supported membrane. The measurement of the protein concentration and separately the lipid concentration can be accomplished in solution. Hereby, it is assumed that the ratio between lipids and proteins in the vesicle solution is the same as in the supported bilayer.

Quantitative Determination of the Integrin Concentration

Following the method reported by Bradford (1976), the concentration of proteins is determined with an adsorption technique. By binding a specific dye, here Coomassie Brilliant Blue G-250 (Sigma, Germany), to proteins the absorption maximum of the dye shifts from 465 to 595 nm. 20 μl of the sample volume is added to 980 μl of the protein reagent solution (0.01% (w/v) dye, 4.7% (w/v) ethanol and 8.5% (w/v) phosphoric acid). The absorbance is measured at 595 nm in an UV-spectroscope and compared to a control sample (pure buffer with protein reagent), yielding an absolute protein concentration of (60 ± 3) nM in the vesicle solution.

Quantitative Determination of the Phosphate Concentration

Since each phospholipid has one phosphate group, the molar content of phosphate in the sample can be determined and equated with the molar lipid content. The phosphate content of the proteins is negligibly small. The determination is done according to the method reported by Fiske and SubbaRow (1925) and Bartlett (1958). Ammonium-molybdate is reduced by phosphate and leads to an increase in the light absorption at 797 nm. The adsorption is linearly dependent on the amount of reduced ammonium-molybdate, which is proportional to the amount of phosphate present in the sample. The method is shown to be reliable for concentrations of phosphate from 0.02 μM to 1 mM. A detailed procedure is given in the Appendix. The phosphate concentration of the sample is determined to (402 ± 5) μM .

In summary, the sample exhibited an integrin concentration of (60 ± 3) nM and a lipid concentration of (402 ± 5) μM , resulting in a molar ratio of integrin:lipids of 1 : (6700 ± 300) . This protein content is rather high, although it is by a factor of 4.5 smaller than the highest concentration reported in literature - 1:1500 (Müller et al. 1993). The measured lipid to protein molar ratio corresponds to an average protein distance of (80 ± 2) nm in the membrane, if an area per lipid $A_L = 100 \text{ \AA}^2$ is assumed (Gennis 1989).

3.4.3 Formation of Planar Membranes with Integrins

Fig. 3.12 shows the fluorescence micrograph of a supported membrane with labelled integrins on bare glass substrate, in the following called *integrin/glass* membrane. The fluorescence distribution (and thus the protein distribution) is heterogeneous and numerous dark patches are visible, showing an incomplete coverage of the glass. These heterogeneous patches and defects can not be healed out, even after prolonged incubation of the vesicle suspension with the substrate. On bare quartz substrates a similar fluorescence image is obtained. These findings are in contrast to the homogeneous membrane reported by Erb et al. (1997), although the preparation procedures are very similar.

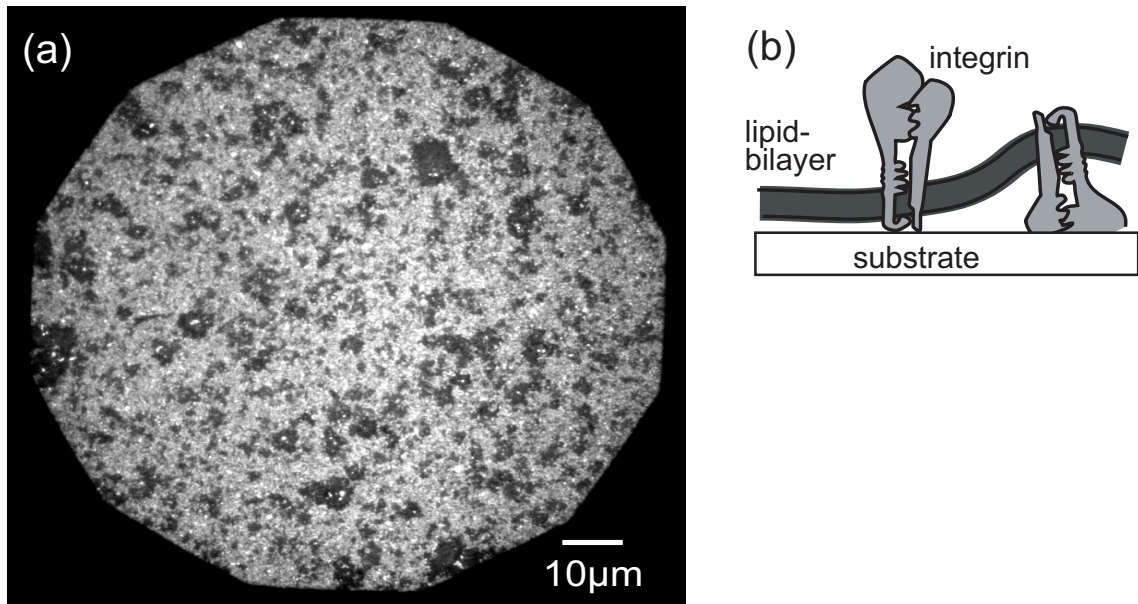


Figure 3.12: (a) Fluorescence micrograph of a membrane on a bare glass substrate. The integrins incorporated in the membrane are fluorescently labelled. (b) Schematic side view of the solid supported membrane.

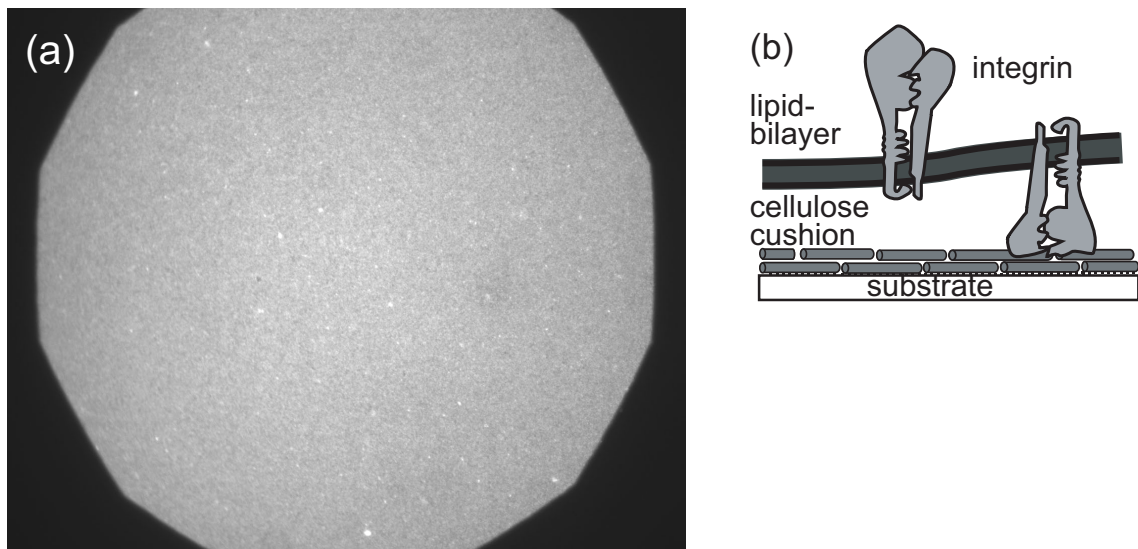


Figure 3.13: (a) Fluorescence micrograph of a cellulose supported membrane with remarkably high quality with respect to the image above. The integrins incorporated in the membrane are fluorescently labelled. (b) Schematic presentation of the membrane viewed from the side, showing the rod like cellulose molecules which support the membrane.

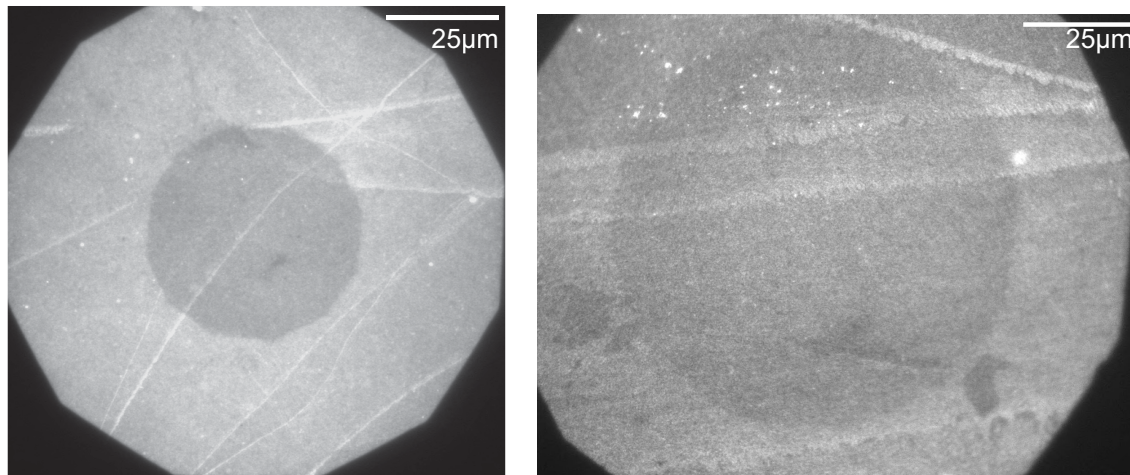


Figure 3.14: Fluorescence images of lipid bilayers on cellulose films containing labelled integrins. In both pictures some line-like defects exhibiting higher fluorescence intensity are observed. Additionally, a nearly circular darker area in the middle of the pictures can be seen. These are bleached areas from a previous observation of the bilayer with a diaphragm of that size.

In contrast as shown in Fig. 3.13, and as more clearly demonstrated by lateral diffusion measurements (cf. following section) a nearly perfectly homogeneous and fluid membrane is formed by membrane fusion on a cellulose "cushion", referred as *integrin/cellulose* membrane in the following. It should be noted that only in one out of three substrates the distribution of integrins is as homogeneous as shown in Fig. 3.13. In other experiments defects or even spotty films are obtained as demonstrated in Fig. 3.14. To assure identical experimental conditions in the following experiments, it is necessary to check the quality of each supported membrane by fluorescence microscopy. The appearance of defects in the fluorescent membrane seems to depend crucially on the quality of the underlying cellulose film: if the film is not hydrophilic (macroscopic contact angle $< 10^\circ$) or not homogeneous in its wetting properties, the supported membrane gets inhomogeneous.

3.4.4 Tunable Model System

For the application of supported membranes as model substrates, it is desirable to be able to vary parameters which have an impact on the adhesion energy like the lateral receptor density or diffusivity (Chazotte and Hackenbrock 1988). In our experimental system a receptor density variation can be achieved by adding small vesicles of pure DMPC/DMPG to the vesicle suspension before spreading onto the substrate. Miscibility of these two types of vesicle is checked by mixing (i) vesicles containing labelled integrin receptors and unlabelled pure lipid vesicles, as

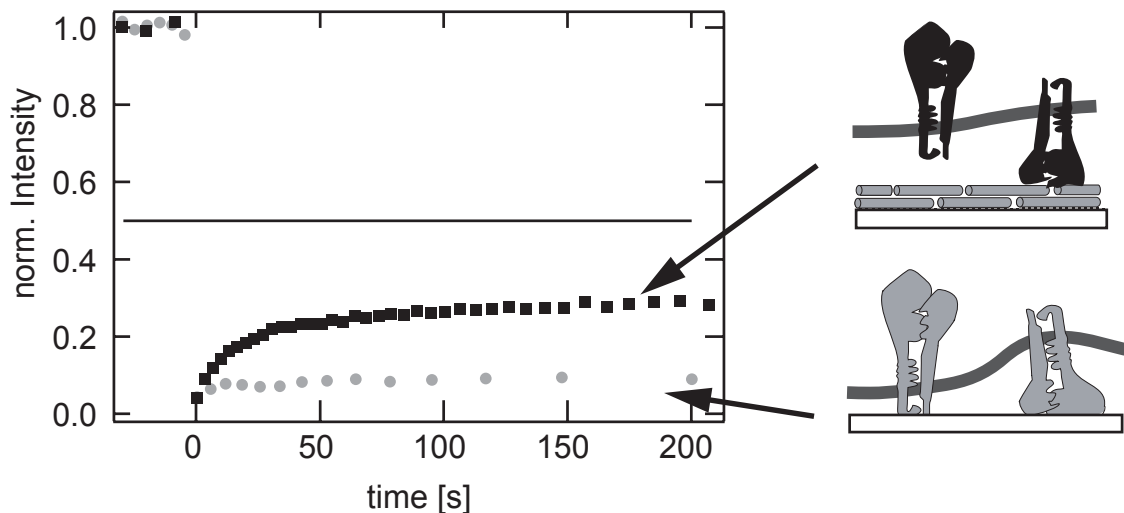


Figure 3.15: Fluorescence Recovery After Photobleaching Experiment (FRAP) on a bilayer with labelled integrin proteins. The gray circles correspond to an experiment on an integrin/glass substrate where no detectable recovery takes place, the black squares show the result for an experiment on an integrin/cellulose substrate, as schematically depicted in the sketches. For the integrin/cellulose bilayer a recovery of 25% is obtained.

well as (ii) unlabelled integrin vesicles and labelled vesicles. In both cases perfectly homogeneous supported membranes are observed. These two experiments provide strong evidence that both vesicle fractions are mixed during the incubation time and that the receptor density can be changed by the mixing procedure.

3.4.5 Determination of the Lateral Diffusion Constant D_T

FRAP experiments are carried out to determine the lateral diffusion constant D_T and the mobile fraction R of integrin receptors and lipids in supported membranes. For the integrin/glass membrane no fluorescence recovery can be observed (cf. gray data points in Fig. 3.15). In the case of the integrin/cellulose membrane, however, a recovery of the fluorescence signal of $(25 \pm 5)\%$ is obtained (black squares in Fig. 3.15). Analysis of the recovery curve yields a diffusion constant $D_T = (0.6 \pm 0.2) \mu\text{m}^2 \text{s}^{-1}$.

To understand the origin of the low recovery, two subsequent bleaching experiments at the same position of the sample are performed. The recovery curves of these FRAP experiments are shown in Fig. 3.16. All proteins are irreversibly bleached during the first laser pulse. Only mobile fluorescent proteins can diffuse into the bleached spot and contribute to the fluorescence signal in the second experiment. Thus, only mobile integrins are observed. Indeed, we obtain a much higher

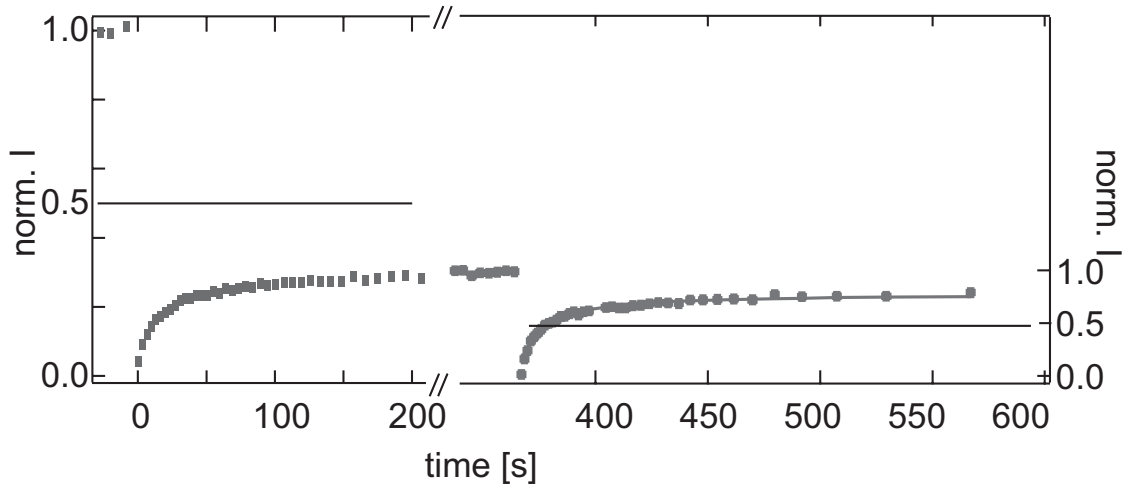


Figure 3.16: Two subsequent FRAP experiments of an integrin/cellulose bilayer at exactly the same position on the sample. In the first experiment the recovery is 30%. With reference to that level, the recovery in the second experiment is 90%. In the second experiment only mobile dyes are considered as explained in the text. This result suggests that mobile and immobile fractions of fluorescent integrins coexist within the sample.

recovery rate of $R = (86 \pm 5)\%$, while the diffusion constant D_T is the same as before. These findings strongly suggest that mobile and immobile integrin species coexist in the membrane. We assume that the immobile fraction corresponds to the receptors whose large headgroups point to the substrate and are immobilized by physisorption, whereas the mobile fractions correspond to those proteins with opposite transmembrane orientations. The immobile fraction of the proteins can be attributed to:

1. the local clustering of receptors within the supported membrane
2. nonspecific attraction between the proteins and the cellulose film
3. nonspecific binding to defects in the cellulose film.

The existence of defects in supported membranes is suggested by measurements of the lipid diffusion. For these experiments fluorescently labelled lipids (PC-NBD) are incorporated in the membrane. Unlabelled integrins are reconstituted into these bilayers. By spreading the vesicles onto cellulose films, homogeneous bilayers are obtained. In FRAP experiments a diffusion constant $D_T = (3.3 \pm 0.2) \mu\text{m}^2 \text{s}^{-1}$ and a recovery rate of 77% is determined (cf. Fig. 3.17a). Bleaching again the same spot, yields a mobile fraction of $(96.9 \pm 0.2)\%$ while the diffusion constant D remains the same (cf. Fig. 3.17b). As the mobile fraction R increases between the first and

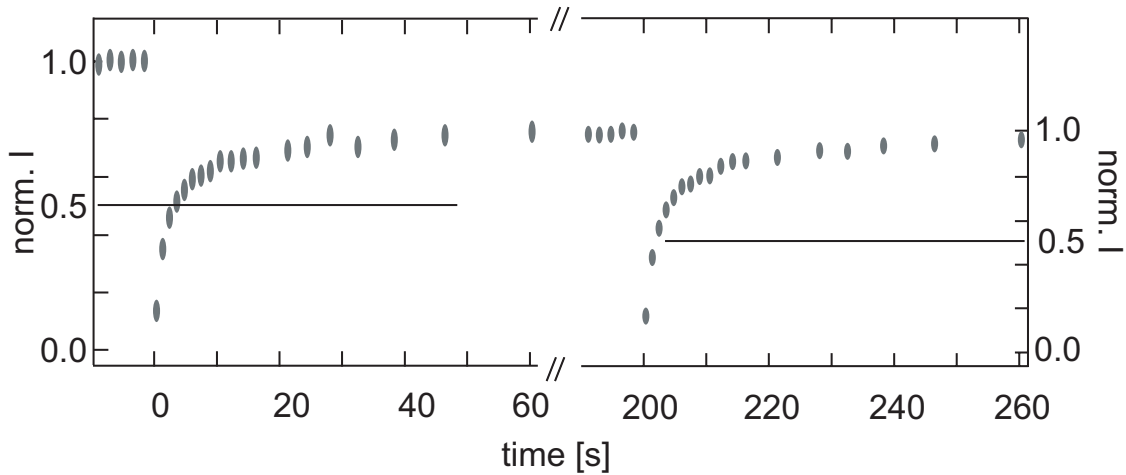


Figure 3.17: Two subsequent FRAP experiments of labelled lipids of an integrin/cellulose bilayer. The measurements are performed at exactly the same position on the sample. In the first experiment, the recovery is 77% and that fraction is taken as the reference fluorescence intensity F_0 for the second experiment. The recovery in the second experiment is 97%. This result suggests that there exists a large mobile fraction and a smaller immobile fraction ($\sim 20\%$) of fluorescent lipids in the sample.

second experiment, we can conclude - in analogy to the previous paragraph - that mobile and immobile lipids coexist. The existence of immobile lipids in the bilayer membrane is attributed to defects within the membrane. These defects (cf. 3 in the list above) are probably the reason for the low recovery R of receptors in the integrin/cellulose membrane experiments shown before.

The measured diffusion constants for lipids are a factor of 3 larger than those reported for pure lipid bilayers (without proteins) deposited onto cellulose cushions (Sigl et al. 1997). It is roughly the same as for membranes supported by non-crosslinked polyacrylamide gels (Kühner et al. 1994).

Interestingly, the diffusion constant of lipids in integrin-containing membranes supported by bare glass slides is a factor of 10 smaller than in polymer supported membranes. This might suggest that the integrins facing their large extracellular domain to the substrate hinder the diffusion of lipids enormously (Kucik et al. 1999). Alternatively, the diameter of the bleaching pulse ($9.3 \mu\text{m}$) might be larger than the size of most continuous lipid patches, therefore the measured long range diffusion coefficient is reduced.

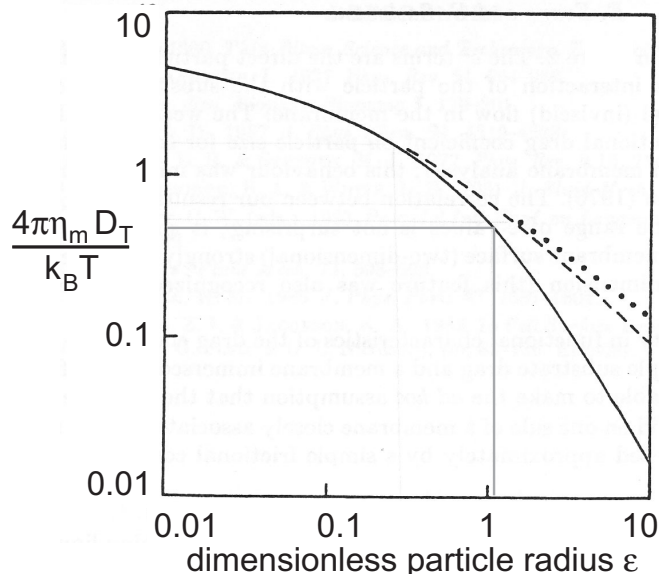


Figure 3.18: Dimensionless particle mobilities for translation of a disk-like particle in a membrane versus the dimensionless particle radius ϵ . The graph is taken from Evans and Sackmann (1988). The gray horizontal line indicates the calculated value $\frac{4\pi\eta_m D_T}{k_B T} = 0.51$ for our experiments, from which $\epsilon = (1.26 \pm 0.1)$ can be extracted (vertical gray line).

3.4.6 Determination of the Frictional Coupling

According to Evans and Sackmann (1988), the frictional coupling b_s of integrins to the cellulose covered substrate can be determined and compared with other experiments. The coupling is obtained as follows (cf. section 3.2.2): From the plot of the dimensionless function $\frac{4\pi\eta_m D_T}{k_B T}$ versus the dimensionless particle radius ϵ , a value of $\epsilon = (1.26 \pm 0.1)$ for the integrins is obtained (cf. Fig. 3.18). According to Eq. (3.4), the frictional coefficient is $b_s = 4 \times 10^6 \text{ N s m}^{-3}$ with $\eta_m = 2.8 \times 10^{-10} \text{ N s m}^{-1}$ and $R_C = 10 \text{ nm}$ for the integrins. The weaker the frictional coupling b_s to the substrate the freer the proteins can diffuse, and the more comparable is the model system of supported bilayers to the cell plasma membrane. Compared to the values in Table 3.1 the large, incorporated integrins have about the same coupling coefficient as small proteins attached to the distal layer and a two orders of magnitude smaller coefficient than proteins in the proximal layer supported by polyacrylamide gels. Compared to annexin V incorporated in membranes which are repelled from the solid by PEG coils, the larger integrins move twice as fast, whereas SNARE proteins incorporated in PEG tethered bilayers reach a comparable diffusion constant. Therefore, the cellulose film provides a well suited support for membranes to generate biomimetic surfaces.

For the integrin/glass system the diffusion constant is too small to be measured,

system	D_T ($\mu\text{m}^2 \text{s}^{-1}$)	b_s (Ns m^{-3})	Reference
antigen epitope 3.4 kD on crosslinked PA ⁸ gels linked -to the proximal layer	1...2	1.4×10^8	Kühner et al. (1994)
-to the distal layer	4...6	3.8×10^5	Kühner et al. (1994)
annexin V on PEG lipids	0.3		Wagner and Tamm (2000)
SNARE proteins	0.75		Wagner and Tamm (2001)

Table 3.1: Summary of diffusion coefficients and frictional coefficients of different lipid polymer composites and different proteins reported in literature.

and the dimensionless particle radius becomes very large as well as the frictional coupling, corresponding to almost immobile proteins.

Another quantity which can be extracted according to Evans and Sackmann (1988) is the height of the diffusing integrins over the substrate, if the frictional coupling b_s and the viscosity of the medium μ_l can be estimated. According to Eq. (3.4), the height is given by:

$$h = \frac{\mu_l}{b_s}. \quad (3.9)$$

For the viscosity in the system μ_l the viscosity of water can be assumed, since the main part of the proteins with their extracellular domain pointing to the substrate are exposed to the aqueous medium. With $\mu_l = \mu_{\text{water}} = 1 \times 10^{-3} \text{ Ns m}^{-2}$ (Pohl 1969), we calculate the height for the membrane $h = 3 \text{ \AA}$. This height is at least one order of magnitude too small, since the minimum height for mobile integrins should be of the order of their size, which is about 1 to 2 nm for the intracellular domain of the integrins. However, any increase in viscosity due to the interactions of the integrins with the membrane or the underlying polymer film will yield a larger distance of the integrin from the substrate. Taking $\mu_{\text{membrane}} = \mu_m = 0.7 \text{ Ns m}^{-2}$ or the viscosity of the underlying polymer film $\mu_{\text{polymer}} = 0.05 \text{ Ns m}^{-2}$ (Kühner et al. 1994) as an estimate for μ_l , one obtains $h = 170 \text{ nm}$ or $h = 10 \text{ nm}$, respectively. Thus, in the real system μ probably lies between the values μ_{water} and μ_m , yielding a realistic height of some 10 nm above the substrate (Lee et al. 1993).

From the diffusion constant of the lipids in the membrane, the frictional coefficient $b_s = 7 \times 10^6 \text{ Ns m}^{-3}$ of the lipids can be determined (with the radius $R_C = 4 \text{ \AA}$ for DMPC). To this end, the dimensionless particle radius $\varepsilon = 0.19$ is analyzed from Fig. 3.18, indicating that the coupling of the lipids to the substrate is weak since $\varepsilon = 0.19 \ll 1$. For the height of the diffusing membrane, $h = 7 \text{ nm}$ is found according to Eq. (3.9), with $\mu_{\text{polymer}} = 0.05 \text{ Ns m}^{-2}$. The height of some nm seems to be a reasonable upper limit. Since the assumption that the membrane diffusion is limited

⁸polyacrylamide

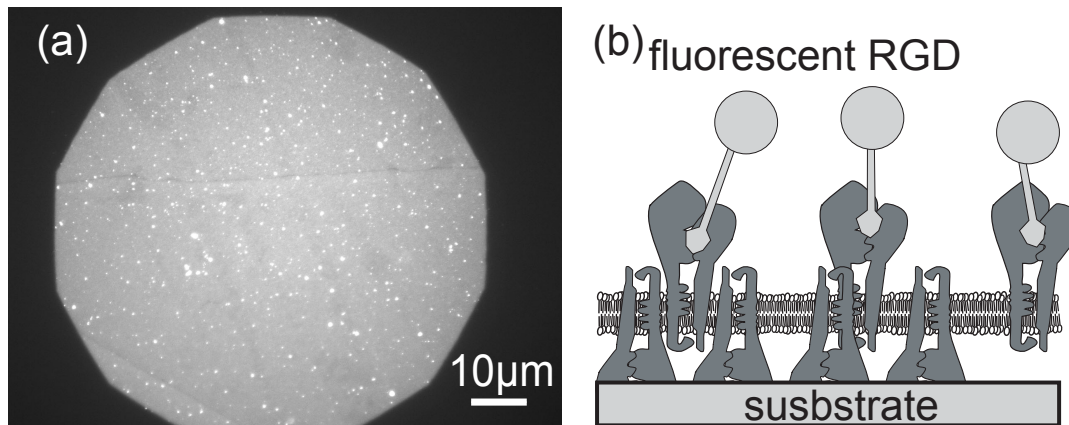


Figure 3.19: (a) Fluorescence micrograph of fluorescently labelled RGD-peptides bound to integrins $\alpha_{IIb}\beta_3$ which are embedded into a supported membrane on a cellulose cushion. (b) Schematic presentation of the side view of the membrane, where synthetic ligands bind only to the integrins pointing their extracellular headgroup to the aqueous phase.

by the frictional coupling to the polymeric support is too simple, additional contributions of the intra-membrane coupling and of the coupling to immobile proteins (so-called boundary lipid) will decrease the roughly estimated height.

3.4.7 Functionality of the Integrins

The functionality of the reconstituted receptors is evaluated from the specific binding to a cyclic hexapeptide containing the RGD sequence, which can be specifically recognized by the integrin $\alpha_{IIb}\beta_3$ receptor (Kantlehner et al. 1999, Hu et al. 2000). With a fluorescent labelled RGD peptide a simple binding test is performed: A bilayer with integrin and a pure DMPC bilayer are blocked against nonspecific adhesion by incubation with a solution of BSA (3 wt.%) in buffer *A* for 1 h. Then, the samples are rinsed with buffer *A* to remove non adsorbed material, and subsequently they are incubated for one hour with the fluorescent labelled peptide. After another careful rinsing, both sample are observed in the fluorescence microscope: The fluorescence intensity in the presence of integrin receptors (Fig. 3.19) is by a factor of two higher than that from the pure membrane. Another clear difference between the two samples appears when the dyes are continuously illuminated in the microscope. For the membrane with integrins, a continuous bleaching of fluorescent dyes, manifested by an exponential decay of the signal intensity is observed (black line in Fig. 3.20). In contrast, for pure membranes fluorescence signals from labelled RGD peptides remain constant (gray line in Fig. 3.20), indicating that in this case the fluorescence signal emerges from RGD peptides in the bulk solution.

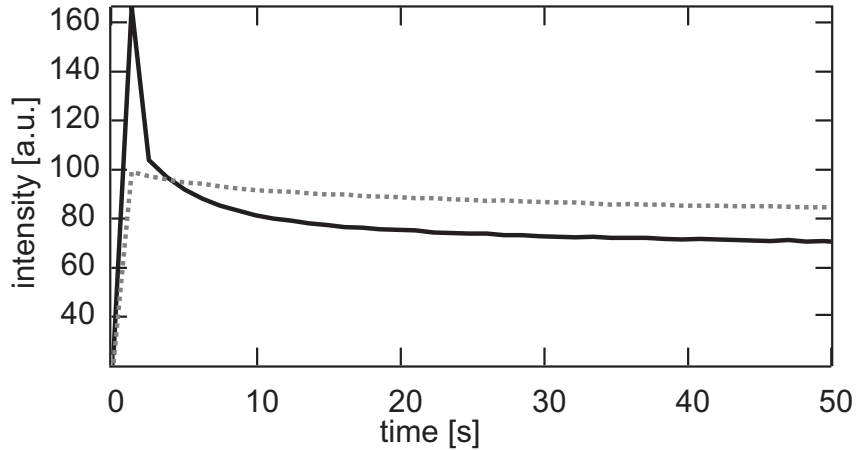


Figure 3.20: (a) Fluorescence intensity over time of a square region (10×10 pixel) of a continuously illuminated sample. The black line is the decay of fluorescence of the RGD-peptides bound to integrins incorporated into a supported membrane on a cellulose cushion. The gray line is the fluorescence signal from the same RGD-peptides incubated on a pure lipid bilayer without any integrins.

3.5 Conclusions

In this chapter it is demonstrated that homogeneous membranes with incorporated integrin proteins can be deposited onto thin layers of cellulose. The structural properties of a bilayer are maintained over dimensions of $18 \times 18 \text{ mm}^2$ as confirmed by fluorescence microscopy. In contrast, bilayers containing integrin proteins did not form homogeneous membranes on pure glass substrates. Dynamical and thermodynamical properties of the bilayers are checked by FRAP measurements. This revealed that a fraction 25% of the integrin receptors on the cellulose cushions exhibited long range lateral mobility with a diffusion constant $D_T = 0.6 \mu\text{m}^2 \text{ s}^{-1}$. The mobile fraction of the integrins is attributed to proteins pointing their large headgroups upwards into the aqueous phase, whereas the immobile integrins are expected to be physisorbed to the cellulose film. FRAP experiments with labelled lipids instead of labelled integrins reveal that the bilayers on the polymer films still exhibit a considerable number of defects, which can not be resolved optically. These defects are most likely responsible for the low recovery fraction R of the integrin receptors. In contrast to these mobile receptors, FRAP experiments on the integrin/glass bilayers show that integrins in membranes supported on bare glass substrates do not show any mobility. Even the mobility of lipids is drastically reduced in the integrin/glass bilayer.

Calculating the frictional coupling of the receptors in the integrin/cellulose membranes, demonstrates that the coupling strength of proteins to the substrate is in an

intermediate regime, whereas the coupling of lipid molecules to the support is weak and therefore quite similar to a free membrane. All properties of the model system integrin/cellulose membrane studied are found to be comparable to the properties of a cell plasma membrane, demonstrating that the artificial model system mimics cell plasma membranes very well. In particular, it can be concluded that the cellulose multi-layers are an essential building block for the design of a biomimetic membranes. Membranes supported on bare glass are not fluid. Moreover, on the soft polymer supports the functionality of the receptors is maintained, as demonstrated by a simple binding test.

A comparison with other supported membranes reported previously, demonstrates that the properties of the designed system are at least as powerful as the properties of other lipid composite systems. A disadvantage of the cellulose film are the multiple LB transfers. Not only the time consuming procedure, but also the low success rate limits the experiments seriously. However, depositing the films by multiple spin-coating steps would reduce the preparation drastically. Preliminary experiments yield quite promising layers (F. Rehfeldt, personal communication).

Relying on these well characterized biomimetic substrates, fundamental aspects of cell adhesion can be investigated in the next chapter.

Chapter 4

Cell Adhesion Studied in Model Systems

4.1 Introduction

Cell adhesion is a fascinating and complex interfacial process. It plays a key role in many aspects of living organisms, e.g. in the immune response or during the embryological development (Lodish et al. 2000). The adhesion process is controlled by a subtle interplay of different forces (Dustin 1997, Sackmann and Bruinsma 2002). There are specific forces, which work according to the lock-and-key principle enabling adhesion between a receptor and its conjugate ligand. The lock-and-key mechanism is responsible for the specificity of cell adhesion. In contrast, the generic forces involved in the adhesion process are unspecific. Steric repulsions are mainly generated by a dense polymer coat, which is covering the cell membrane. The repulsive polymer layer is called the cell glycocalix and prevents unspecific adhesion of cells. However, the glycocalix needs to be expelled of regions where tight contact between cells is formed. This adhesion plaque formation can be observed for example during the adhesion of fibroblasts to cell tissues and solid substrates. During the adhesion process additionally a drastic reorganization of the membrane coupled cytoskeleton of the adhering cell takes place. The short description of cell adhesion already demonstrates that there are many different processes acting in parallel. To get insights into cell adhesion, detailed experimental and theoretical studies are necessary.

There are mainly two different experimental approaches to study the cell adhesion:

- studies on real cells
- studies on cell models.

Cell models are artificial systems, which mimic key properties of cells and have no active regulation mechanism. Comparison between cell studies and cell model

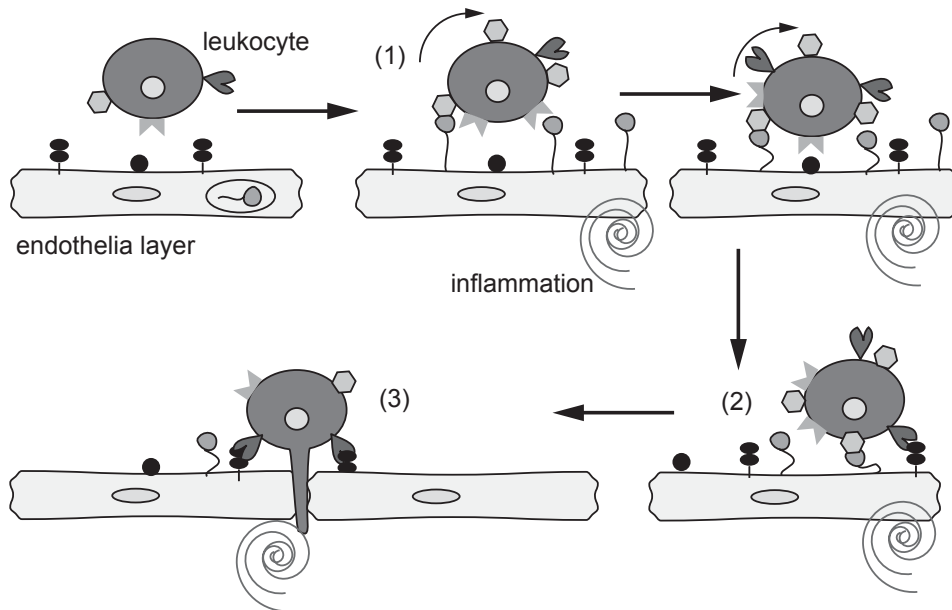


Figure 4.1: Leukocyte cascade triggered by the inflammation of the underlying tissue. In a first step the leukocyte rolls along the blood vessel wall due to transient specific bindings. In (2) it adheres strongly and in a third step (3) it moves through the endothelia cells (extravasation).

studies gives insights whether the studied process needs an active regulation or whether it is self-assembled. Model systems are often more variable, as it is simpler to change the attached ligand than to work with different cells. Additionally, the results of model systems are more reproducible as one can achieve the same experimental conditions over months, whereas cells may change during a day. However, studies on model systems demand a strong biochemic support, as the preparation of functional receptors is very difficult and lengthy.

4.2 State of Knowledge

Studies on Cells

Studies on cells often concentrate on the identification of the macromolecules involved and their biochemical regulations. Therefore an immense number of different receptor-ligand pairs have been discovered (Alberts et al. 1994). Insights in the physical principles governing the cell adhesion process have been gained by systematic studies of the migration of leukocytes, cf. Fig. 4.1 (Spinger 1994, Lodish et al. 2000). When an injury or inflammation occurs in a human body, specific binding proteins (selectins) are activated in the approximate endothelia layers, which cover the inner wall of blood vessels. Leukocytes passing by in the bloodstream are slowed down due to a successive formation and breakage of bonds mediated between the selectins and

receptors on the leukocyte surface. The continuous binding and rebinding of many receptor-ligand pairs in addition to the acting blood flow leads to a rolling of the leukocytes along the blood vessel wall. By activation of stronger adhesion molecules, namely integrin molecules, the leukocytes adhere tightly. Subsequently, the leukocytes move between adjacent endothelia cells to the underlying injured tissues. Chan et al. (1991) found that adhesion between cells is controlled by the formation of receptor clusters (often called junctions or immunological synapses (Dustin 1997)). Additionally it is reported that a reorganization of the actin-based cytoskeleton in the cell (e.g. the formation of focal complexes) appears upon adhesion. Further, the adhesion is limited by diffusion of receptors and repellers, since the latter have to be pushed away, before tight cell-cell contacts can be formed (Bongrand 1999, Zamir et al. 2000, Brochard-Wyart and de Gennes 2002).

Studies on Cell Models

In experiments with cell models, the test cells can be mimicked by giant vesicles. Receptors are reconstituted into the vesicle membrane or receptor fragments are coupled to the lipid membrane, cf. Fig. 4.2. The generic long range repulsion of the glycocalix is modelled by phospholipids exhibiting polymeric headgroups of polyethylene-glycols. Adhesion studies of these test cells to real cells, other vesicles or solid substrates have been reported (Guttenberg 2000, Marchi-Artzner et al. 2001, Prechtel et al. 2002). In the following chapter we will focus on the adhesion of vesicles to solid substrates via lock-and-key forces, where vesicles contain ligands and substrates exhibit the conjugated receptors. There are different possibilities to attach receptors onto substrates:

1. By incubating the receptor solution with a cleaned solid substrate, the adhesion proteins physisorb onto the substrate. The receptors have different orientations on the surface and the functionality is partially maintained (Guttenberg et al. 2001).
2. Receptors can be incorporated or attached to solid supported bilayers, which are spread onto hydrophilic surfaces (Kloboucek et al. 1999).
3. Receptors can be attached to cell polymer tissues, which cover the inorganic solid substrate. The soft polymers provide a biocompatible surface for the adhesion proteins, therefore the receptors are expected to be highly functional.

Adhesion was found to be accompanied by lateral segregation of receptor-ligand pairs (Bruinsma et al. 2000, Sackmann and Bruinsma 2002) leading to the formation of adhesion plaques. This behavior is reminiscent of the development of focal contacts in a cell adhesion process. The formation of adhesion domains in the model systems can be controlled by changing the concentration of ligands or receptors.

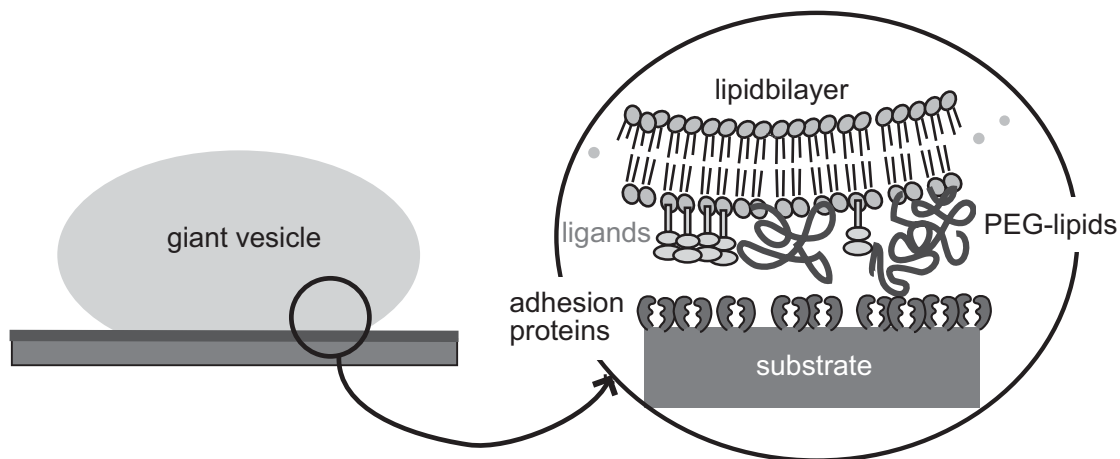


Figure 4.2: Model system of a giant lipid vesicle adhering to a solid substrate. The specific binding will be generated by the adhesion proteins and the conjugate ligands, whereas the PEG lipids prevent unspecific adhesion.

Surprisingly, low repeller concentrations (1 to 3 mol%) also strongly affects the adhesion strength. Naively, one would expect, that the repellers can be easily expelled from the contact area without any effect on the binding strength, since the contact area is only 2% of the total vesicle surface. However, due to an osmotic pressure difference arising from the depletion of the repellers in the contact area the thermodynamic potential of the specific adhesion energy between ligands and receptors is reduced (Guttenberg et al. 2001).

The model study presented in this thesis is a continuous development of the existing systems. Test cells are giant vesicles, which allow for the study of the interplay of specific and nonspecific forces as well as membrane bending elasticity in cell adhesion. As substrates, supported bilayers with incorporated integral adhesion proteins are used. These membranes are supported either on bare glass (called integrin/glass substrates in the following) or by cellulose films (integrin/cellulose substrates), as described in the previous chapter. The specific binding energy of giant vesicles to these two types of substrates is studied quantitatively by RICM (chapter 1). The central result is that the adhesion strength of the vesicles on the integrin/cellulose substrates is a factor of 30 higher than on the integrin/glass substrates. By estimating the number of formed bonds a determination of the interaction energies per single receptor-ligand is possible. For bioanalogue conditions (integrin/cellulose substrate) the adhesion strength is $10 k_B T$, in good agreement with estimates from literature. In contrast, for the bare glass/integrin substrates the specific adhesion is far below that value. These findings suggest that the receptors on bare glass substrates denature, demonstrating the crucial importance of bioanalogue substrates in cell adhesion investigations.

4.3 Theory of Vesicle Adhesion

In the following theoretical part the different contributions to the free adhesion energy of a vesicle will be discussed. Besides the generic forces discussed in chapter 2, the elasticity of membranes, the specific lock-and-key forces and the polymer induced repulsion have to be taken into account.

4.3.1 Bending Elastic Theory

The adhesion strength of vesicles in terms of the free energy of adhesion Δg_{ad} per unit area (also called spreading pressure) is determined by the equilibrium condition for soft shells.

In the following two different theoretical approaches, namely the Seifert and Lipowsky (1990) (SL) model and the Bruinsma (1995) (RB) model will be described, which both calculate the adhesion energy of vesicles. Both models are based on a rigorous analysis of the vesicle global shape in terms of fluid membranes. The boundary conditions are obtained from the required equilibrium of the bending moments close to the adhesion area. According to SL and RB, a determination of the local free adhesion energy from the deformation of the vesicle membrane at each point of the adhesion disc is possible.

In the SL model the attractive potential is a generalization of all the various forces experienced by the vesicle membrane such as electrostatic, van der Waals or hydration forces. This simplification is possible because the authors are interested in the gross features of a vesicle bound to a wall. By minimizing the free energy functional which accounts for the curvature energy, the bending rigidity and adhesion energy as well as constraints for the volume and the area of the vesicle, the SL model determines:

$$2\Delta g_{ad} = \frac{\kappa}{R_C^2}. \quad (4.1)$$

Here κ is the bending stiffness which is known for the vesicle (Gennis 1989). R_C is the contact curvature, characterized by the curvature at the transition from the adhering to the non-adhering region of the vesicle. The free adhesion energy Δg_{ad} can be determined by measuring R_C . Unfortunately, the contact curvature R_C is difficult to measure and one gets only order-of-magnitude estimates for the free adhesion energy Δg_{ad} (Rädler and Sackmann 1992).

Bruinsma (1995) suggests a simpler model for the adhesion of soft shells, which was shown to give more accurate results for RICM measurements than the SL model (Sackmann 1994). Consequently, the model will be discussed in more details here. A vesicle, which is assumed to be initially spherical, is deformed locally by the adhesion to a flat substrate and the adhesion domain is delimited by a circular contact line, cf. Fig. 4.3a,b. The contour of the vesicle along a direction x radial to the contact line is described by the following expression for the free energy (which is valid only

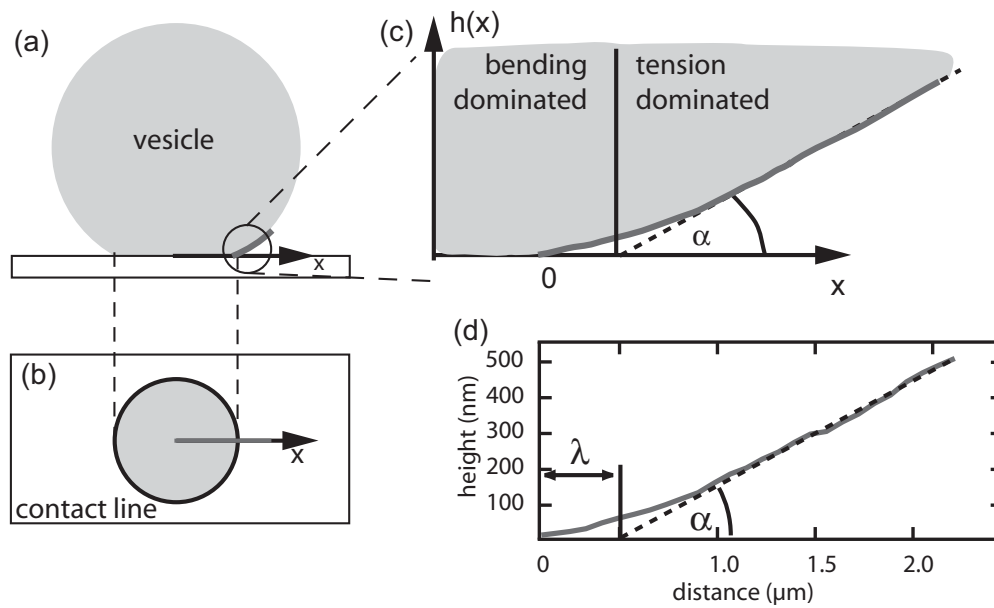


Figure 4.3: (a) Sketch of a sphere like vesicle adhering to a substrate, viewed from the side. (b) Seen from below a circular contact area of the vesicle with the substrate is formed. The black line indicates the contact line. (c) Enlarged side view of the contact area of the vesicle with the substrate, showing the bending and tension dominated domains of the vesicle. (d) The height profile of the vesicle reconstructed from the RICM interference micrograph. A straight line (dotted in the sketch) is fitted to the contour of the vesicle, yielding the contact angle α . The characteristic capillary length λ is given by the difference between intersection of the dotted line with the abscissa, and the point where the vesicle starts to bend off from the substrate.

for the area close to the adhesion domain):

$$\Delta F = \int_{\lambda}^{\infty} \left\{ \frac{\kappa}{2} \left(\frac{\partial^2 h}{\partial x^2} \right)^2 + \frac{\gamma}{2} \left(\frac{\partial h}{\partial x} \right)^2 \right\} dx - \int_{-\infty}^{\lambda} g_{ad}(x) dx, \quad (4.2)$$

where h is the height of the membrane and g_{ad} the adhesion energy and λ the capillary length of the membrane. The first term accounts for the bending energy, the second term for the tension energy and the third term for the free adhesion energy of the membrane. In comparison to the SL model, the constraints for the volume and area are neglected. By minimizing this energy functional, the following equation of the height profile along x is obtained:

$$\gamma \frac{\partial^2 h}{\partial x^2} - \kappa \frac{\partial^4 h}{\partial x^4} = 0. \quad (4.3)$$

The assumptions of the RB model leads to the following boundary conditions:

$$\begin{aligned} h(x) &= 0 & \text{for } x = 0 \\ h(x) &= \alpha x & \text{for } x \gg 0, \end{aligned} \quad (4.4)$$

where α is the macroscopic contact angle between the membrane and the substrate. The numerical solution for the differential equation (4.3) describes the membrane profile perpendicular to the contact line as shown in Fig. 4.4.

$$\begin{aligned} h(x) &= \alpha(x - \lambda) + \alpha \lambda \exp(-\frac{x}{\lambda}) & \text{for } x \geq 0, \\ h(x) &= 0 & \text{for } x = 0. \end{aligned} \quad (4.5)$$

λ is the capillary length, determined by

$$\lambda = \sqrt{\frac{\kappa}{\gamma}}, \quad (4.6)$$

according to Eq. (4.5) and Eq. (4.3). λ is a measure of the length over which the deformation of the membrane is determined by the bending stiffness of the membrane. For a liquid this length would be zero, since its bending stiffness is zero, whereas for an infinitely rigid bar λ would be the length of the bar. By fitting Eq. (4.5) to the reconstructed height, the values of λ and α can be deduced. However, since the height depends on both fitting parameters the determination of α and λ is not precisely possible. Much better results are obtained by fitting the two parameters separately. According to Eq. (4.4) α can be determined by fitting a straight line (tangent) to the vesicle shape for $x > \lambda$ (cf. Fig. 4.3c). The capillary length λ is the distance between $x = 0$ and the intersection of the x -axis with the tangent. The zero point of the x -axis ($x = 0$) is determined by the onset of the deflection of the membrane (cf. Fig. 4.3c). The bending stiffness κ is determined to $\kappa = 100 k_B T$ for DMPC vesicles containing 50 mol% cholesterol (Gennis 1989).

Even since all parameters are determined for the adhering membrane, the determination of the free adhesion energy Δg_{ad} according to Eq. (4.2) is non-trivial,

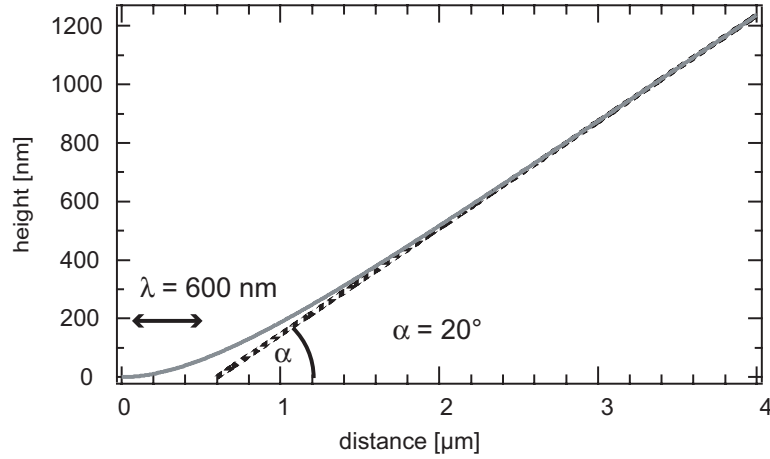


Figure 4.4: Calculated profile of a vesicle adhering to a substrate according to the RB model Eq. (4.5). The dotted line is the tangent fitted to the vesicle contour, defining the contact angle α and the characteristic capillary length λ .

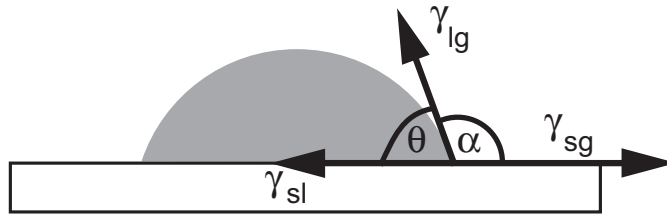


Figure 4.5: A droplet of a liquid on a substrate viewed from the side. The arrows indicate the direction of the forces acting on the contact line of the droplet. The interacting surface tensions are solid/gas (γ_{sg}), solid/liquid (γ_{sl}) and liquid/gas (γ_{lg}) the contact angle α is determined by the balance of these tensions.

since the second derivative of measured values are needed. In contrast, the adhesion energy can be measured more accurately from the theory of wetting. The spreading pressure - i.e. the free adhesion energy - can be calculated from the contact angle and the surface tension of the adhering (or equivalent wetting) soft shell:

$$\frac{\Delta G_{ad}}{A} = \Delta g_{ad} = -\gamma_{sl} + \gamma_{sg} + \gamma_{lg}. \quad (4.7)$$

ΔG_{ad} is the free adhesion energy, A the area of adhesion, Δg_{ad} the spreading pressure. γ_{sg} , γ_{sl} , γ_{lg} are the surface tensions between solid/gas, solid/liquid and liquid/gas, respectively.

According to the Young equation, the spreading pressure Δg_{ad} can be related to

the macroscopic contact angle θ , cf. Fig. 4.5 (deGennes 1985).

$$\gamma_{sg} = \gamma_{sl} + \gamma_{gt} \cos \theta. \quad (4.8)$$

For $\alpha = \pi - \theta$, Eq. (4.7) can be written as Young-Dupré law:

$$\Delta g_{ad} = \gamma(1 - \cos \alpha) \quad (4.9)$$

where $\gamma = \gamma_{lg}$ is the lateral membrane tension (corresponding to the surface tension of a liquid) (Israelachvili 1991). Accordingly the free energy of adhesion Δg_{ad} can be calculated from the geometric parameters λ and α , i.e. from the deformation of the spherical shapes, at every position of the contact line of the vesicle.

4.3.2 Lock-and-Key Forces

The adhesion energy of cells is determined by the specific binding energy w_{ad} between the receptor and its conjugated ligand as well as the number of bonds formed. Each specific lock-and-key bond relies on an interplay of 10 to 20 different single weak bonds (Bogan and Thorn 1998). The current types of weak bonds are:

- Hydrogen bonds ($E = 1 \dots 2 k_B T$): two electronegative atoms like oxygen and nitrogen can share a hydrogen atom and thus form a hydrogen bond. A prominent example is the hydrogen bond in water.
- Ionic bonds ($E = 2 \dots 4 k_B T$) are due to electrostatic interactions between complementary charged ions or domains of molecules. Due to the presence of salt in a physiological environment, the interaction is screened at distances larger than 2 nm (Debye length). However, the ionic bonds are responsible for a stable and tight shell of water molecules around free ions.
- Van der Waals interactions result from the attraction between transient or permanent dipoles. Dipoles are associated with polar and non-polar molecules by charge fluctuations within the molecules. The interaction is omnipresent but quite weak ($E = 0.2 \dots 0.5 k_B T$). Although, numerous van der Waals contacts due to precisely complementary shapes of the interacting macromolecules can attain an appreciable strength.
- Hydrophobic interactions occur between non-polar molecules in an aqueous environment. Enclosing hydrophobic molecules by water costs a lot of energy as the polar water molecules have to order around the hydrophobic molecules. If the hydrophobic molecules aggregate energy is decreased. This corresponds to an attractive force between them.

An interplay of these interactions is responsible for the lock-and-key forces between two conjugated molecules. Since the bonds are rather weak (average energy

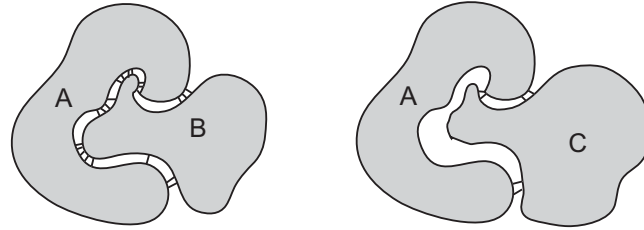


Figure 4.6: Sketch of a lock-and-key bond between two biomolecules A and B or A and C. The recognition is established by many weak bonds, depicted as black lines between the two biomolecules. Only if the two molecules fit well together like the molecule A and B, many weak bindings can form and the aggregate of A and B is strongly attached. For a small number of weak bonds (molecules A and C) the molecules dissociate rapidly due to thermal fluctuations.

of $0.25 \dots 2 \text{ kJ mol}^{-1} = 0.5 \dots 4 k_B T/\text{bond}$) many bonds have to work together to stabilize bound macromolecules against thermal unbinding. Exactly this weakness enables the high precision of recognition: only if the highly complex structured surfaces of interacting biomolecules are complementary in structural and chemical properties, enough weak bindings can form and lead to a strong attachment (cf. Fig. 4.6) (Bogan and Thorn 1998). "Wrong" binding partners dissociate immediately.

Additionally, the weak binding provides the ability of macromolecules to dissociate spontaneously and no further regulation is necessary to separate them. The importance of the unbinding has been mentioned in the example of the rolling leukocytes.

4.3.3 Repulsion by Repellers and Ligands

The measured free adhesion energy Δg_{ad} is a thermodynamic potential, which has been shown to depend not only sensitively on the number of bonds and their binding energy, but also on further thermodynamic variables like the ligand and repeller concentrations. Since the large repeller molecules would impede the tight binding, they are expected to be expelled from the adhesion domains. Therefore the concentration of repellers in the adhesion domain is reduced with respect to the free membrane. This generates an osmotic pressure difference and reduces the specific adhesion energy ΔW_{ad} to the measured free adhesion energy Δg_{ad} (Bruinsma et al. 2000, Guttenberg et al. 2001). For ligand molecules a similar effect might occur since their concentration in the contact area is influenced by the concentration of the receptors on the substrate. However, the osmotic pressure difference generated from the ligands is expected to be much smaller than that from the repellers and will be neglected in the following.

To calculate the repulsion due to the osmotic difference of the lipid anchored

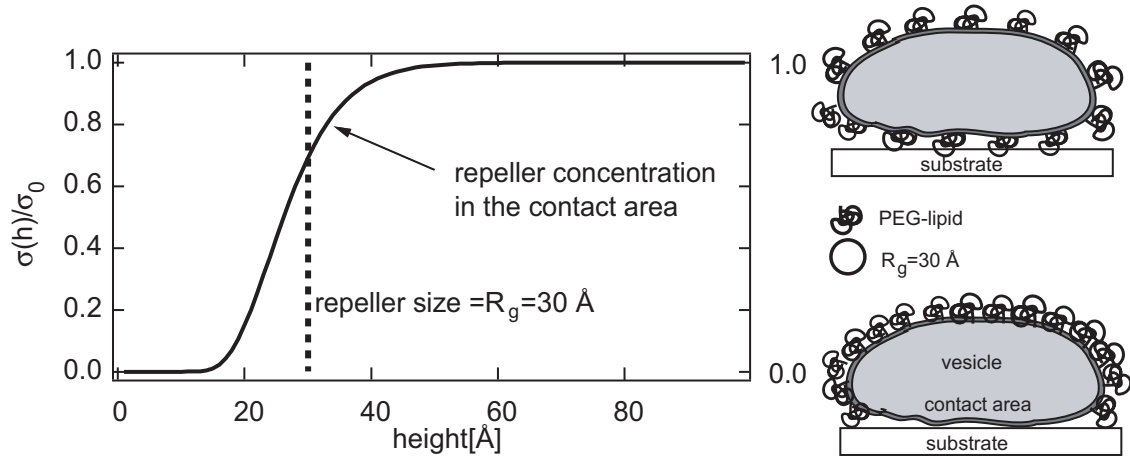


Figure 4.7: Calculated ratio of repellers present in the contact area as function of the membrane height (according to Eq. (4.11))

PEG lipids, one has to consider the sum of the translational entropy term and the cost of compression of the large polymers. In equilibrium, the local potential has to be equal to the chemical potential μ :

$$\mu = k_B T \ln[\Omega \sigma(h)] + \frac{\pi^2}{6} k_B T \left(\frac{R_g}{h} \right)^2 \exp \left[-1.5 \left(\frac{h}{R_g} \right)^2 \right], \quad (4.10)$$

where Ω is the area per repeller headgroup and σ the repeller surface concentration, h the height of the membrane and R_g the radius of gyration of the repellers. According to $\mu = k_B T \ln(\sigma_0 \Omega)$, where σ_0 is the repeller concentration far from the adhesion domain, the repeller concentration in the adhesion domain can be calculated to

$$\frac{\sigma(h)}{\sigma_0} = \exp \left[-\frac{\pi^2}{6} \left(\frac{R_g}{h} \right)^2 \exp \left[-1.5 \left(\frac{h}{R_g} \right)^2 \right] \right]. \quad (4.11)$$

Thus the repeller concentration in the adhesion plaque is seriously reduced if the spacing h is small compared to the radius of gyration R_g of the repeller as shown in Fig. 4.7. The Gibb's free energy per unit area can be calculated according to $\mu = \frac{\partial G}{\partial N}$, with N the number of particles or repellers, which is proportional to the concentration σ . From the concentration difference between the contact area and the free membrane, the inter-membrane potential energy $V_R(h) = G(\sigma(h)) - G(\sigma_0)$ is obtained, yielding two limiting cases:

$$\begin{aligned} V_R(h) &= k_B T \sigma_0 \frac{\pi^2}{6} \left(\frac{R_g}{h} \right)^2 \exp \left[-1.5 \left(\frac{h}{R_g} \right)^2 \right] & \text{for } h \gg R_g \\ V_R(h) &= k_B T \sigma_0 & \text{for } h \ll R_g. \end{aligned} \quad (4.12)$$

For strong adhesion ($h \ll R_g$), we find that the repulsive potential is equal to the two dimensional osmotic pressure as predicted by van't Hoff's law for a dilute solution

(Adam et al. 1995):

$$\pi_R = -\frac{k_B T}{V_M^0} \ln x_M, \quad (4.13)$$

where π_R is the osmotic pressure of the repellers, V_M^0 is the molar volume of the membrane and x_M the mole fraction of the membrane. For a small concentration c_R , Eq. (4.13) can be simplified by the approximation $\ln x_M = \ln(1 - c_R) \approx -c_R$:

$$\pi_R = c_R k_B T, \quad (4.14)$$

where c_R is the concentration of the repellers R . The pressure difference $\Delta\pi_R$ between the repeller free and repeller containing membrane domains is:

$$\Delta\pi_R = k_B T \Delta c_R. \quad (4.15)$$

The free energy of adhesion can be expressed:

$$\Delta g_{ad} = W_{ad} - \Delta\pi_R, \quad (4.16)$$

where W_{ad} is the specific adhesion energy per unit area of the receptor-ligand pairs. Hereby, effects of the membrane elasticity and of the osmotic pressure difference generated by ligands are neglected.

4.4 Materials and Methods

4.4.1 Giant Vesicles

The giant vesicles investigated are composed of equimolar amounts of DMPC and cholesterol, 1 mol% of DMPE (1,2-dimyristoyl-sn-glycero-3-phosphoethanolamine) with PEG head-groups (molar mass PEG = 2000) and 1 mol% of DMPE with a cyclic RGD peptide head-group (RGD lipid) with respect to the DMPC content. Giant vesicles are prepared by the electrosweeling technique (Dimitrov and Angelova 1988, Albertsdörfer et al. 1997), described in detail in the Appendix.

4.4.2 Adhesion Assay

The adhesion of giant vesicles to supported bilayers with incorporated integrins, which have been characterized in the previous chapter are studied. There, two different substrates are prepared:

- integrin/glass substrate: the integrin-containing vesicles are spread directly on glass substrates. This results in inhomogeneous bilayers where no diffusion of the receptors can be observed.

- integrin/cellulose substrate: the protein containing vesicles are spread on ultrathin cellulose films. Here, perfectly homogeneous bilayers appear as demonstrated by fluorescence microscopy. The integrin receptors have a diffusion constant of $0.6 \mu\text{m}^2 \text{s}^{-1}$.

A glass substrate forms the bottom of a measuring chamber (cf. Fig. 3.8), which is filled with buffer B . $200 \mu\text{l}$ of the giant vesicle suspension is injected carefully into the chamber. The vesicles settled to the bottom of the measuring chamber due to gravity as the intra vesicle sucrose solution has a higher density with respect to the outer buffer B ($\Delta\rho = 50 \text{ g cm}^{-3}$). Due to an osmotic pressure difference of 30 to 40 mOsm between the inner and outer medium of the vesicle, the vesicles are deflated. Thereby excess area is generated, enabling the formation of a finite contact area between the vesicles and the flat substrate. A tensed vesicle would behave like a sphere and only form a point-like contact with a plane.

4.5 Results and Discussion

To evaluate the binding capacity of the reconstituted receptors in the supported membranes, it is essential to compare data for well known vesicle compositions and for identical substrates. To this end, the homogeneity of the integrin-containing bilayer is checked in fluorescence microscopy before each adhesion experiment. The quality of the integrin is kept constant by shock freezing the integrin vesicles in amounts of $100 \mu\text{l}$ with liquid nitrogen directly after preparation. They are stored at $-70 \text{ }^\circ\text{C}$ and defrosted directly before use and completely used.

4.5.1 Control Experiments

In RICM micrographs strong adhesion is manifested by dark areas. These domains are attached to the substrate and do not exhibit thermally excited bending fluctuations. Weakly adhered domains, however, are strongly moving and flickering. The contact areas of the latter exhibited large bright patches assuming that their height is about 100 nm, cf. chapter 1. To determine the state of adhesion from one picture, it is helpful to average over single images for a period of more than 5 s. If the vesicle or areas of the vesicle are strongly adhered, the averaged image of the vesicle appears very clear. However, if the vesicle is weakly adhered and performs undulations, the averaged image of the vesicle appears blurry, as shown in Fig. 4.8c. Thus RICM enables one to distinguish between strong binding and weak binding domains of a vesicle.

Non-specific adhesion as origin of dark domains is excluded by the following control experiments:

1. A giant vesicle without RGD ligands is brought in contact with an integrin-containing supported membrane for more than 10 min. The vesicle does not show any dark adhesion plaques (cf. Fig. 4.8).

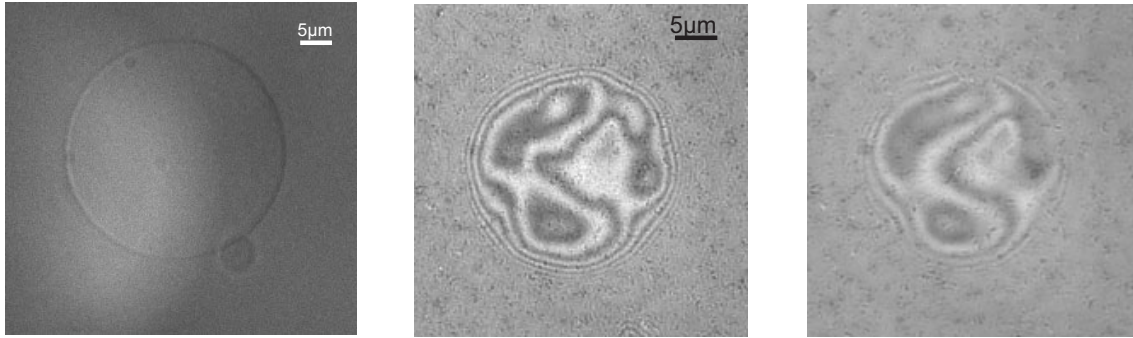


Figure 4.8: Micrograph of a giant vesicle without any RGD ligand in contact with an integrin-containing lipid bilayer. a) bright field picture of the vesicle b) RICM micrograph of the same vesicle (integration time 59 ms) c) averaged RICM interferogram obtained by integrating over 6 s.

2. A RGD-decorated giant vesicle in contact with a pure supported DMPC membrane does not show any dark adhesion domains.
3. An integrin-containing supported membrane is incubated for one hour with a specific antibody CD41A (Chemicon, Germany) against the intact platelet $\alpha_{IIb}\beta_3$ complex. Then the substrate is blocked by BSA and giant vesicles with RGD peptides are added to the measuring chamber. In the micrograph no dark adhesion domains are observed.

All these control experiments demonstrate that strong binding can only be mediated by specific bindings, i.e. accessible integrin receptors and conjugated RGD ligands.

4.5.2 Free Adhesion Energy Determination for Giant Vesicles

In the following the adhesion strength of vesicles adhering to the two different substrates, integrin/glass and integrin/cellulose is studied. The main differences between the two substrates are the mobility and the bioanalogue conditions of the receptors. The effect on adhesion will be elucidated by comparing the adhesion strengths of the two substrates. Additionally, a systematic study of the influence of the PEG concentration on the adhesion energy allows to determine the specific adhesion energy W_{ad} between the vesicle and the substrate. Since the approximate number of bonds in the adhesion area is known, the specific adhesion energy w_{ad} between a single integrin receptor and a RGD ligand can be determined.

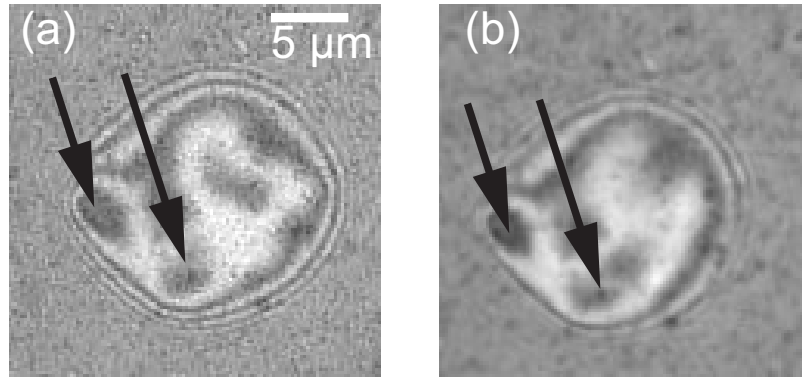


Figure 4.9: (a) RICM interferogram of a giant vesicle with 1% RGD lipid and 2% PEG lipid adhering to an integrin-doped membrane on a bare glass substrate (integration time 59 ms). The arrows indicate the areas of strong adhesion (dark), whereas the main part of the contact disc adheres only weakly (bright areas) and exhibits strong flickering. (b) RICM image of the same giant vesicle taken with a prolonged integration time of 5 s. Due to the motion of the contact area, the vesicle exhibits a bleary appearance. Only the attached areas exhibit a clear contact line.

Adhesion Energy on Integrin/Glass Substrates

2 mol% PEG Lipid in the Vesicle Membrane The adhesion of giant vesicles with 2 mol% PEG lipids and 1 mol% RGD lipids adhering on an integrin/glass substrate (integrin:lipid about 1:7000) is shown in the two RICM micrographs of Fig. 4.9.

Most of the adhesion disc exhibits large bright patches which correspond to weak adhesion. Additionally, the blurred appearance of the averaged image (Fig. 4.9b) demonstrates that the contact area fluctuates strongly. Fig. 4.10 shows the values measured for the contact angle. The tension γ is determined to $\gamma = (0.9 \pm 0.2) \times 10^{-6} \text{ J m}^{-2}$ by Eq. (4.6) with $\lambda = (670 \pm 80) \text{ nm}$. The local adhesion energies at the positions of the lines in the micrograph are calculated according to Eq. (4.9) and are shown in the lower graph of Fig. 4.10. The mean value for the adhesion energy Δg_{ad} for 2 mol% PEG on a integrin/glass substrate is determined to $\Delta g_{ad} = (5 \pm 3) \times 10^{-8} \text{ J m}^{-2}$. The accuracy of the measurement of the adhesion energy depends critically on the quality of the RICM-images. Here, for a mainly weakly adhering vesicle the contact angle can be measured quite accurately. However, mistakes in the capillary length λ are large, since it is difficult to determine the onset of the deflection. Therefore more accurate results are obtained by measuring the isotropic tension at sites where the onset of the deflection is well defined (position number 0 and 1 in Fig. 4.10), and using this value to determine the adhesion energies Δg_{ad} at the other positions.

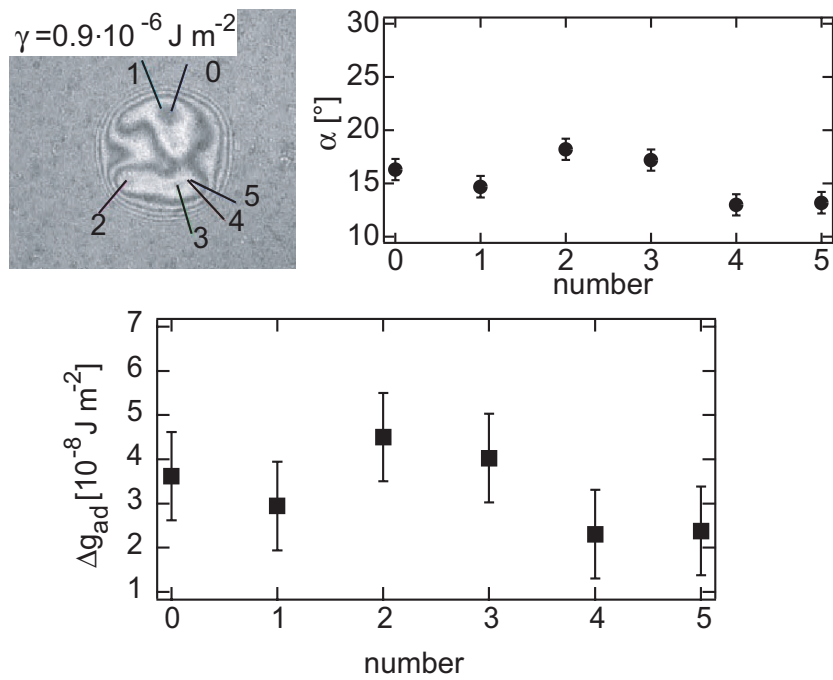


Figure 4.10: RICM micrograph of a giant vesicle (1% RGD lipid and 2% PEG lipid) adhering to an integrin/glass substrate. In the graphs the values for the membrane tension γ , the contact angles α (circles) and the free adhesion energies Δg_{ad} (squares) at the indicated sites near the rim of the contact area are shown.

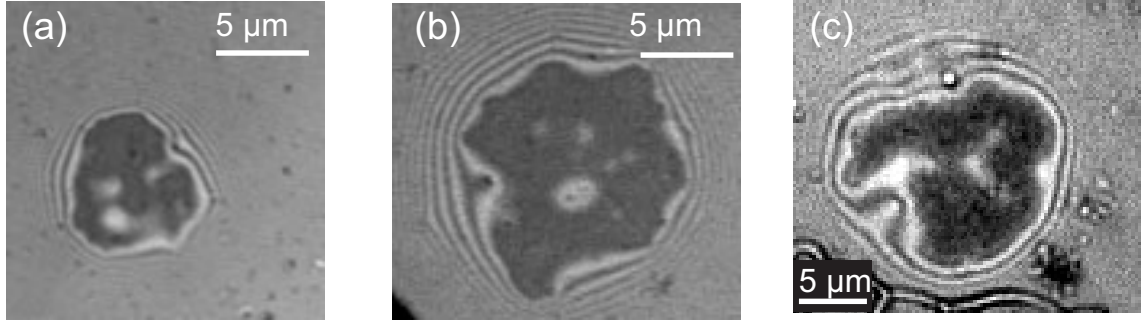


Figure 4.11: RICM micrographs of a giant vesicles (1% RGD lipid and 2% PEG lipid) adhering to a membrane with integrin $\alpha_{IIb}\beta_3$. The membrane is supported by a cellulose cushion. The dark areas indicate strongly adhered domains.

Adhesion Energy on Integrin/Cellulose Substrates

2 mol% PEG Lipid in the Vesicle Membrane Fig. 4.11 shows micrographs of the same vesicle composition as in the previous section, now adhering on integrin/cellulose substrates. A comparison of the micrographs of Fig. 4.11 with the figure in the previous paragraph (Fig. 4.9) demonstrates that the adhesion of the vesicles on the soft cellulose cushions is stronger, since the whole contact area appears dark and no flickering can be observed. The measurement of the free energy per unit area Δg_{ad} confirms the observation: $\Delta g_{ad} = (90 \pm 30) \times 10^{-8} \text{ J m}^{-2}$ and $\gamma = (1.2 \pm 0.5) \times 10^{-5} \text{ J m}^{-2}$ in the example of Fig. 4.12. Thus, the adhesion energy is about a factor 30 higher.

In the micrograph of Fig. 4.12 the capillary length is $\lambda = (180 \pm 40) \text{ nm}$ determined at sites of weak adhesion (position 0 and 9 in the figure). The absolute error in λ is smaller than for weaker adhering vesicles, as the onset of the deflection can be determined more precisely. For tight adhesion domains (dark areas in the micrograph) the equilibrium tension is the lowest tension measured, excluding domains with a large contact line curvature (positions 1, 2, 5, 7). In these domains the simplifications of the RB model assuming a circular contact line are not valid (Bruinsma 1995, Guttenberg et al. 2000).

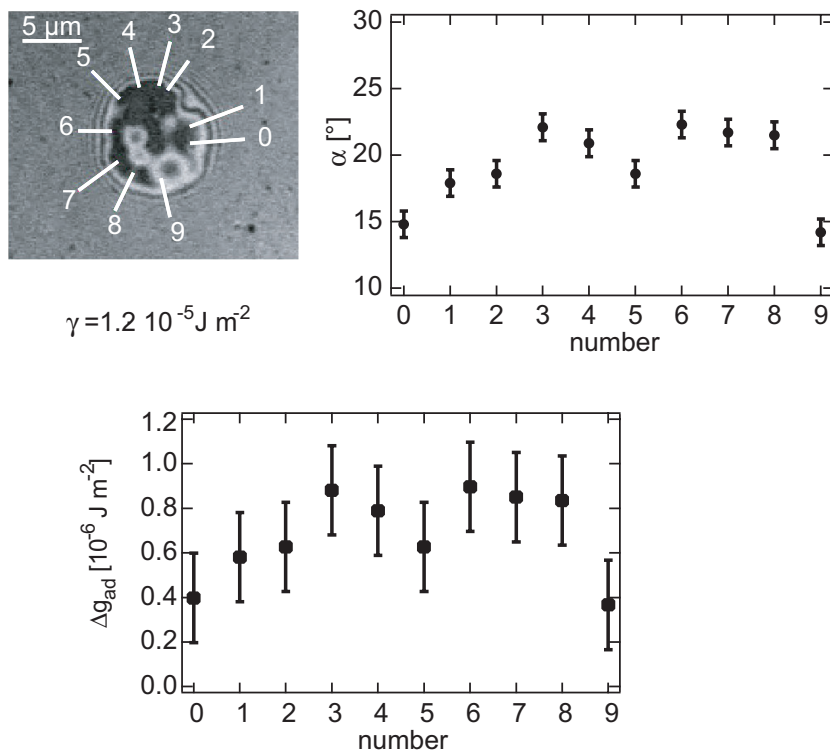


Figure 4.12: RICM micrograph of a giant vesicle (1% RGD lipid and 2% PEG lipid) in contact with an integrin/cellulose substrate. Values of the membrane tension γ , contact angles α (circles) and free adhesion energies Δg_{ad} (squares) are given in the graphs.

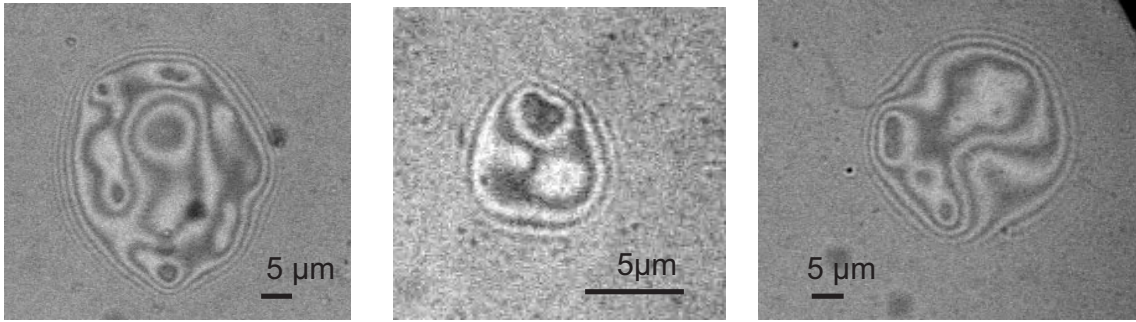


Figure 4.13: RICM micrographs of a giant vesicles (1% RGD lipid and 3% PEG lipid) adhering to a integrin/cellulose membrane.

3 mol% PEG Lipid in the Vesicle Membrane Fig. 4.13 shows micrographs of adhering vesicles to an integrin/cellulose substrate. The vesicles contain 3 mol% PEG lipids. The comparison of the micrographs shows that the adhesion of the vesicles with the higher repeller concentration is weaker than for 2 mol% PEG lipid, because in Fig. 4.13 only a part of the contact area appears dark. The measurement of the free energy per unit area yields $\Delta g_{ad} = (25 \pm 10) \times 10^{-8} \text{ J m}^{-2}$, as shown in Fig. 4.14, with $\gamma = (3 \pm 0.8) \times 10^{-6} \text{ J m}^{-2}$ resulting from $\lambda = (365 \pm 50) \text{ nm}$.

Summary of the Adhesion Energies The free adhesion energies per unit area measured for a given set of repeller concentrations at various sites of the adhesion disc agree remarkably well. This is confirmed by all measurements of this chapter. The agreement demonstrates that the vesicles are in a thermodynamic equilibrium, which is important to obtain reproducible results. The adhesion energy Δg_{ad} obtained for different concentrations of repeller molecules and 1% RGD-lipid onto different substrates are presented in the histogram in Fig. 4.15. In Table 4.1 the mean values of Δg_{ad} for the different configurations is given.

The origin of the order of magnitude variation in the free adhesion energy between the two different substrates, which is documented by the different appearances in the micrographs, requires an explanation. This will be given in the next paragraph by comparing the free adhesion energies with the specific adhesion energies of the receptor-ligand pairs.

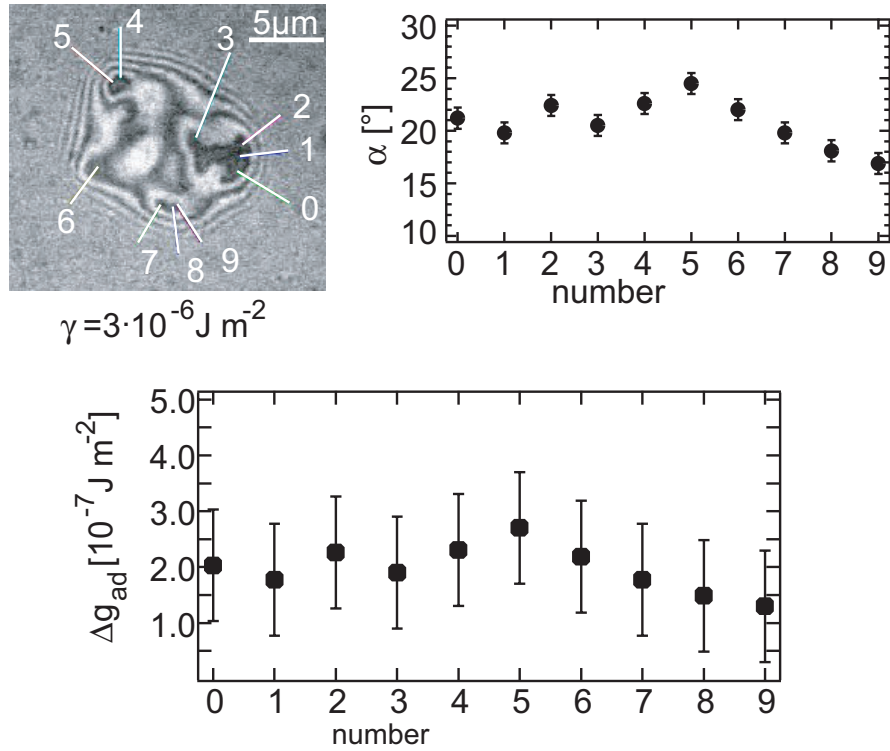


Figure 4.14: RICM micrographs of a giant vesicle (1% RGD lipid, 3% PEG lipid) adhering to an integrin/cellulose membrane. The membrane tension γ , contact angle α (circles) and free adhesion energy densities Δg_{ad} (squares) are given for the indicated positions.

Table 4.1: Summary of free adhesion energies Δg_{ad} for giant vesicles adhering to membranes on bare glass and on cellulose films, respectively. The molar integrin concentration on the substrate is 1:14000 and the RGD concentration is 1% for all data shown in the table. The free energies are given in J m^{-2} .

system	Δg_{ad} cellulose cushion	Δg_{ad} bare glass
$c_R = 2\%$	$30 \dots 110 \times 10^{-8}$	$2 \dots 9 \times 10^{-8}$
$c_R = 3\%$	$10 \dots 30 \times 10^{-8}$	

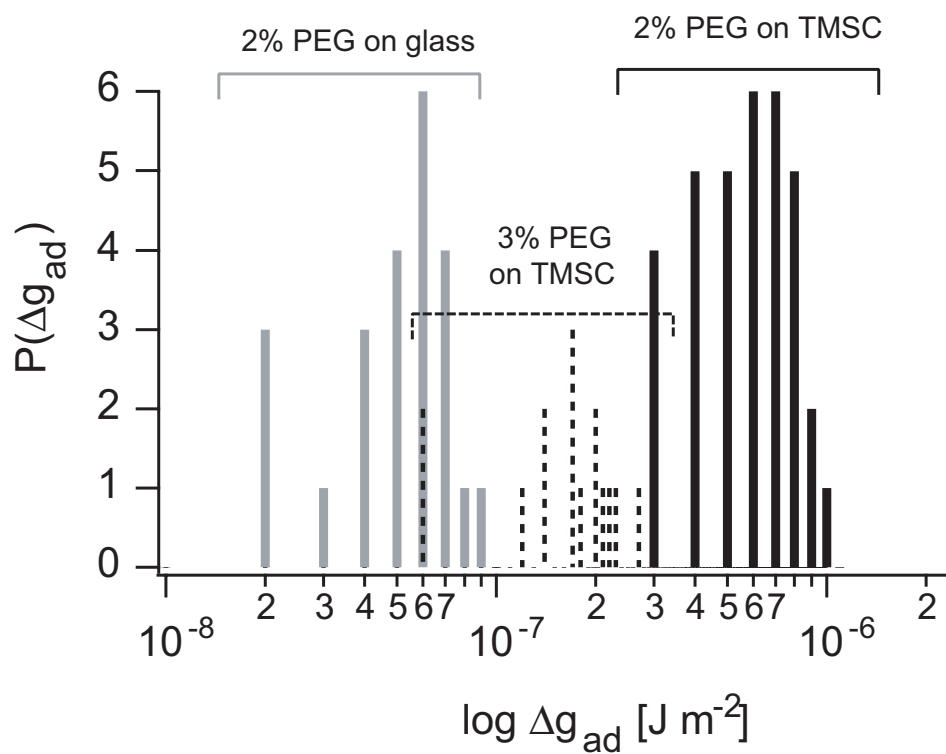


Figure 4.15: Histogram of measured values for the free energies Δg_{ad} of adhesion of vesicles. The vesicles adhering on cellulose membranes contain 2 and 3 mol% of repeller lipids (black and dotted lines, respectively) and the vesicles adhering on bare glass substrates contain 2 mol% PEG-lipids (gray lines).

4.5.3 Specific Adhesion Energy of the Integrin-RGD Binding

A comparison of the measured values of the free adhesion energy Δg_{ad} for strong adhesion sites with the specific adhesion energy W_{ad} (cf. (4.16)) is attempted. From concentration measurements the accessible integrin receptor density $n_I \approx 7 \times 10^{13} \text{ m}^{-2}$ can be estimated. Thereby it is assumed firstly that the integrin concentration within the strong adhesion plaque is about equal to the initial concentration and secondly that 50% of the integrins exhibit the functional headgroup towards the aqueous phase.

The binding energy of the receptor-ligand pair has not been measured yet, but it can be estimated from the dissociation constant of the hexapeptide-integrin pair, $k_{D(I-RGD)} \approx 1.1 \times 10^{-6} \text{ M}$ (Hu et al. 2000). This k_D -value is a factor of 10^9 smaller than the corresponding value reported for the biotin-streptavidin bond ($k_{D(B-S)} \sim 10^{-15} \text{ M}$), which has a binding energy of $w_{ad(B-S)} \sim 35k_B T$ (Green 1963, Bayer 1990). This approach yields $w_{ad(I-RGD)} \sim 10k_B T$ for the integrin-RGD binding energy. The specific adhesion energy in our experiment is then expected to be of the order of $W_{ad} \approx n_I \cdot w_{ad(I-RGD)} \approx 3 \times 10^{-6} \text{ J m}^{-2}$. According to Fig. 4.15, this value is only 3 and 10 times larger than the largest spreading pressure Δg_{ad} found for vesicles containing 2% and 3% PEG lipids, respectively. It is 30 times larger than the largest value of Δg_{ad} found for vesicles containing 2% PEG lipids on bare glass substrates (cf. Fig. 4.15).

The relatively small discrepancies between the values of W_{ad} and Δg_{ad} for the cellulose covered substrates can be understood as follows. The free adhesion energy depends not only sensitively on the receptor and ligand densities and their binding energy, but also on the repeller concentration c_R . A two-dimensional osmotic pressure difference between the adhesion plaque and the non-adherent membrane regions drastically reduces the free energy of adhesion (Bell et al. 1984, Bruinsma et al. 2000). If the local repeller concentration in the adhesion domain is assumed to be zero and the area per lipid is 100 \AA^2 , the osmotic pressure would be $\Delta\pi_R \approx 8 \times 10^{-5} \text{ J m}^{-2}$ (for 2 mol% PEG lipid), according to Eq. (4.15). This value is much higher than the measured spreading pressure ($\Delta g_{ad} = 1 \times 10^{-6} \text{ J m}^{-2}$, cf. Fig. 4.15). In order to account for the difference between the spreading pressure Δg_{ad} and the estimated specific interaction energy W_{ad} , we calculate the energetic difference to $2 \times 10^{-6} \text{ J m}^{-2}$ for the case of 2% PEG after Eq. (4.16). The concentration difference Δc_R necessary to generate this difference is determined to $\Delta c_R \sim 0.03 \cdot c_R$. The existence of a rather high density of PEG lipids in the tight adhesion plaques suggested by the above consideration can be explained in terms of the larger integrin headgroups ($\sim 12 \text{ nm}$) as compared to the Flory radius of the PEG lipid $R_g \approx 3 \text{ nm}$ (Kenworthy et al. 1995, Majewski et al. 1998).

The determination of the specific adhesion energy W_{ad} between a single receptor-ligand pair requires measurements of the free adhesion energy as function of the

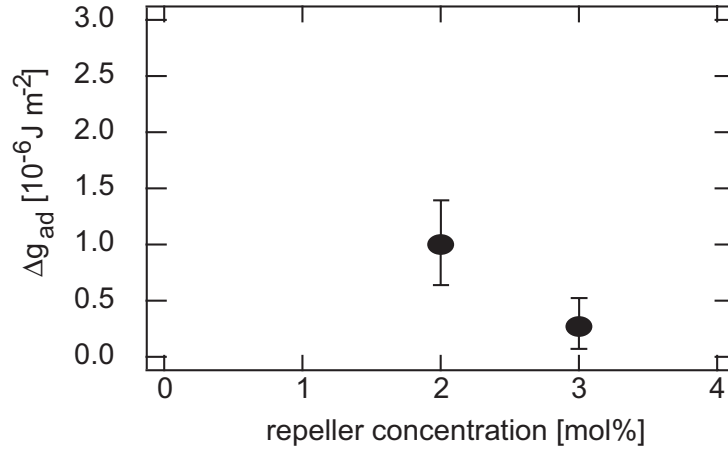


Figure 4.16: Dependence of the measured free adhesion energy Δg_{ad} on the repeller concentration in the membrane.

repeller and ligand concentration, cf. Eq. (4.16). As noted before, the osmotic pressure of the ligand is expected to be negligible due to their small size. Fig. 4.16 shows the dependency of the free adhesion energy Δg_{ad} on the repeller concentration. Although there are only two different receptor densities measured the plot is extrapolated versus the molar PEG concentration c_R to $c_R = 0$. In the work of Guttenberg (2000) a linear dependence on the concentration is demonstrated for the concentrations between 0 mol% and 5 mol% of PEG lipids. The extrapolation of g_{ad} yields a free adhesion energy at $c_R = 0$ of $\Delta g_{ad}(c_R=0) = (2.5 \pm 0.8) \times 10^{-6} \text{ J m}^{-2}$. The value of Δg_{ad} agrees well with the predicted specific adhesion energy in the tight adhesion plaques $W_{ad} = 3 \times 10^{-6} \text{ J m}^{-2}$ (see above). It is therefore concluded that the mobile integrin receptors do not accumulate remarkably in the tight adhesion domains. Possibly the accumulation of the receptors is impeded by the presence of repeller molecules.

The smaller value of the free adhesion energy for a vesicle adhering on pure glass supported membranes is attributed to the denaturing of receptors since the osmotic pressure effect should be very similar to that of the vesicle on polymer supported membranes. In the work of Guttenberg (2000) a detailed study of the amount of functional integrin is given. For integrin physisorbed on bare glass substrates, the functional percentage is determined to 39%. Naively, the results here would suggest that only 10% of the integrins in contact with bare glass remain functional. However, due to the absence of the cellulose film in these experiments, the distance of the adhering vesicle to the solid substrate surface is smaller. Therefore more repellors are expected to be expelled from the adhesion domain in comparison to the integrin/cellulose system, which results in a larger reduction of the measured free adhesion energy in comparison to the cellulose system.

4.6 Conclusions on the Adhesion Studies

The adhesion process studied here is controlled by the interplay of the short range attraction between receptor-ligand pairs and the long range generic repulsion of the polymers (repellers). Observation of strong adhesion domains in micro-interferograms confirm a functional incorporation of integrin $\alpha_{IIb}\beta_3$ into artificial lipid membranes. The adhesion strength can be determined from the free adhesion energy Δg_{ad} , also called spreading pressure, of a vesicle to the substrate. It is a well characterized quantity, accounting for the specific adhesion energy, the number of bonds and the repulsion generated by repellers. To obtain reliable values of the spreading pressure the vesicle has to be in equilibrium. A comparison of the adhesion energy to different substrates reveals that for identical vesicle compositions, the values differ by a factor of 30 between the integrin/cellulose substrate and the integrin/glass substrate. This suggests that the receptors denature partially if they are in contact to inorganic glass substrates and demonstrates the crucial importance of bioanalogue substrates used here.

The studied adhesion process is observed to be accompanied by adhesion plaque formation very reminiscent to focal adhesion points. In the adhesion plaque the repeller concentration can be determined to be only about 3% smaller than in the free membrane. The repeller depletion is thus weak for the present system. This can be explained since the Flory radius of the repellers $R_g = 3\text{nm}$ is smaller than the radius of the receptor headgroups $\sim 12\text{nm}$.

Since the free adhesion energy Δg_{ad} is equal to the difference between the specific energy W_{ad} and the lateral osmotic pressure exerted by the repeller molecules $\Delta\pi_R$, measurements of Δg_{ad} as a function of the repeller concentration allow for an estimate of the specific surface energy. By extrapolating the free adhesion energy Δg_{ad} versus the PEG lipid concentration c_R to $c_R = 0$, the specific adhesion energy can be estimated. Since the approximate number of bonds is known from the mean receptor concentration, the energy of a single receptor-ligand binding can be estimated to $w_{ad} \simeq 10 \text{ k}_B\text{T}$ for the integrin/cellulose system. Additionally, this result suggests that the functionality of the receptors is largely maintained for the bioanalogue substrate.

The presented technique provides a simple and powerful tool to measure relative receptor-ligand binding energies under bioanalogue conditions. However receptor condensation can not be taken into account so far.

4.7 Outlook: Controlling the Adhesion Area

A better estimate for the specific adhesion of a vesicle would require an independent measurement of the receptor density in the adhesion plaque. The assumed average receptor density gives rise to a large uncertainty in the determination of the specific receptor-ligand binding energy w_{ad} . Different strategies to achieve a defined

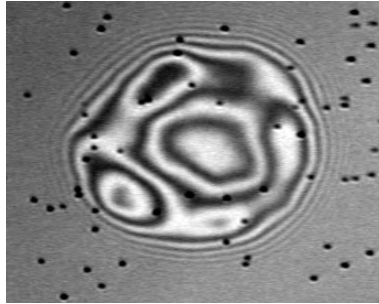


Figure 4.17: RICM micrograph of 40 nm colloidal gold beads lying on a silanized glass substrate. A giant vesicle is hovering over the substrate without any detectable strong adhesion domain.

number of functional receptors are explored and some insights can be obtained from preliminary experiments.

In a first approach the adhesion domain and thereby the number of receptors is defined by nanometer sized beads. The gold beads of 40 nm size are still visible in the RICM and thus the adhesion to a bead can be observed. By the well characterized surface density of the proteins and the countable number of beads involved in the adhesion process one can deduce the absolute number of involved proteins quite precisely. For simplicity, the experiments are performed with the protein streptavidin which binds specifically to the ligand biotin exhibited by the vesicles. The streptavidin biotin binding is used very often in biochemical assays, as the binding is very strong and the two macromolecules are quite stable and therefore easy to handle. The gold beads coupled to streptavidin are purchased from British Bio Cell International Ltd., Cardiff, UK, ready for use. By silanization of the substrate the beads can be physisorbed on the substrate in variable densities. The substrate is blocked with BSA, as described before. Giant vesicles with lipid anchored biotin-cap-DMPE (1 ... 5 mol%) are prepared and incubated to the substrate.

No specific adhesion of the giant vesicles to the beads can be observed, cf. Fig. 4.17. By increasing the receptor concentration in the vesicles and the surface concentration of the beads no reliable attachment can be achieved - it is more likely to lose the transparency of the substrate. Control measurements of a vesicle adhering to a plain streptavidin substrate and fluorescently labelled streptavidin adhering to the vesicles are both successful. A possible explanation for the non-binding might be the restricted number of bonds possible to form and the counteracting thermal undulations. Possibly even single biotin lipids which adhere to a bead are pulled out of the membrane.

Another approach is to deposit the adhesion proteins only to distinct areas of the substrate. A patterning of the surface can be achieved by the recently established micro-contact printing (μ CP) of proteins or membranes (Bernard et al. 1998, Xia and Whitesides 1998, Hovis and Boxer 2001, Renault et al. 2002). Fig. 4.18 shows

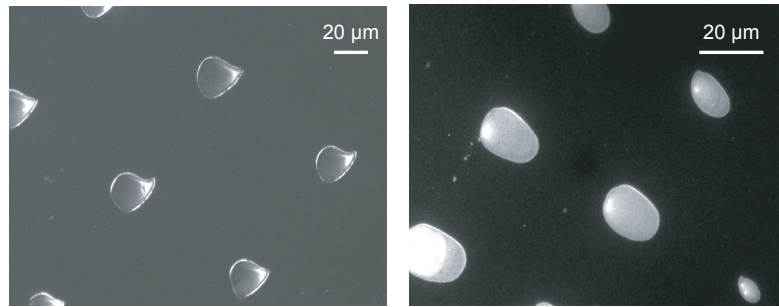


Figure 4.18: Fluorescently labelled adhesion molecules, which are deposited by micro-contact printing on a glass substrate. The two images show different patterns.

a fluorescent micrograph of printed streptavidin proteins. The ease of patterning surfaces is amazing, although the shown size is still much too large to control the number of bonds formed. Stamping membranes onto cellulose cushions in order to maintain the established bioanalogue conditions of the system would be a first achievement. Additionally, a determination of the minimal size of a patch necessary to attach a membrane with a given binding strength would be another interesting question. However, many different masks are necessary for these investigations. Nevertheless, this seems a promising approach for future studies.

Chapter 5

Magnetic Tweezers

5.1 Introduction

The ability of cells and organisms to maintain functionality in the presence of external forces is of crucial importance. For example, adhering leukocytes - described in the introduction of the previous chapter - have to resist hydrodynamic shear fields generated by the blood circulation. Moreover, many essential functions of living organisms require active force production (e.g. chromosome separation during cell division). Therefore the study of mechanical forces on cells and molecules is a rapidly expanding field (Merkel 2001). We will here focus on quantitative approaches to elucidate the effect of external forces upon receptor-based cell adhesion. The central question is: how do specific bonds react to applied mechanical forces? This can be studied either by investigations of single bonds, or by experiments on systems exhibiting ensembles of bonds.

The failure of bonds is predicted to be a statistical process. Any bond will fail, even without applied forces on the time scale of spontaneous dissociation, which can be of course infinitely long (Bell 1978). Upon the action of a force the statistical life time of the bonds is expected to decrease, since the force effectively reduces the energy barrier for bond dissociation. This behavior can be described in terms of a modified Arrhenius law of chemical kinetics, which was derived on the basis of statistical thermodynamics by Kramer (Dembo et al. 1988, Evans and Ritchie 1997).

A manifold of different experimental techniques have been set up to investigate the force induced dissociation of specific bonds, including atomic force microscopy (AFM) (Florin et al. 1994), micropipette aspiration (Evans and Ritchie 1997, Simson et al. 1999), optical tweezers (Mehta et al. 1999), surface force apparatus (SFA) (Leckband 1995), and shear flow experiments (Tha et al. 1986, Lorz et al. 2000).

In measurements of unbinding forces, the applied force F_{pull} is increased linearly with time t , a so-called force rate $\dot{F}_{pull} = \frac{d}{dt}F_{pull}$ is applied. For single molecule measurements it was shown, that for each force rate one obtains a distribution of unbinding forces. However, there is a clear dependence: the higher the applied force

rate, the larger is the unbinding force for a single molecular bond (Alon et al. 1995, Merkel et al. 1999). The unbinding force depends linearly on the applied force rate. Two recently published review articles give an overview on the understanding of the dynamic force spectroscopy on single molecules (Merkel 2001, Leckband and Israelachvili 2001).

In contrast, experiments on ensembles of receptor-ligand pairs are not well understood to date. The situation is more complex, as different bonds interact. However, insights would be of great interest, since the interaction between receptors and conjugate ligands in biology is not a single molecule process, but depends on collective phenomena and membrane elasticity. Many receptor-ligand pairs act together and share the applied mechanical load, what may lead to very different situations. For instance, in these systems, one single broken bond may be reestablished because the other bonds still hold the cells in place (Bell et al. 1984, Dembo et al. 1988). Additionally, the membrane-bound repeller molecules such as the glycoproteins of the glycocalix reduce the adhesion free energy, and bonded pairs of adhesion molecules are likely to be in local chemical equilibrium with free ligands and receptors. It has been shown that these collective effects result in a significant lowering of the effective adhesion energy, cf. the previous chapter (Bruinsma et al. 2000). Moreover, scaling theories predict a root mean square dependence of the unbinding force on the force rate and the number of bonds (Seifert 2000). Micropipette experiments on Jurkat or endothelium cells (Tozeren et al. 1992, Prechtel et al. 2002) revealed that the mechanical adhesion strength depends very strongly on the duration of force application and the number of bonds initially formed. Qualitatively, the same effect as for single bonds was found: for a slower force application (smaller force rates \dot{F}_{pull}) the yielded unbinding forces are lower. In experiments in shear flows, the decay of many bonds in time upon the action of a force could be analyzed in detail for the first time (Tha et al. 1986, Lorz et al. 2000).

In the following chapter we will report on an in-vivo, mesoscopic method allowing to measure unbinding forces of an ensemble of ligand-receptor pairs. To this end we apply constant lift forces in the range of 2...100 pN on adhering vesicles in a direction normal to the adhesion plane. Since the lift force is generated by a magnetic gradient field acting on a paramagnetic particle, the method is called *vertical magnetic tweezers*. The RICM allows for a real time observation of the adhesion disc and enables to monitor the detachment of local pinning centers from the adhesion area.

5.2 Magnetic Tweezers

The magnetic tweezers setup consists of an electromagnet, which is placed in the vicinity of the measuring chamber on a microscope. The magnet generates a gradient field, which in turn can exert a force on ferro- or paramagnetic beads in the sam-

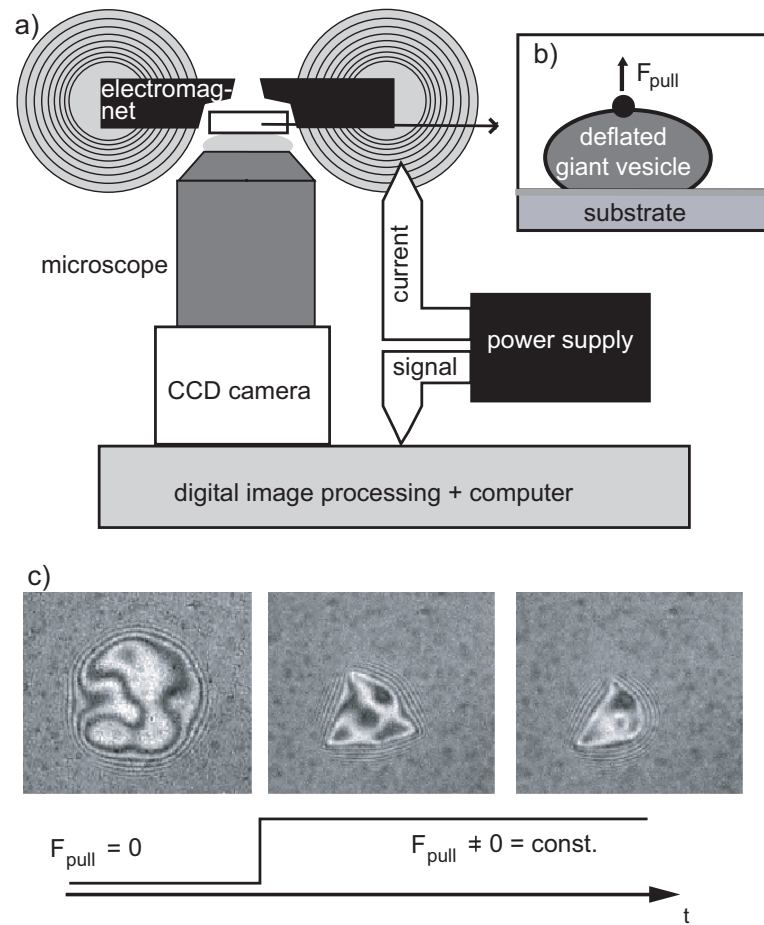


Figure 5.1: (a) Depiction of the vertical magnetic tweezers experiment. The electromagnet generates a magnetic gradient field in the vicinity of a sample which is mounted on top of an inverted microscope. The sample consists of a paramagnetic bead attached to a vesicle, which are drawn at an enlarged scale in (b). In (c) three RICM micrographs of the contact area of the vesicle are shown. In the first image no vertical force is applied, while in the second and third image a constant vertical pulling force is acting on the vesicle. Upon the action of a pulling force F_{pull} , the vesicle is lifted from the surface and centers of strong adhesion (pinning centers) appear gradually. Between the second and the third micrograph a pinning center is unbound.

ple. The principle of the magnetic tweezers is used for many different studies: Most widely used are horizontal magnetic tweezers to measure the viscoelastic properties of polymeric and biological networks as well as cells (Heilbronn 1922, Yagi 1961). There the deflection of the bead due to the magnetic force is monitored by a microscope. In particular, measurements of the frequency dependence of the viscoelastic moduli were a big step forward in establishing the magnetic tweezers as a rheometer (Lutz et al. 1973, Ziemann et al. 1994, Hinner et al. 1998). The first vertical magnetic tweezers setup was reported for measurements of the elasticity of single molecules (Strick et al. 1996).

In the present work, a vertical magnetic tweezers setup is realized by placing an electromagnet above the measuring chamber, cf. Fig. 5.1. By varying the current through the solenoid, or by changing the distance d between the measuring chamber and the magnetic poles, the vertical force at the position of the sample can be varied. A paramagnetic bead in the sample is transducing the magnetic force to the cell or vesicle studied, cf. Fig. 5.1b. The action of the force on the contact area of the cell or vesicle is observed in real time via the RICM or in bright field.

5.2.1 Setup

The vertical magnetic tweezers designed here can be mounted onto a microscope Axiovert 200 (Zeiss, Germany), which allows to observe the sample by fluorescence microscopy and RICM. Additionally, the use of the magnetic tweezers and illumination of the sample from the top (bright field) are simultaneously possible, cf. Fig. 5.2. The electromagnet is attached to the microscope by fixing it to the frame of the microscope. By set screws, the magnet is adjusted in such a way, that it pulls exactly perpendicularly to the plane of the measuring chamber. Furthermore, it is still possible to move the measuring chamber freely on an adapted xy-table in order to observe different parts of the sample. The electromagnet is designed to have a strong field gradient perpendicular to the image plane of the microscope. It consists of a solenoid with a cylindrical iron core of 10 mm diameter, formed in a rectangular shape (7.5 cm \times 7.5 cm). The rectangle has got one gap of 4 mm as shown in detail in Fig. 5.3c. The coils are made with 0.85 mm diameter copper wire, each with 735 turns (resistance $R = 3.2 \Omega$). They are mounted on two opposing sides of the iron core, cf. Fig. 5.3.

5.2.2 Force transducers

Paramagnetic or ferromagnetic particles, which are attached to the giant vesicles, are used to transduce the force from the electromagnet to the vesicle. In a magnetic gradient field these particles are attracted in the direction of the highest gradient. The acting force \vec{F}_{pull} depends on the magnetic induction \vec{B} and the dipole moment

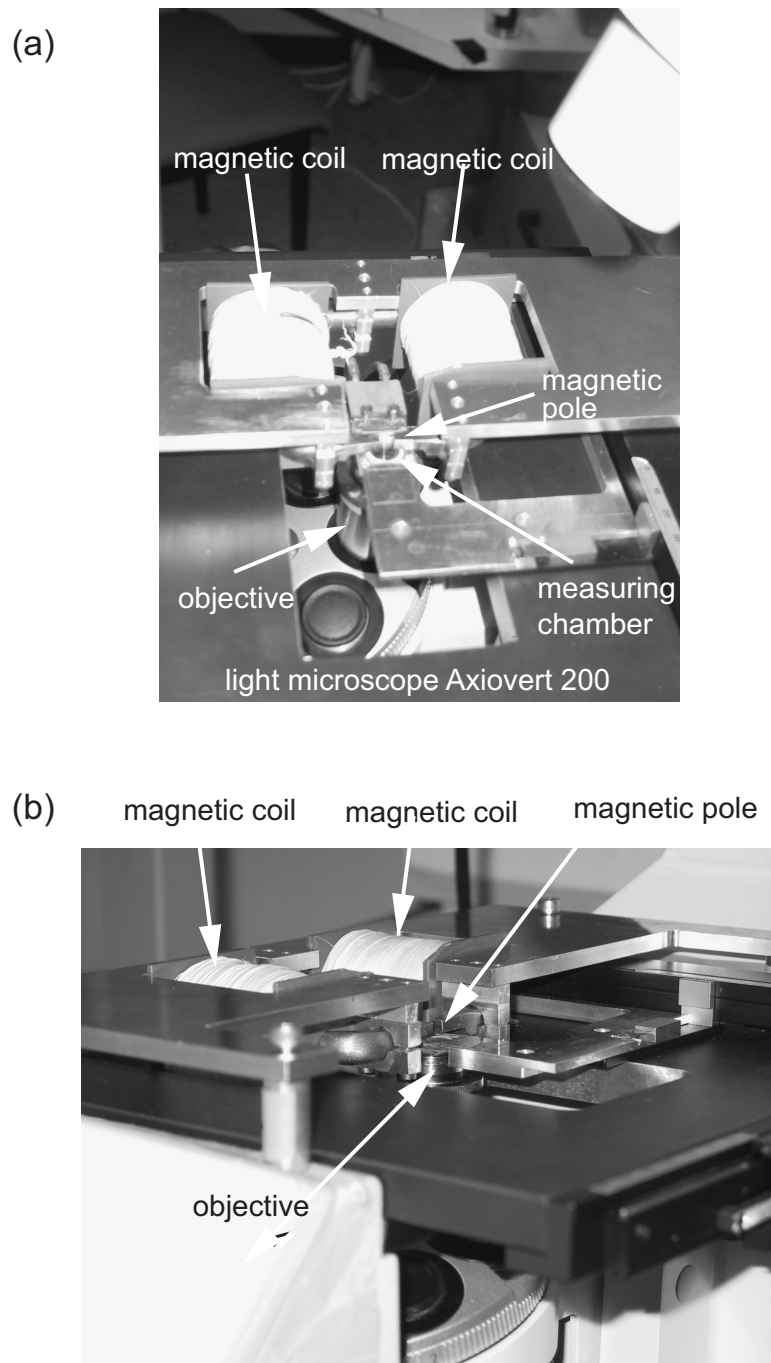


Figure 5.2: Two images of the vertical magnetic tweezers setup mounted on an inverted microscope (Axiovert 200). The length of the white coils is about 5 cm and their width is 4 cm.

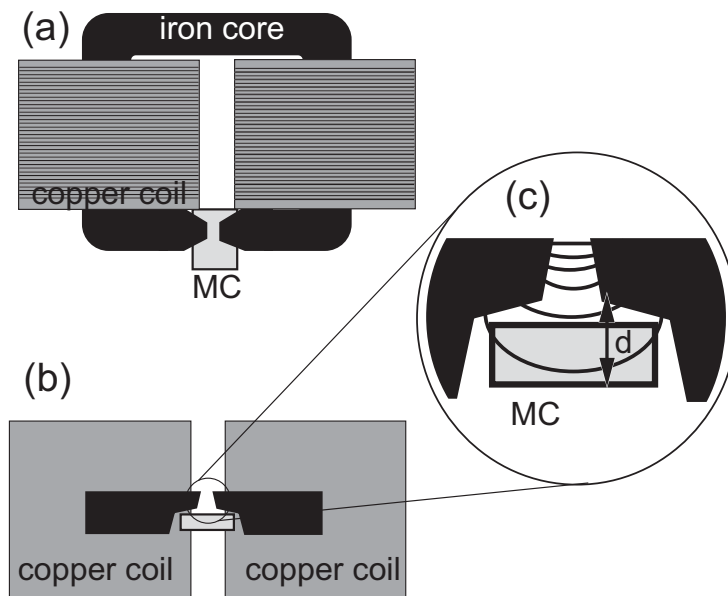


Figure 5.3: Shape of the electromagnet used for the vertical magnetic tweezers. a) Top view of the core and of the coils. The measuring chamber (MC) is indicated in light gray. b) Side view of the setup. The magnetic poles and the lines of force are depicted in c). The distance d between the magnetic pole and the substrate can be varied.

\vec{m} generated in the magnetic beads:

$$\vec{F} = \nabla(\vec{m} \cdot \vec{B}). \quad (5.1)$$

This equation can be simplified to $\vec{F} = (\vec{m} \cdot \nabla) \vec{B}$ in the stationary and current-free case. Thus, only a gradient in \vec{B} yields a force on the magnetic bead. Additionally, if the magnetic induction exceeds $B = 150$ mT (manufacturer notice) the magnetic dipole moment of the beads is constant with $|\vec{m}| = m_0 \approx 7.1 \times 10^{-13}$ Am², since they are fully magnetized.

To obtain reproducible forces the uniformity of the magnetic moment in the particles is crucial. Ziemann (1997) showed that polystyrene beads containing iron oxide particles purchased from Dynal, Norway are sufficiently uniform. We used Dynabeads M-450 with a diameter $d = 4.5$ μ m. Their size distribution is specified to 3% and their Fe₂O₃ iron content (19.6 ± 2) wt.%. Since the size of the iron grains is typically smaller than the size of the magnetic (Weiss) domains, the beads are not ferromagnetic but paramagnetic with a high magnetic susceptibility $\mu_r = 16 \times 10^{-5}$.

In order to attach the Dynabeads to vesicles or cells, the beads are purchased with a tosyl-activated surface. This group can form covalent bonds to amino-groups. Amino-groups are exhibited on the vesicle surface, since 1 mol% of amine-PEG lipid is incorporated into the vesicle membrane, as described in more detail in the experimental section 5.3.3.

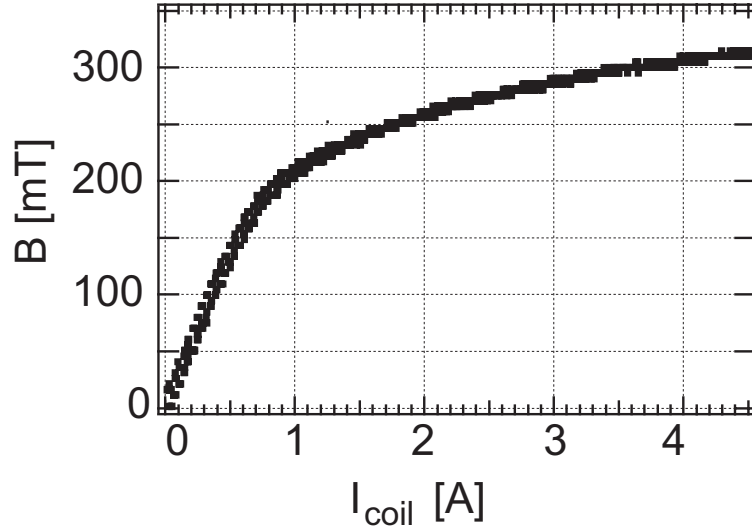


Figure 5.4: Variation of the induction B with the current I_{coil} through the magnetic coils. The magnetic field is measured by a Hall probe at the sample position.

5.2.3 Characterization

To determine the variation of the magnetic field with the current through the magnetic coil, the Hall voltage is measured at the position of the measuring chamber. The curve shown in Fig. 5.4 indicates a saturation of the magnetic induction \vec{B} at coil currents $I_{coil} \geq 1$ A, below that value \vec{B} depends linearly on I_{coil}

5.2.4 Calibration

The force calibration of the vertical magnetic tweezers setup is performed by lifting giant vesicles from the substrate. If the vesicles are free, i.e. not strongly adhered, the gravitational force G counteracts the lift force F_{pull} . G can be calculated for each vesicle from the volume measured in the bright field image by assuming a spherical shape of the vesicle and the specific weight difference $\Delta\rho = 50 \text{ kg m}^{-3}$ between the intravesicular solution and the outer solution:

$$G = \frac{4}{3}\pi r^3 \Delta\rho g \equiv F_{pull}, \quad (5.2)$$

where r is the radius of the vesicle, and $g = 9.81 \text{ m s}^{-2}$ is the gravitational acceleration.

To obtain the dependence of the pulling force on the current in the coil, the values of I_{coil} required to lift vesicles of different r and thus with different G , are measured and plotted in Fig. 5.5. Since the pulling force is proportional to the magnetic field (Eq. 5.1), the B versus I_{coil} diagram (Fig. 5.4) can be fitted to the measured data points. This yields a numerical function relating the applied current and the pulling

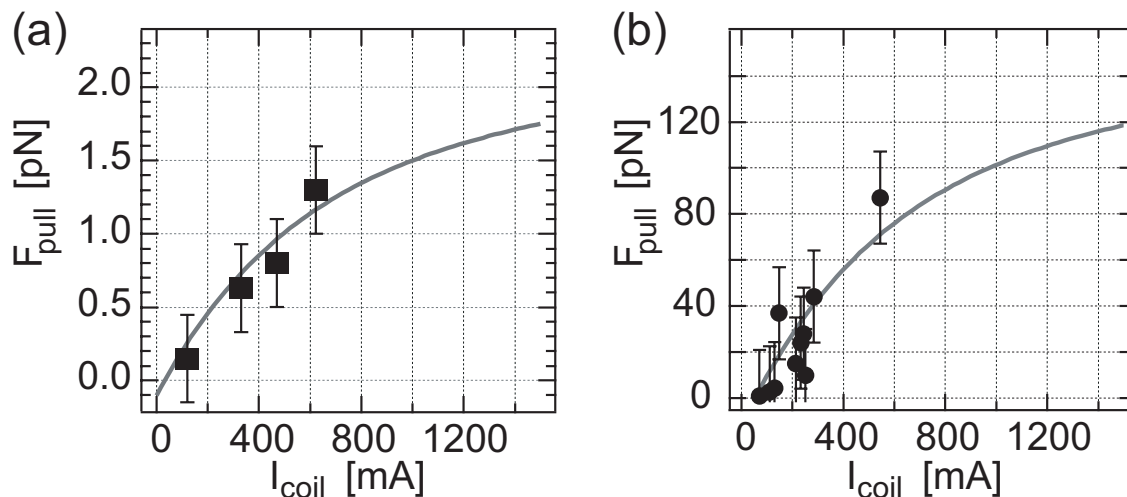


Figure 5.5: Dependence of the pulling force F_{pull} on the current I_{coil} through the magnetic coils for two different sample holders. The squares or circles indicate the measured data points, whereas the line is the fit of the B versus I_{coil} diagram (Fig. 5.4). In (a) the sample to magnet distance is $d = 4$ mm, whereas in (b) the distance is $d = 1$ mm.

force. In Fig. 5.5 two different force to current calibrations are displayed, which correspond to different sample holders: the first is reaching a force of 1.5 pN at 1 A, whereas the second reaches 100 pN at that current. This increase in force is due to a smaller distance d from the sample to the magnetic poles, depicted in Fig. 5.3c: for the first holder $d = 4$ mm, compared to $d = 1$ mm for the latter.

5.3 Materials and Methods

The unbinding experiments of giant vesicles are performed with two different receptor-ligand pairs, which exhibit a difference in binding affinity of roughly a factor 100.

5.3.1 RGD-containing Vesicles on Integrin-exhibiting Substrates

The preparation of the model system is described in detail in the previous chapter. The integrin-containing bilayers are supported either on bare glass substrates or on substrates covered by a cellulose film. Giant vesicles are prepared by electrosweating and their composition is slightly changed, as an additional lipid to attach the paramagnetic bead is necessary. They are composed of an equimolar mixture of DMPC and cholesterol, 1 mol% of DMPE with polyethylene glycol headgroups (PEG

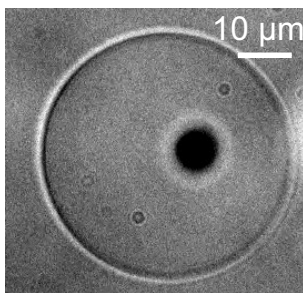


Figure 5.6: Bright field micrograph of a paramagnetic bead attached to a giant lipid vesicle.

lipid, molecular mass PEG = 2000), 1 mol% amine-PEG lipid (1,2-distearoyl-sn-Glycero-3-phosphoethanolamine-N-[amino(PEG)2000], Avanti Polar Lipids, Inc.), and 1 mol% of DMPE with a cyclic RGD peptide headgroup. All quantities are given with respect to the DMPC amount.

5.3.2 Sialyl-Lewis^X-containing Vesicles on E-Selectin Substrates

The specific receptor-ligand model system of Sialyl-Lewis^X and E-selectin has been established by Barbara Lorz, and the details are given in her thesis (Lorz 2003). The substrates are prepared by incubating silanized glass slides with different concentrations (1.5 and 2.5 $\mu\text{g ml}^{-1}$) of E-selectin in buffer *B* (cf. the Appendix) for 2 h and subsequently passivating the substrate by a 3 wt.% solution of casein in buffer *B* (1 h). The substrates are carefully rinsed and mounted on the microscope. The vesicles consist of an equimolar mixture of DMPC and cholesterol, 15 mol% of lipid coupled Sialyl-Lewis^X, 1 mol% of PEG 2000 lipid, and 1 mol% of amine-PEG lipid (with respect to the DMPC amount). For fluorescently labelled membranes 0.2 mol% of bodipy dye is added.

5.3.3 Attachment of Beads

To attach paramagnetic beads to giant vesicles, the vesicles are slightly deflated to generate some excess area and enable adhesion. An osmotic pressure of 10 to 15 mOsm across the vesicle membrane is applied by adding 200 μl of the freshly prepared giant vesicle suspension (170 mOsm) to a well vortexed solution with 185 mOsm. The latter consisted of 900 μl buffer *B*, 50 μl millipore water and 100 μl of the bead-stock solution. The whole vesicle-bead-suspension is rotated carefully for 1 h at room temperature, so that single beads can attach spontaneously to the vesicles, cf. Fig. 5.6. Finally, about one fourth of the giant vesicles have a bead sticking to them.

The bead stock solution is prepared by taking 10 μl of the purchased M-450 Dynabead solution and adding 1 ml of buffer B , yielding a concentration of 4×10^6 beads per ml. Before the beads are used, they are washed three times by exchanging the buffer, in order to remove stabilizing components of the buffer, in which the beads are suspended.

It should be noted that during the whole experiment and especially while injecting the vesicles and beads into the measuring chamber, a small magnetic pulling force ($F_{pull} \sim 250$ fN) is applied. This prevents the beads from sinking to the substrate and sticking strongly to it by non-specific forces which can not be overcome by the magnetic tweezers anymore. If the force is very small and just keeps the beads floating, the adhesion process of the vesicles to the substrate will not be influenced.

5.3.4 Laser Confocal Scanning Microscopy (LCSM)

The principle of a laser scanning microscope is fluorescent excitation and detection. In contrast to a conventional fluorescent microscope, in LCSM a focused laser illuminates a spot on the sample. This excited spot is observed through a pinhole, leading to a higher lateral resolution (factor 2 to 3) and to a smaller depth of focus (200-300 nm). By scanning the focus layer by layer from the glass surface to the upper side of the object, a three-dimensional reconstruction of the structures of the sample is possible (Pawley 1995). The setup used here is a microscope Odyssey XL (Noran, WI, USA), adapted to an Ar-Kr-Laser (wavelength 488, 567 and 647 nm).

5.4 Magnetic Tweezers Experiments

A pulling force acting on one point of the vesicle surface lifts the vesicle up if it does not adhere. However, if it adheres to the substrate the pulling force will result in an additional tension γ' and increase the contact angle between the vesicle and the substrate (Dembo et al. 1988). Both the resulting membrane tension and the contact angle can be analyzed from the RICM micrographs using the Bruinsma model, cf. chapter 4 (Bruinsma 1995). Since the theoretical model has initially been developed for spherical leukocytes adhering in a steady state, the predictions of the model need to be checked for the case of vesicles which are pulled upwards.

The line force f acting on the contact line of a pulled vesicle can be separated in an horizontal part f_{\parallel} and vertical part f_{\perp} :

$$\begin{aligned} f_{\parallel}(s) &= \gamma \cos \alpha(s) \\ f_{\perp}(s) &= \gamma \sin \alpha(s), \end{aligned} \tag{5.3}$$

where γ is the resulting membrane tension, α the resulting macroscopic contact angle and s the contour length.

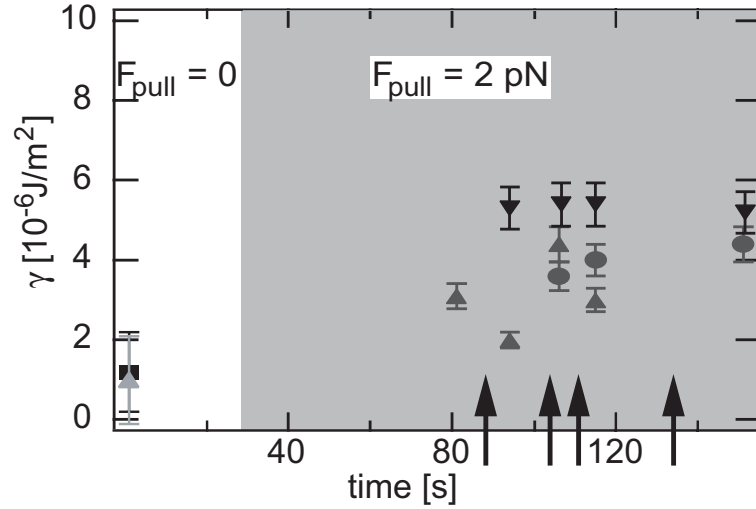


Figure 5.7: Graph of the membrane tension γ of the vesicle versus time. γ increases upon the action of a pulling force. Then, for $F_{pull} = \text{const.}$ γ is constant even after the unbinding of individual pinning centers, which is depicted by the arrows on the time axis.

By integrating the vertical line force f_{\perp} over the whole contour length s , the absolute vertical force F_{\perp} of the vesicle on the substrate can be obtained (Guttenberg et al. 2000):

$$F_{\perp} = \gamma \oint \sin \alpha(s) ds. \quad (5.4)$$

Note that f_{\perp} can be determined more accurately from the RICM micrographs than F_{\perp} , since the tension and contact angles can be averaged from different positions, whereas the contour length s is more difficult to measure accurately, especially if the vesicle is only locally adhered and exhibits pronounced pinning centers (PC).

5.4.1 Membrane Tension

The additional tension γ' - induced by the pulling force - has to be added to the membrane tension γ_0 of the adhered vesicle. For a selected vesicle the membrane tension γ is analyzed at different positions along the contact line and plotted versus time, cf. Fig. 5.7. In the force free state ($F_{pull} = 0$), the tension in the membrane is $\gamma = (1 \pm 0.5) \times 10^{-6}$ J m 2 . Upon pulling on the vesicle with 2 pN, the tension in the membrane increases to $\gamma = 3 \dots 6 \times 10^{-6}$ J m 2 . During the application of the force (indicated by the gray background) γ remains constant, even if individual pinning centers detach, as denoted by the arrows in Fig. 5.7.

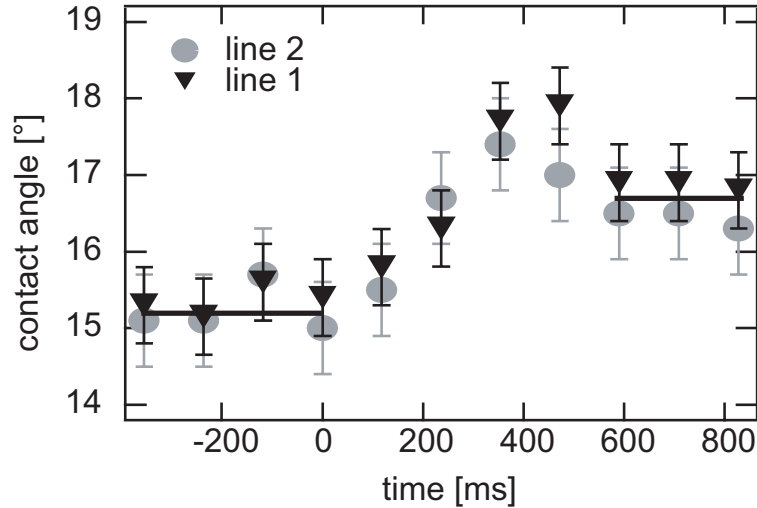


Figure 5.8: Changes of the contact angle α of the membrane at two different positions (gray and black symbols) during the unbinding of a pinning center. The unbinding takes place at $t = 0$ s.

5.4.2 Contact Angle

Since the membrane tension does not increase upon the unbinding of individual pinning centers (Fig. 5.7) the contact angle α has to increase according to Eq. (5.4). Indeed, Fig. 5.8 shows that the contact angle increases from $(15.1 \pm 0.5)^\circ$ to $(16.8 \pm 0.5)^\circ$ for the pinning center which unbinds at $t = 0$ s. The observed overshoot of the contact angle to 18° can be used to measure the response time of a vesicle, i.e. the time required by the vesicle to respond to the external force. For different vesicles of identical composition, we find that this response time is always about (350 ± 30) ms.

5.4.3 Vertical Force

By application of Eq. (5.4), we can now crosscheck the forces measured from the RICM micrograph with the force determined by the calibration. The force F_\perp acting on the vesicle is equal to the sum of the pulling force F_{pull} exerted by the magnetic tweezers and the free adhesion energy of the adhering vesicle W_{ad} multiplied by the contour length s .

$$\begin{aligned} F_\perp &= F_{pull} + W_{ad} \times s \\ &= F_{pull} + F_{ad}. \end{aligned} \quad (5.5)$$

Since W_{ad} and F_\perp can be measured independently by analysis of the RICM interferogram, the applied pulling force can be calculated (Guttenberg 2000).

W_{ad} is determined from the steady state RICM micrograph as discussed in the previous chapter. For the vesicle shown in Fig. 5.9 an adhesion energy of $W_{ad} =$

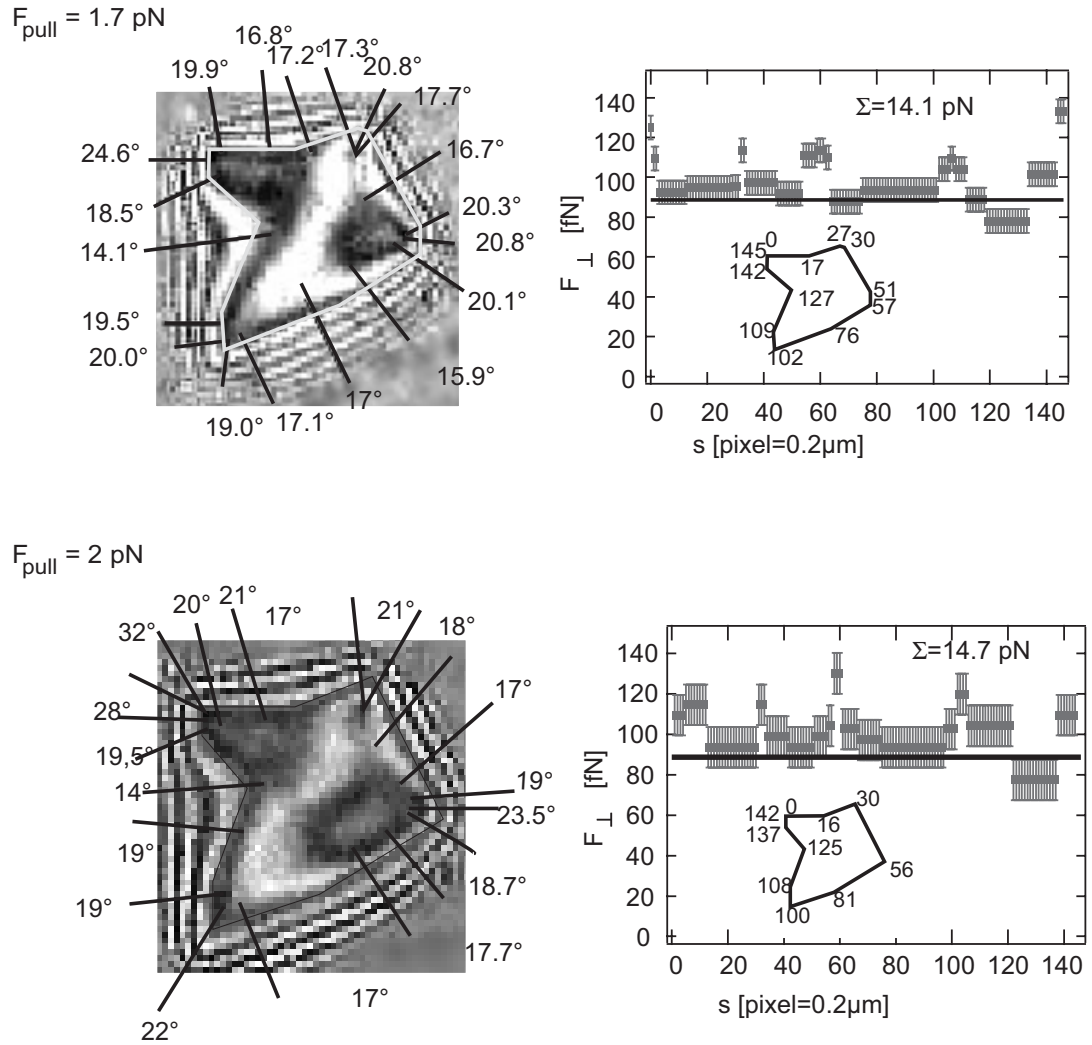


Figure 5.9: The black bars in the left micrographs show the directions along which the contact angles are measured. The forces F_{\perp} at the various positions along the contact line are indicated by the squares in the right graphs. The line denotes the force calculated from the tension of the vesicle, which is the steady state adhesion force F_{ad} of the pulled vesicle. The inset in each graph gives the contact line of the vesicle and enumerates the positions along the vesicle contact line.

$(4.4 \pm 0.2) \times 10^{-7} \text{ J m}^{-2}$ is obtained which yields $F_{ad} = (12.8 \pm 0.9) \text{ pN}$ with the contour length of the adhesion disc $s = (29 \pm 3) \mu\text{m}$. Eq. (5.4) is integrated by adding sections of the contour length with identical contact angles, as shown in Fig. 5.9. According to Eq. (5.5), the pulling force is $F_{pull} = F_{\perp} - F_{ad} = (1.3 \pm 0.9) \text{ pN}$ for the upper micrograph and $F_{pull} = (1.9 \pm 0.9) \text{ pN}$ for the lower one. The corresponding pulling forces obtained from the coil current calibration are $F_{pull} = (1.7 \pm 0.3) \text{ pN}$ and $F_{pull} = (2.0 \pm 0.3) \text{ pN}$, respectively, since the currents are $I_{coil} = 1.8 \text{ A}$ and $I_{coil} = 2.3 \text{ A}$ (cf. Fig. 5.5a). The two independently measured values for the pulling force agree well. Therefore the forces obtained by application of the Bruinsma model (RB, cf. section (Bruinsma 1995)) hold for the locally adhered vesicles which are pulled in the vertical direction.

5.4.4 Unbinding Experiments

RGD-Integrin Receptor-Ligand Pair on Integrin/Glass

Fig. 5.10a shows unbinding experiments of a vesicle which is adhered specifically to an integrin-containing bilayer (integrin/glass). The force applied in the experiments is $F_{pull} = 0$ at $t = 0$, $F_{pull} = 1.15 \text{ pN}$ for $t = 2.7 \text{ s}$ to 32.5 s and $F_{pull} = 1.8 \text{ pN}$ for the last seconds, as indicated by the force profile in Fig. 5.10b. Upon the application of a pulling force, the adhesion area in Fig. 5.10 exhibits distinct pinning centers (PC), which unbind from the substrate one after the other. The unbinding of the PCs seems to occur randomly, i.e. one can not predict which PC will be the next to detach. According to Eqs. (5.3-5.4) the unbinding line force f_{\perp} and the unbinding force F_{\perp} for each PC is calculated and plotted in Fig. 5.10b. We consider the outer length of the PC as the relevant length as shown in Fig. 5.12. The vertical force is believed to act only upon this line because here the contact angle is large, resulting in a high line force f_{\perp} according to Eq. (5.3) (Dembo et al. 1988, Guttenberg et al. 2000, Seifert 2000). Therefore, the force acting on one single PC is not symmetrical. However all the PCs in the adhesion disc together are supposed to retain the symmetry.

The dependence of f_{\perp} and F_{\perp} on the contour length of the pinning center s_{PC} is shown in Fig. 5.11, suggesting that f_{\perp} does not depend on s_{PC} , since an approximately constant value $f_{\perp} = (1.4 \pm 0.3) \text{ N m}^{-1}$ is obtained, whereas F_{\perp} increases with s_{PC} .

Since the contour length of the pinning center s_{PC} is proportional to the size of the adhesion domain, the observed increase of F_{\perp} with s_{PC} suggests that the density of the adhesion sites on the substrate is constant as depicted in Fig. 5.12. Adhesion sites can either be single receptors or receptor clusters. However, it is not possible to determine the number of bonds within one pinning center from the micrograph. Therefore only the average receptor density determined in chapter 4 can be used to estimate the unbinding force per receptor-ligand pair (cf. below).

In Fig. 5.13 the variation of the unbinding force F_{\perp} with the contour length of

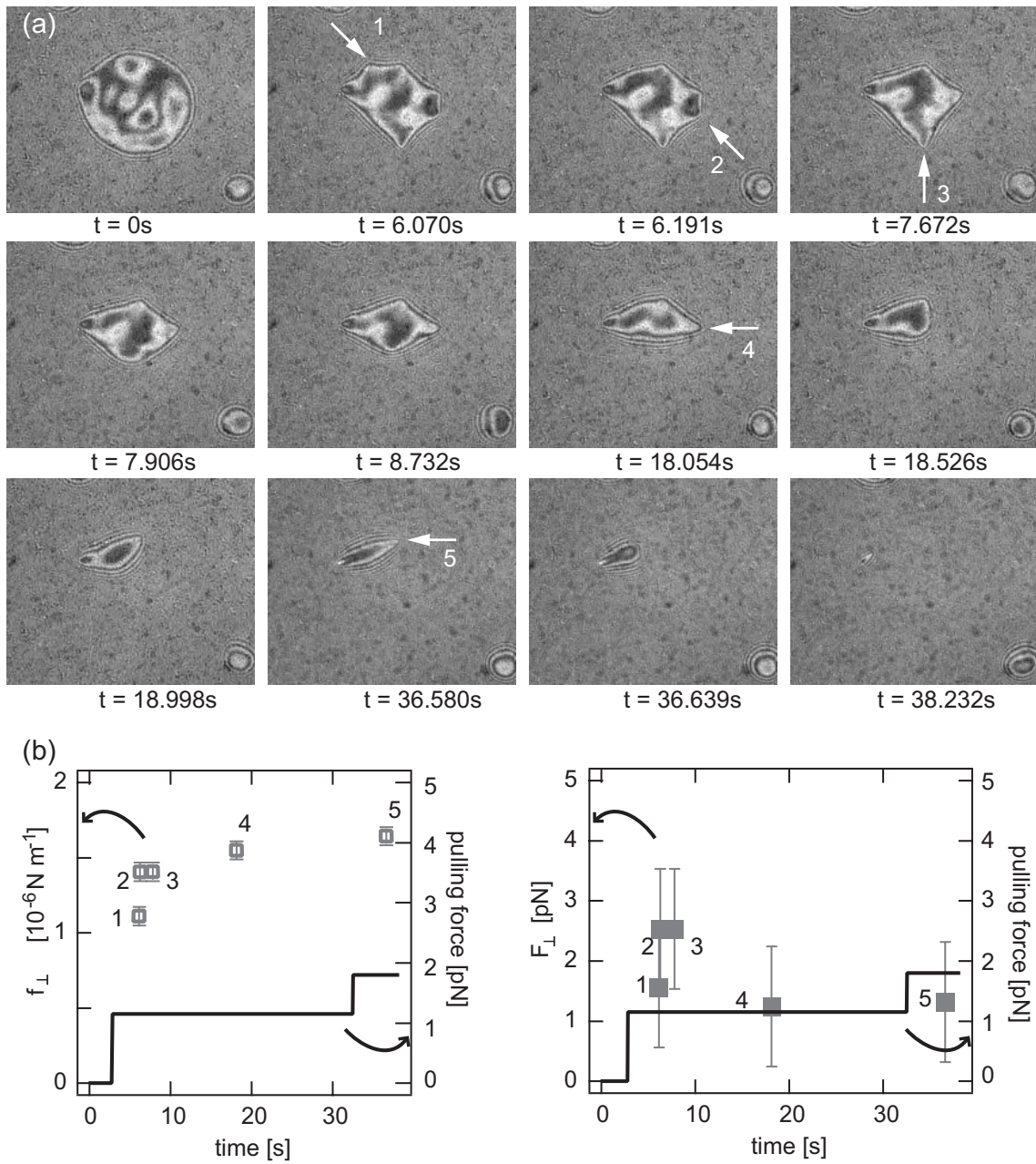


Figure 5.10: (a) Unbinding of a vesicle containing 50 mol% DMPC, 50 mol% cholesterol, 1 mol% RGD lipid, and 1 mol% PEG lipid, which adheres to an integrin/glass substrate. A constant force $F_{pull} = 1.15$ pN is applied to the vesicle at $t = 2.7$ s, and the pinning centers detach one after the other at $t = 6.070$ s, $t = 6.191$ s, $t = 7.672$ s, $t = 18.054$ s, and $t = 36.580$ s. (b) Evaluation of the unbinding line force f_{\perp} (open squares) and the unbinding force F_{\perp} (filled squares) for the single unbinding events enumerated in the micrographs above.

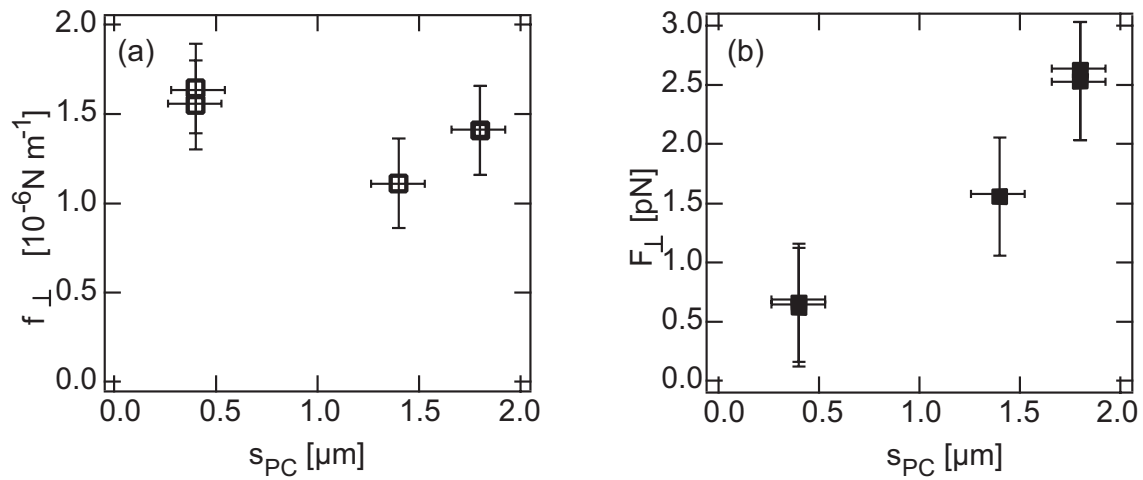


Figure 5.11: a) Unbinding line force f_{\perp} versus the pinning center contour s_{PC} , depicted in open squares. b) Total unbinding force F_{\perp} (filled squares) for pinning centers as a function of the pinning center contour length s_{PC} .

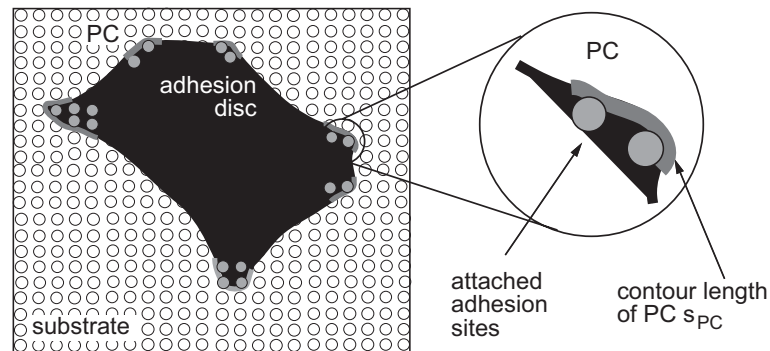


Figure 5.12: Sketch of the adhesion disc of a giant vesicle adhering to adhesion sites (open circles) on the substrate. The vesicle adheres strongly at the pinning centers (PC), which are supposed to consist of different numbers of adhesion sites (drawn as gray circles). The contour length of the pinning center s_{PC} is indicated by the dark gray line.

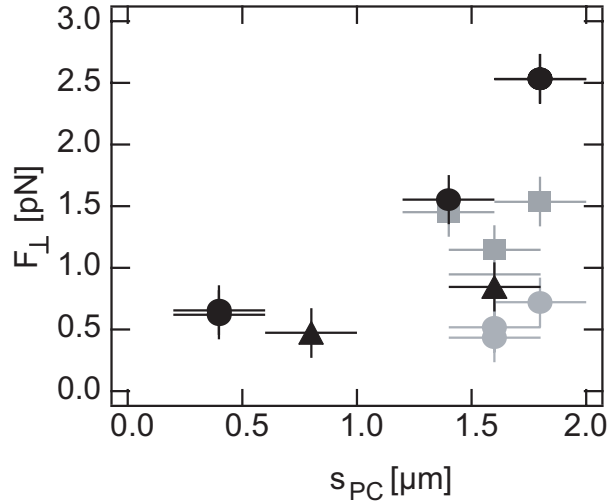


Figure 5.13: Unbinding force F_{\perp} as a function of the contour length of the pinning centers s_{PC} for different vesicles, indicated by different symbols.

the pinning center s_{PC} is shown for different vesicles. The pulling forces applied are $1.3 \text{ pN} \leq F_{pull} \leq 1.9 \text{ pN}$. Although the error bars are rather large, due to the uncertainty in determining s_{PC} and the vesicle tension γ , a clear trend is visible: F_{\perp} increases linearly with s_{PC} . A more detailed inspection of the figure shows that the slope is comparable for different vesicles but the offset in vertical direction varies. According to Eq. (5.4), this offset can be attributed to the different tensions γ of the different vesicles. However, since all samples (vesicles plus substrates) are prepared identically, and are subjected to similar pulling forces, γ should be constant. Thus, in good approximation an average tension $\bar{\gamma} = 2.2 \times 10^{-6} \text{ J m}^{-2}$ can be used in all the evaluations. Plotting the line force f_{\perp} obtained in this way versus s_{PC} clearly reveals a constant value of $f_{\perp} = (0.87 \pm 0.13) \times 10^{-6} \text{ N m}^{-1}$, whereas the force per pinning center F_{\perp} scales evidently with s_{PC} , cf. Fig. 5.14. The drastically reduced scatter in our data shows that the assumption that all vesicles have the same membrane tension $\bar{\gamma}$ is reasonable.

In Fig. 5.15a the histogram of the line forces f_{\perp} calculated for a constant tension $\bar{\gamma} = 2.2 \times 10^{-6} \text{ J m}^{-2}$ is displayed. A mean value of $f_{\perp} = (0.9 \pm 0.1) \times 10^{-6} \text{ N m}^{-1}$ is clearly obtained. The histogram of F_{\perp} presented in Fig. 5.15b exhibits different peaks, indicating different sizes of the pinning centers and thus different numbers of receptor-ligand pairs as depicted in Fig. 5.12.

Figures 5.14 and 5.15 show that the accuracy of the evaluation is improved by determining an average tension $\bar{\gamma}$ for the vesicles and calculating the unbinding forces with this value. The assumption that all vesicle should have the same tension is validated since they are all prepared identically, are deposited on similar substrates and subjected to similar pulling forces $1.3 \text{ pN} \leq F_{pull} \leq 1.9 \text{ pN}$. A large difference in their tensions γ would thus not be expected. Therefore, the measured deviation of

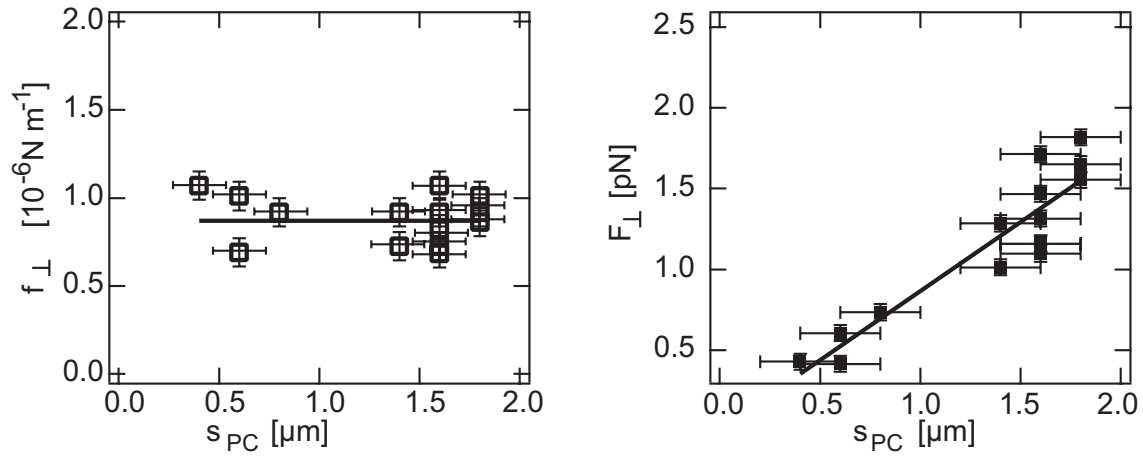


Figure 5.14: (a) The open squares show the unbinding line forces f_{\perp} of the pinning centers versus their contour length s_{PC} . The straight line represents the mean value. (b) Absolute unbinding forces F_{\perp} versus s_{PC} , depicted by squares. The straight line is a linear fit to the data. The forces are obtained from different vesicles, assumed to have all the same tension $\bar{\gamma}$.

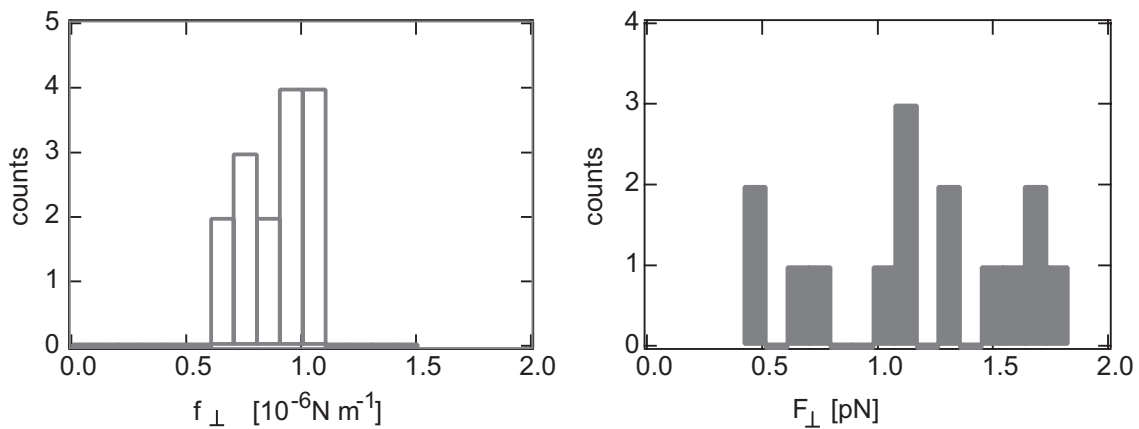


Figure 5.15: (a) Histogram of the unbinding line forces f_{\perp} for different pinning centers of identical vesicles. (b) Histogram of the unbinding forces F_{\perp} for different pinning centers.

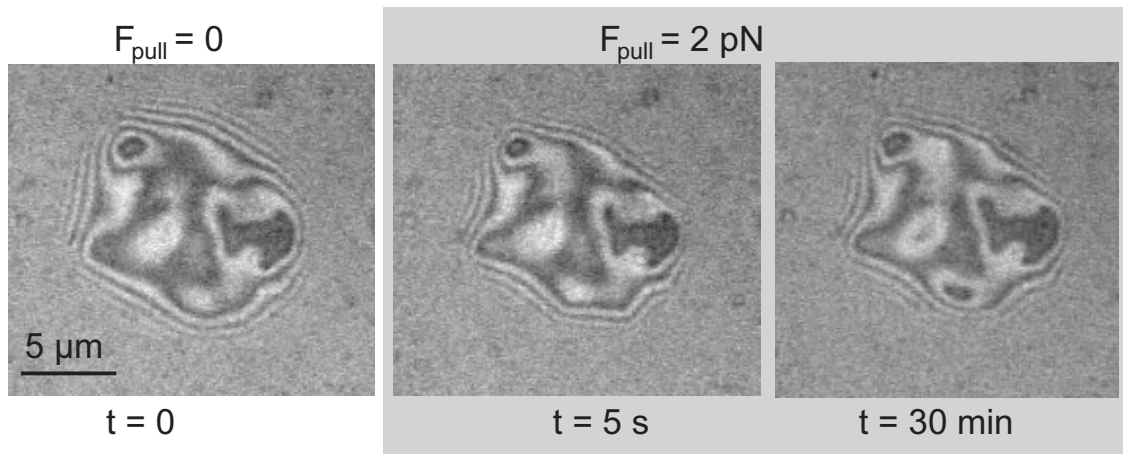


Figure 5.16: RICM micrograph of the adhesion area of a vesicle adhering specifically to the integrin/cellulose substrate. In the second and third micrograph a constant vertical pulling force is acting on the vesicle for 5 s and 30 min, respectively.

45% in γ for different vesicles must be due to the uncertainties in the determination of γ for the pulled vesicles. This arises from the difficulty to find a domain of the contact line in the micrograph which is not subjected to any further tension than the tension resulting from pulling and adhesion. In all the areas of the contact line with high curvatures like pinning centers and convex geometries the determination of the tension is not possible, since further contributions come into play (Bruinsma 1995, Guttenberg et al. 2000). An additional line force has to be introduced in order to balance the high curvature of the contact line. Therefore, the positions where the membrane tension γ can be determined are very limited and the values differ appreciably.

For the evaluation of the adhesion energy in the previous chapter these problems did not occur, since the vesicles were in a steady state. Thus, there were many different positions where the tension could be accurately determined. The values obtained for the tensions there differed only by 22%, demonstrating the much higher accuracy of these measurements.

We do not attempt to estimate the number of receptor per adhesion site here, since in the adhesion study of chapter 4 we showed that the functionality of the integrins on bare glass is strongly reduced ($\sim 30\%$). Therefore, such a consideration does not seem to be reasonable.

RGD-Integrin Receptor-Ligand Pair on Integrin/Cellulose

In contrast, on the integrin/cellulose cushions, the vesicles adhere much stronger and no unbinding can be observed upon applying a pulling force of 2 pN to the vesicle as shown in the example of Fig. 5.16. The figure suggests that the adhesion area rather

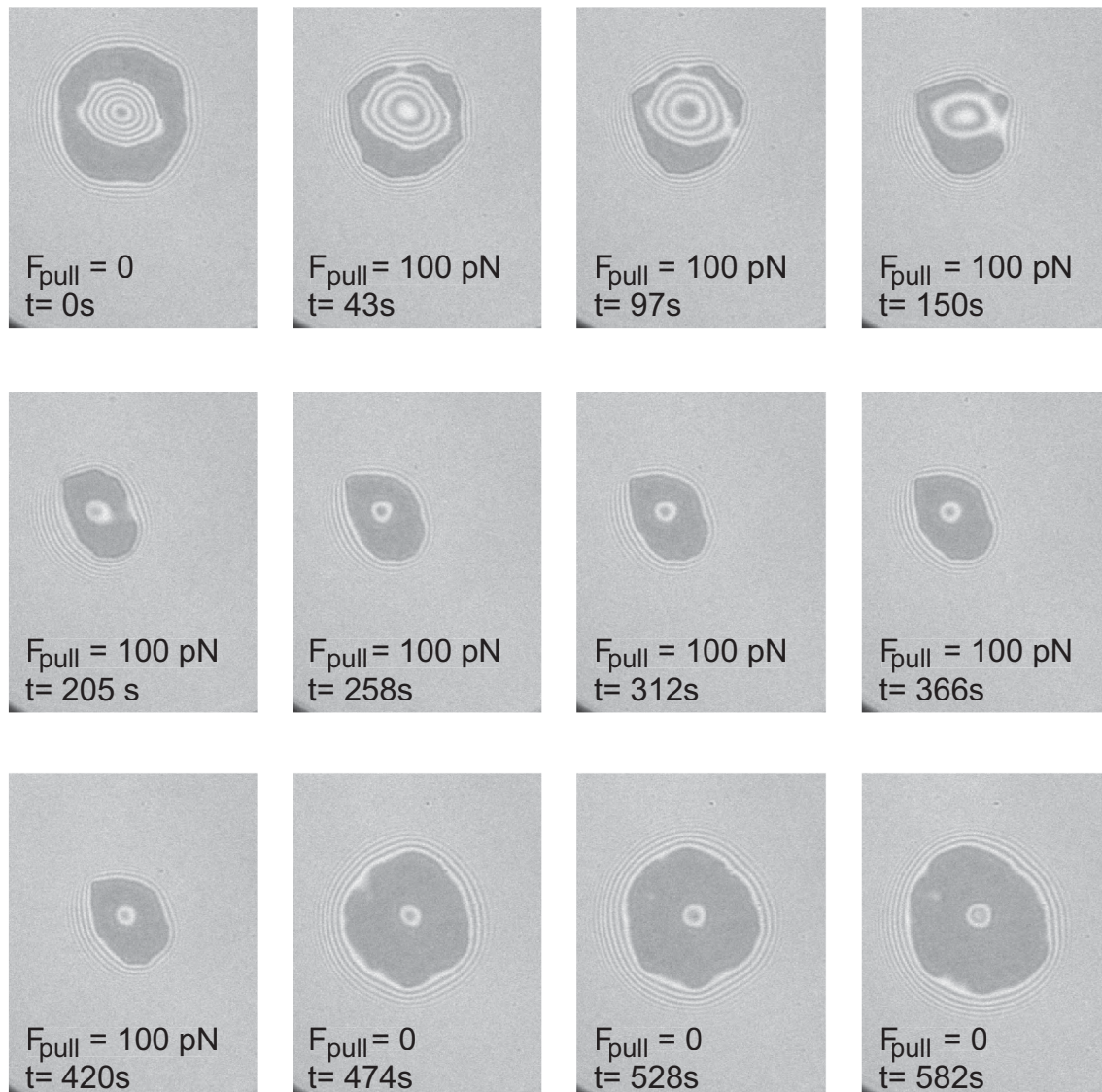


Figure 5.17: Time series of an unbinding experiment of a Sialyl-Lewis^X vesicle initially adhered to a substrate covered by E-selectin. In the first and the three last RICM micrographs the force pulling on the vesicle is zero, in all the other micrographs the force is 100 pN.

increases than decreases while the pulling force is acting on the vesicle. This observation may be attributed to the reduced undulations due to the increased membrane tension upon pulling. Since the undulations result in a repulsive interaction, their decrease may indeed lead to a larger adhesion area in the new steady state regime of a pulled vesicle. However, only further experiments will eventually show if this assumption is correct.

To estimate the force required to unbind the vesicles from the integrin/cellulose system, the line force f_{\perp} is expected to be a factor of 30 larger than for the vesicles on bilayers supported by bare glass, as determined in the previous chapter. The absolute force F_{\perp} is assumed to be at least about 300 times larger, since large parts of the contact line are pinned. Therefore pulling forces of 0.5...1 nN would be necessary to unbind those vesicles. To increase the magnetic tweezers pulling force accordingly (factor 100...500) would require either different paramagnetic beads with a higher dipole moment, or a different setup with a thicker iron core to obtain higher magnetic fields, or a distance d between the sample and the magnetic poles $d \ll 1$ mm. Another parameter that can be varied is the specific adhesion energy by either increasing the repeller concentration (cf. previous chapter), or by exchanging the receptor-ligand system to one with a smaller binding affinity. Increasing the amount of repellers in the vesicle for the RGD-integrin system did not allow to unbind the vesicles with the present tweezers setup.

Sialyl-Lewis^X-E-Selectin Receptor-Ligand Pair

Unbinding experiments using the present magnetic tweezers setup with the Sialyl-Lewis^X-E-selectin systems are expected to be more successful since the specific adhesion energy of these receptor-ligand pairs is by a factor of 100 smaller than for the RGD-integrins system (Vestweber and Blanks 1999). In the PhD thesis of Lorz (2003) a vesicle model system based on the Sialyl-Lewis^X-E-selectin binding is established. Fig. 5.17 shows an unbinding experiment on that system with magnetic tweezers. The strongly adhered adhesion domain unbinds continuously from the substrate while a pulling force is applied. If the force is released, the vesicle rebinds to the substrate, demonstrating that the unbinding is reversible and the detached receptor-ligand pairs are not destroyed or pulled out of the membrane.

In addition to the evaluation of the unbinding line force f_{\perp} and unbinding forces F_{\perp} , here an analysis of the decrease and increase of the adhesion area can be performed with high accuracy as shown in Fig. 5.18. The decrease of the adhesion area $A(t)$ can be described by an exponential decay with an offset or level A_1 which accounts for the remaining adhesion area, reminiscent of a steady state:

$$A(t) = A_0 \exp\left(-\frac{t}{\tau}\right) + A_1, \quad (5.6)$$

where $A_0 + A_1$ is the initial adhesion area, t is the time and τ the decay constant.

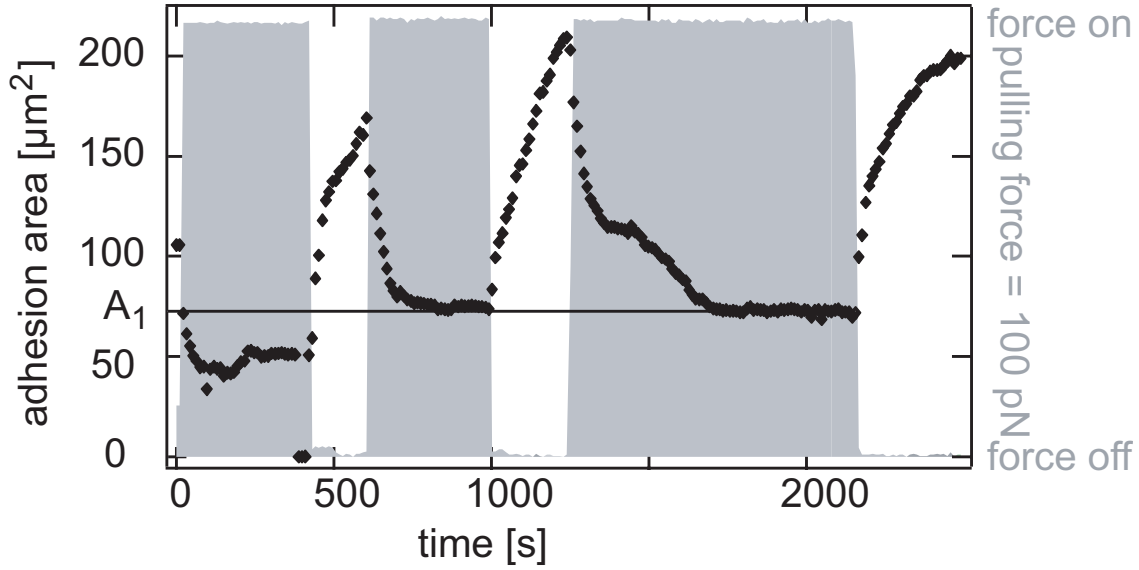


Figure 5.18: Adhesion area of a vesicle plotted versus time. The black symbols show the adhesion area of the vesicle, whereas the line A_1 indicates the area of the steady state for the unbinding. The gray rectangles indicate the intervals during which a constant pulling force of 100 pN is applied to the vesicle.

A detailed analysis of the obtained unbinding time constant τ as a function of the pulling force, the repeller, and the receptor concentrations is given in Lorz (2003).

5.5 Conclusions

We have developed a magnetic tweezers technique to unbind specifically adhered vesicles from substrates while monitoring the adhesion area with RICM. The substrate may for example mimic a target cell as shown in the previous chapters. The strength of the technique is the observation of the heterogeneous structure of the adhesion area as well as the in situ study of unbinding events of various pinning centers. In contrast to single molecule experiments, the adhesion domain can be studied in our approach. This is very important, since the amount of unbound receptor-ligand pairs as well as their geometric distribution is expected to have a drastic effect on the observed unbinding forces. For instance the membrane peeling zone may encounter focal contact sites. Furthermore, the method allows for a determination of the line force f_{\perp} and the unbinding force F_{\perp} of the pinning centers from the analysis of the deformation of the vesicle.

The constant unbinding line force f_{\perp} measured in the experiments, suggests that the distribution of the adhesion points on the substrate is rather homogeneous, whereas the unbinding force F_{\perp} per PC depends on the contour length per pin-

ning center s_{PC} . The constant value f_{\perp} allows for a comparison to the force rate measurements by Prechtel et al. (2002), where rather constant unbinding forces of $\tilde{F}_{\perp} \geq 100$ pN are obtained for one fixed force rate. Since in these experiments many receptor-ligand pairs ($\sim 10^3 \dots 10^4$ per μm^2) are acting together, only a small scatter in the force occurs due to a variation of the number of receptor-ligand pairs. In contrast, in our experiments we assume to have a small number of binding sites ($\sim 3 \dots 10$ per pinning center, cf. chapter 4). Therefore the absolute unbinding force F_{\perp} exhibits a large variation if the number of binding pairs varies in the assumed limits. However, the line tension f_{\perp} , which is corrected with respect to the contour length s_{PC} , exhibits a constant value and has to be compared to the unbinding force F_{\perp} in experiments with many receptor-ligand pairs. Measurements with different forces would be necessary to validate the assumption, that f_{\perp} is increasing with higher force rates. Additionally, measurements with receptor-ligand pairs in the $10^3 \dots 10^4$ range would be a method to demonstrate the correctness of our assumptions.

The Silayl-Lewis^X-E-selectin system exhibits a receptor concentration of 900 receptors per μm^2 , modelling the concentration range found in cells. A nearly continuously peeling of the vesicle from the substrate can be observed. However, the decrease in adhesion area always approaches a steady state where no further unbinding is observed. This observation is very different from the results reported so far. Possibly, the rebinding plays a key role if the applied force is not increasing ($\dot{F}_{pull} = 0$). From the decreasing contact area induced by the applied pulling force, the binding kinetics of the system might become accessible. Additionally, first experiments with a changing pulling force are now underway, in order to study the effects on the unbinding dynamics.

5.6 Outlook

Shape Reconstruction

With the laser scanning confocal microscope (LSCM) the three-dimensional shape of vesicles adhering to a substrate can be observed. By adaption of the magnetic tweezers setup to the LSCM the shape variation of the vesicle upon an applied vertical lift force can be investigated (cf. Fig. 5.19). By changing the pulling force we hope to understand how the force is transduced by the vesicle and how it is acting on the receptor-ligand pairs. Does for example a leverage, as proposed by Guttenberg et al. (2000) play a role for the enforced unbinding? The overall shape of the pulled vesicles might allow to test the validity of theoretical models. This could result in a more precise theoretical description of the unbinding process. A comparison to theoretical calculations based on the finite element technique in terms of elasticity has been discussed recently (A. Smith and U. Seifert private communication).

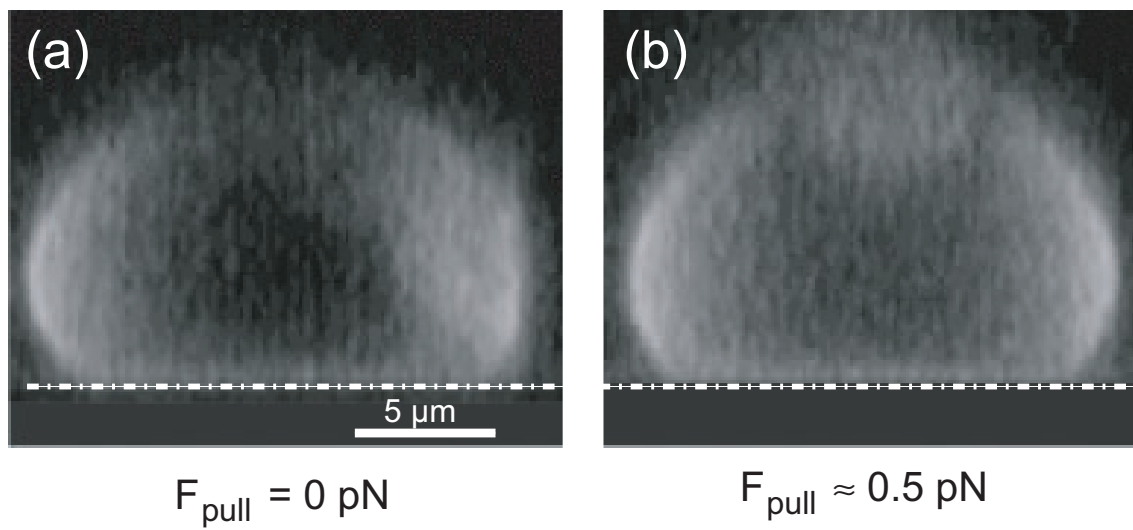


Figure 5.19: Three-dimensional shape of a fluorescently labelled vesicle reconstructed from a confocal microscopy series. a) The vesicle adheres specifically to a substrate without any applied lift force ($F_{\text{pull}} = 0$). b) A vertical pulling force $F_{\text{pull}} = 0.5 \text{ pN}$ is acting on the vesicle.

Appendix

Giant Vesicle Preparation

Giant vesicles were prepared following the electroswelling method of Dimitrov and Angelova (1988). Lipids were dissolved in chloroform (1 mg ml^{-1}). Some droplets ($\approx 10 \dots 50 \mu\text{l}$) were deposited onto indium-tin-oxide (ITO) electrodes and stored in a vacuum chamber for at least 12 h so that the solvent was evaporated completely. The swelling chamber consisted of two teflon wells, pressed together by screws. The chamber was filled with 2 ml of a 170 mM sucrose solution and the ITO electrodes were opposed to each other as in a capacitor. Then an AC electric current of 10 Hz and 1 V was applied for 2 h while the whole chamber was kept at $40 \text{ }^\circ\text{C}$. The giant vesicles formed by a self-assembled process. Before the next use, the electrodes and the chambers were washed carefully by ultra-sonication for 15 min in 2 mol% Hellmanex (Hellma, Germany) solution. To get rid of the detergent, they were rinsed 10 times with millipore water and ultra-sonicated in pure millipore water for 15 minutes. The washing step with the millipore water was repeated a second time.

Phosphate Analysis

The concentration of phosphate following (Fiske and SubbaRow 1925, Bartlett 1958) is determined from the amount of reduced ammonium-molybdate, which leads to an increase in the light absorbtion at 797 nm. The phosphate analysis is performed with reference solutions in order to calibrate the measured absorbance to molar contents, with a dilution series of a 1 mM KH_2PO_4 to 0, 1 μM , 10 μM , 100 μM , 500 μM and 1 mM of phosphate.

The different liquids are pipetted into test tubes and heated at $180 \text{ }^\circ\text{C}$ for 5 minutes in order to evaporate the liquid. Successively 0.3 ml perchloric acid (H_2SO_4 , 70%, Sigma, Germany) is added to each tube and all tubes - closed with a marble to prevent evaporation - are kept at $180 \text{ }^\circ\text{C}$ for 2 h. After the samples have cooled to room temperature 1.4 ml H_2O and 0.2 ml NH_4 -molybdate of a 2.5% stock solution is added (in total 0.3 wt.% NH_4 -molybdate). The solutions are then well mixed and 0.2 ml ascorbic acid solution of a freshly prepared 10 wt.% solution is added (in total 1 wt.% ascorbic acid). By heating the test tubes to $100 \text{ }^\circ\text{C}$ for

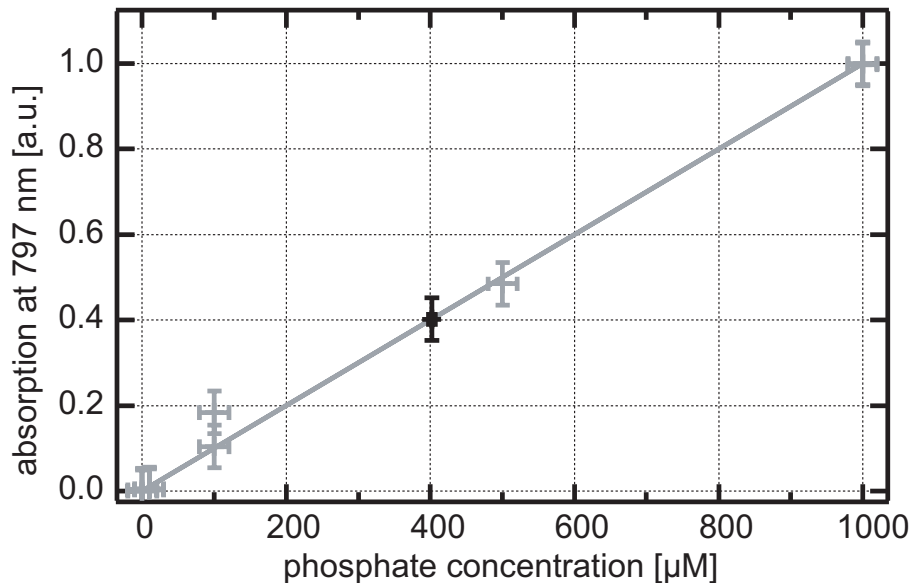


Figure 5.20: The linear dependence of the light absorption at 797 nm to the phosphor content is shown in the gray calibration curve. The black marker is the absorbance of the measured integrin vesicle solution indicating a phosphate amount of $(402 \pm 5) \mu\text{M}$.

6 minutes a clear blue solution appears in the tubes where phosphate is present. The absorbance for the different dilutions is measured in a 1 cm cuvette in an UV-spectroscopy (797 nm). It is proportional to the concentration from $1 \mu\text{M}$ to 1 mM of phosphate, as shown in Fig. 5.20. From this linear dependence the phosphate concentration of the studied sample can be calculated. For the integrin vesicle solution a concentration $c_{\text{phosphate}} = (402 \pm 5) \mu\text{M}$ was determined.

Buffers

Buffer A 150 mM NaCl, 20 mM TRIS, 1 mM NaN_3 , 1 mM CaCl_2 , 1 mM MgCl_2 at pH 7.3 (dialyzed with HCl).

Buffer A1 250 mM NaCl, 20 mM TRIS, 1 mM NaN_3 , 1 mM CaCl_2 , 1 mM MgCl_2 at pH 7.3 (dialyzed with HCl).

Buffer B 100 mM NaCl, 10 mM HEPES, 1 mM NaN_3 , 1 mM CaCl_2 at pH 7.3 and 205 mOsm (dialyzed with NOH).

Buffer C 100 mM NaCl, 10 mM TRIS, 1 mM NaN_3 , at pH 7.3 and 205 mOsm (dialyzed with NOH).

Used Symbols

α	contact angle
A	area
A_H	Hamakar constant
χ	second virial term
d	distance magnetic pole to sample
δ	membrane thickness
$\Delta\rho$	difference in density
F_{pull}	pulling force
F_{\perp}	unbinding force
f_{\perp}	vertical line force
γ	membrane tension
G	gravity
g	acceleration due to gravity
h	height
I	intensity
κ	bending stiffness of the membrane
$k_B T$	thermal energy
λ	wavelength
n	refractive index
$P(h)$	probability distribution
R	resistance
R_g	radius of gyration
s	contour length
t	time
$V(h)$	interaction energy per unit area
V_{He}	Helfrich potential
W	energy
W_{ad}	adhesion force per length
w	root mean square (rms) width
ξ_{\parallel}	in-plane correlation length

Abbreviations

AC	alternative current
BSA	album bovine serum
CD41A	Antibody against integrin $\alpha_{IIb}\beta_3$ mouse monoclonal anti-human CD41A
DEPC	1,2-dielaidoyl-sn-glycero-3-phosphocholine,
DMPC	1,2-dimyristoyl-sn-glycero-3-phosphocholine,
DMPE	1,2-dimyristoyl-sn-glycero-3-phosphoethanolamine,
DMPG	1,2-dimyristoyl-sn-glycero-3-phosphatidylglycerol,
DOPC	1,2-dioleoyl-sn-glycero-3-phosphocholine,
ECM	extracellular matrix
FAS	focal adhesion sites
HEPES	4-(2-Hydroxyethyl)piperazine-1-ethanesulfonic acid
ITO	indium tin oxide
LL	Lipowsky and Leibler (1986)
LCSM	laser scanning confocal microscope
N.A.	numerical aperture
NBD	6-(N-(7-Nitrobenz-2-oxa-1,3-diazol-4-yl)amino)hexanoic acid
PC-NBD	1-Oleoyl-2-[12-[(7-nitro-2-1,3-benzoxadiazol-4-yl)amino]dodecanoyl]-sn-Glycero-3-Phosphocholine
PEG	polyethylene glycol
ODTMS	octadecyltrimethoxysilane,
PC	pinning center
RB	Bruinsma (1995)
RICM	reflection interference contrast microscope
RGD	amino acid sequence Arg-Gly-Asp
SL	Seifert and Lipowsky (1990)
TAMRA	5-(and-6)-carboxy-tetramethylrhodamine succinimidyl ester
TMSC	trimethylsilyl cellulose
TRIS	Tris-(hydroxymethyl)-aminomethane
vdW	van der Waals
w/v	weight per volume
wt.	weight

Bibliography

- Abercrombie, A. W. and Ambrose, E. J. (1958). Interference reflection microscopy studies of cell contacts in tissue culture, *Exp. Cell Res.* **15**: 332–345.
- Adam, G., Lauger, P. and Stark, G. (1995). *Physikalische Chemie und Biophysik*, 3 edn, Springer-Verlag.
- Alberts, B., Bray, D., Lewis, J., Raff, M., Roberts, K. and Watson, J. D. (1994). *Molecular Biology of the Cell*, 4 edn, Garland Publishing, Inc., New York.
- Albertsdorfer, A., Feder, T. and Sackmann, E. (1997). Adhesion-induced domain formation by interplay of long-range repulsion and short-range attraction force: A model membrane study, *Biophys. J.* **73**(1): 245–257.
- Almeida, P. and Vaz, W. (1995). *Lateral diffusion in membranes.*, Vol. 1A of *Handbook of Biological Physics*, 1 edn, Elsevier Science B.V., Amsterdam, chapter 6, pp. 305–358.
- Alon, R., Hammer, D. A. and Springer, T. A. (1995). Lifetime of the p-selectin-carbohydrate bond and its response to tensile force in hydrodynamic flow., *Nature* **374**: 539–542.
- Axelrod, D., Koppel, D., Schlessinger, J., Elson, E. and Webb, W. (1976). Mobility measurements by analysis of fluorescence photobleaching recovery kinetics, *Biophys. J.* **16**: 1055–1069.
- Baekmark, T., Elender, G., Lasic, D. and Sackmann, E. (1995). Conformational transitions of mixed monolayers of phospholipids and poly(ethylene oxide) lipopolymers and interaction forces with solid surfaces, *Langmuir* **11**: 3975–3987.
- Bartlett, G. (1958). Phosphorus assay in column chromatography, *J. Biol. Chem.* **234**(3): 466–468.
- Bayer, E. (1990). *Avidin-Biotin Technology*, Vol. 184 of *Methods in Enzymology*, Academic Press, Inc.

- Bell, G. (1978). Models for the specific adhesion of cells to cells, *Science* **200**: 618–627.
- Bell, G., Dembo, M. and Bongrand, P. (1984). Competition between nonspecific repulsion and specific bonding, *Biophys. J.* **45**(6): 1051–64.
- Bernard, A., Delamarche, E., Schmid, H., Michel, B., Bosshard, H. and Biebuyck, H. (1998). Printing patterns of proteins, *Langmuir* **14**(9): 2225–2229.
- Bogan, B. and Thorn, K. (1998). Anatomy of hot spots in protein interfaces, *J. Mol. Biol.* **280**: 1–9.
- Böhm, J. (2001). *Identifikation makromolekularer Komplexe in Elektronentomogrammen eiseingebetteter Phantomzellen*, Dissertation, Physikdepartment, Technische Universität München.
- Bongrand, P. (1999). Ligand-receptor interactions, *Reports on Progress in Physics* **62**(6): 921–968.
- Born, M. and Wolff, E. (1999). *Principles of Optics*, 7 edn, Cambridge University Press, Cambridge.
- Boulbitch, A., Guttenberg, Z. and Sackmann, E. (2001). Kinetics of membrane adhesion mediated by ligand-receptor interaction studied with a biomimetic system, *Biophys. J.* **81**(5): 2743–2751.
- Boxer, S. (2000). Molecular transport and organization in supported lipid membranes, *Curr. Op. Chem. Biol.* **4**: 704–709.
- Bradford, M. (1976). A rapid and sensitive method for the quantitation of microgram quantities of protein utilizing the principle of protein-dye binding, *Anal. Biochem.* **72**: 248–254.
- Brian, A. A. and McConnell, H. M. (1984). Allogenic stimulation of cyto-toxic T-cells by supported planar membranes, *Proc. Nat. Acad. Sci. USA* **81**: 6159–6163.
- Brochard-Wyart, F. and de Gennes, P. (2002). Adhesion induced by mobile binders: Dynamics, *Proc. Nat. Acad. Sci. USA* **99**(12): 7854–7859.
- Bruinsma, R. (1995). *Adhesion and Rolling of Leukocytes. A Physical Model. Proceedings of the NATO Advanced Institute of Physics and Biomaterials.*, NATO Advanced Study Institute Series B: Physics, Kluwer, p. 611.
- Bruinsma, R., Behrisch, A. and Sackmann, E. (2000). Adhesive switching of membranes: experiment and theory, *Phys. Rev. E* **61**(4): 4253–4267.

- Buck, C. and Horwitz, A. (1987). Cell surface receptors for extracellular matrix molecules, *Annu. Rev. Cell Biol.* **3**: 179–205.
- Castro-Roman, F., Porte, G. and Ligoure, C. (1999). Renormalization of Helfrich's interactions between fluid membranes in a lyotropic lamellar phase by addition of amphiphilic copolymers, *Phys. Rev. Lett.* **82**(1): 109–112.
- Cevc, G. and Marsh, D. (1987). *Phospholipid Bilayers*, John Wiley & Sons, New York.
- Chan, P., Lawrence, M., Dustin, M., Ferguson, L., Golan, D. and Springer, T. (1991). Influence of receptor lateral mobility on adhesion strengthening between membranes containing LFA-3 and CD2, *J. Cell Biol.* **115**(1): 245–255.
- Chazotte, B. and Hackenbrock, C. (1988). The multicollisional, obstructed, long-range diffusional nature of mitochondrial electron transport, *J. Biol. Chem.* **263**(28): 14359–14367.
- Cheng, S., Craig, W., Mullen, D., Tschopp, J., Dixon, D. and Pierschbacher, M. (1994). Design and synthesis of novel cyclic rgd-containing peptides as highly potent and selective integrin $\alpha_{IIb}\beta_3$ antagonists, *J. Med. Chem.* **37**: 1–8.
- Clark, E. and Brugge, J. S. (1995). Integrins and signal transduction pathways: the road taken., *Science* **268**: 233–238.
- Craig, W., Cheng, S., Mullen, D., Blevitt, J. and Pierschenbacher, M. (1995). Concept and progress in the development of RGD-containing peptide pharmaceuticals, *Biopolymers (Peptide Science)* **37**: 157–175.
- Curtis, A. (1964). The mechanism of adhesion of cells to glass. a study by interference reflection microscopy, *J. Biol. Chem.* **20**: 199–215.
- David, F. and Leibler, S. (1990). Multicritical unbinding phenomena and nonlinear functional renormalization-group, *Phys. Rev. B* **41**(18): 12926–12929.
- deGennes, P. (1980). Conformations of polymers attached to an interface, *Macromolecules* **13**: 1069–1075.
- deGennes, P. (1985). Wetting: statics and dynamics, *Rev. Mod. Phys.* **57**(3): 827–863.
- Dembo, M., Torney, D., Saxman, K. and Hammer, D. (1988). The reaction-limited kinetics of membrane-to-surface adhesion and detachment, *Proc. Roy. Soc. London B* **234**(1247): 55–83.
- Dimitrov, D. and Angelova, M. (1988). Lipid swelling and liposome formation mediated by electric fields, *Bioelchem.* **19**(2): 323–336.

- Dustin, M. (1997). Adhesive bond dynamics in contacts between T lymphocytes and glass-supported planar bilayers reconstituted with the immunoglobulin related adhesion molecule CD58, *J. Biol. Chem.* **272**(225): 15782–15788.
- Dzyaloshinskii, I., Lifshitz, E. and Petaevskii, L. (1961). The general theory of van der Waals forces, *Adv. Phys.* **10**(38): 165–209.
- Erb, E., Tangemann, K., Bohrmann, B., Müller, B. and Engel, J. (1997). Integrin alpha IIb beta 3 reconstituted into lipid bilayers is nonclustered in its activated state but clusters after fibrinogen binding, *Biochemistry* **36**(24): 7395–7402.
- Evans, E. and Ritchie, K. (1997). Dynamic strength of molecular adhesion bonds, *Biophys. J.* **72**(4): 1541–1555.
- Evans, E. and Sackmann, E. (1988). Translational and rotational drag coefficients for a disk moving in a liquid membrane associated with a rigid substrate, *J. Fluid. Mech.* **194**: 553–561.
- Fahey, P. and Webb, W. (1978). Lateral diffusion in phospholipid bilayer membranes and multilamellar liquid crystals, *Biochemisry* **17**: 3046–3053.
- Fiske, C. and SubbaRow, Y. (1925). The colorimetric determination of phosphorus, *J. Biol. Chem.* **66**: 375.
- Fitzgerald, L., Leung, B. and Phillips, D. (1985). A method for purifying the platelet membrane glycoprotein IIB-IIIA complex, *Anal. Biochem.* **151**(1): 169–177.
- Florin, E., Moy, V. and Gaub, H. (1994). Adhesion forces between individual ligand-receptor pairs, *Science* **264**(5157): 415–417.
- Galla, H., Hartmann, W. and Sackmann, E. (1978). Lipid-protein-interaction in model membranes - binding of melittin to lecithin bilayer vesicles, *Ber. Bunsen. Phys. Chem.* **82**(9): 918–922.
- Gardner, J. M. and Hynes, R. O. (1985). Interaction of fibronectin with its receptor on platelets, *Anal. Biochem.* **42**: 439–448.
- Gennis, R. (1989). *Biomembranes Molecular Structure and Function*, 1 edn, Springer-Verlag, New York.
- Gingell, D. and Todd, I. (1979). Interference reflection microscopy: a quantitative theory for image interpretation and its application to cell-substratum separation measurements, *Biophys. J.* **26**: 507–526.
- Goennenwein, S., Tanaka, M., Hu, B., Moroder, L. and Sackmann, E. (2003). Functional incorporation of integrins into solid supported membranes on ultrathin films of cellulose - impact on adhesion, *in press Biophys. J.* .

- Gompper, G. and Kroll, D. (1989). Steric interactions in multimembrane systems - a monte-carlo study, *Europhys. Lett.* **9**(1): 59–64.
- Green, N. (1963). Avidin. 3. the nature of the biotin-binding site, *Biochem. J.* **89**(3): 599.
- Gritsch, S., Nollert, P., Jähnig, F. and Sackmann, E. (1998). Impedance spectroscopy of porin and gramicidin pores reconstituted into supported lipid bilayers on indium-tin-oxide electrodes, *Langmuir* **14**(11): 3118–3125.
- Gurrath, M., Müller, G., Kessler, H., Aumailley, M. and Timpl, R. (1992). Conformation/activity studies of rationally designed potent anti-adhesive RGD peptides, *Eur. J. Biochem.* **210**: 911–921.
- Guttenberg, Z. (2000). *Zelladhäsion als Benetzungsübergang: Mikrooptische und micromechanisch untersuchung eines biomimetischem Modellsystems*, Dissertation, Physikdepartment, Technische Universität München.
- Guttenberg, Z., Bausch, A., Hu, B., Bruinsam, R., Moroder, L. and Sackmann, E. (2000). Measuring ligand-receptor unbinding forces with magnetic beads: Molecular leverage, *Langmuir* **16**(23): 8984–8993.
- Guttenberg, Z., Lorz, B. and Sackmann, E. (2001). First-order transition between adhesion states in a system mimicking cell-tissue interaction, *Europhys. Lett.* **54**(6): 826–832.
- Hecht, E. (1987). *Optics*, 2 edn, Addison-Wesley Publishing Company, Inc., New York.
- Heilbronn, A. (1922). Eine neue methode zur bestimmung der viscosität lebender protoplasten, *Jahrb. wiss. Bot.* **61**: 284–338.
- Helfrich, W. (1978). Steric interaction of fluid membranes in multilayer systems, *Z. Naturforsch.* **33a**: 305–315.
- Heyse, S., Vogel, H., Sängler, M. and Sigrist, H. (1995). Covalent attachment of functionalized lipid bilayers to planar waveguides for measuring protein binding to biomimetic membranes, *Protein Science* **4**: 2532–2544.
- Hiergeist, C. and Lipowsky, R. (1996). Elastic properties of polymer-decorated membranes, *J. de Phys. II* **6**(10): 1465–1481.
- Hillebrandt, H. and Tanaka, M. (2001). Electrochemical characterization of self-assembled alkylsiloxane monolayers on indium-tin oxide (ITO) semiconductor electrodes, *J. Phys. Chem B* **105**(19): 4270–4276.

- Hillebrandt, H., Wiegand, G., Tanaka, M. and Sackmann, E. (1999). High electric resistance thin polymer/lipid composite systems on indium-tin-oxide (ITO) electrode-arrays, *Langmuir* **15**(24): 8451–8459.
- Hinner, B., Tempel, M., Sackmann, E., K.Kroy and Frey, E. (1998). Entanglement, elasticity, and viscous relaxation of actin solutions, *Phys. Rev. Lett.* **81**: 2614–2617.
- Horwitz, A. (1998). Integrine, *Spektrum der Wissenschaft* **1**: 86–94.
- Hovis, J. and Boxer, S. (2001). Patterning and composition arrays of supported lipid bilayers by microcontact printing, *Langmuir* **17**(11): 3400–3405.
- Hu, B. (2001). *Vesicle Adhesion via Interaction of Integrin and Cyclic-RGD-Lipopeptide: A Model of Cell Adhesion Processes*, Dissertation, Physikdepartment, Technische Universität München.
- Hu, B., Finsinger, D., Peter, K., Guttenberg, Z., Bärmann, M., Kessler, H., Escherich, A., Moroder, L., Böhm, J., Baumeister, W., Sui, S. and Sackmann, E. (2000). Intervesicle cross-linking with integrin alpha(IIb)beta(3) and cyclic-RGD-lipopeptide. A model of cell-adhesion processes, *Biochemistry* **39**(40): 12284–12294.
- Hynes, R. (1992). Integrins: Versatility, modulation, and signaling in cell adhesion, *Cell* **69**: 11–25.
- Israelachvili, J. N. (1991). *Intermolecular and Surface Forces*, 2 edn, Academic Press, London.
- Kalb, E., Frey, S. and Tamm, L. (1992). Formation of supported planar bilayers by fusion of vesicles to supported phospholipid monolayers, *Biochim. Biophys. Acta* **1103**: 307–316.
- Kantlehner, M., Finsinger, D., Meyer, J., Schaffner, P., Jonczyk, A., Diefenbach, B., Nies, B. and Kessler, H. (1999). Selective RGD-mediated adhesion of osteoblasts at surfaces of implants, *Angew. Chem. - Int. Ed.* **38**(4): 560–562.
- Keller, C., Glasmästar, K., Zhdanov, V. and Kasemo, B. (2000). Formation of supported membranes from vesicles, *Phys. Rev. Lett.* **84**(23): 5443–5446.
- Keller, S., Pitcher, W., Huestis, W. and McConell, H. (1998). Red blood cell lipids from immiscible liquids, *Phys. Rev. Lett.* **81**(22): 5019–5022.
- Kenworthy, A., Hristova, K., Needham, D. and McIntosh, T. (1995). Range and magnitude of the steric pressure between bilayers containing phospholipids with covalently attached poly(ethylene glycol), *Biophys. J.* **68**: 1921–1936.

- Kessler, H., Grantias, R. and Mullen, G. (1996). Conformation of cyclic peptides. Principle concepts and the design of selectivity and superactivity in bioactive sequences by "spatial screening", *Pure and Applied Chemistry* **68**: 1201.
- Kloboucek, A., Behrisch, A., Faix, J. and Sackmann, E. (1999). Adhesion-induced receptor segregation and adhesion plaque formation: A model membrane study, *Biophys. J.* **77**: 2311–2328.
- Komura, S. and Andelman, D. (2002). The unbinding transition of mixed fluid membranes, *submitted to Europhys. Lett.* .
- Kucik, D., Elson, E. and Scheetz, M. (1999). Weak dependence of mobility of membrane protein aggregates on aggregate size supports a viscous model of retardation of diffusion, *Biophys. J.* **76**: 314–322.
- Kühner, M. (1994). *Photobleichuntersuchungen der lateralen diffusion in lipidschichten auf polymerem und von polymeren in lipidschichten*, Diplomarbeit, Physikdepartment, Technische Universität München.
- Kühner, M. and Sackmann, E. (1996). Ultrathin hydrated dextran films grafted on glass: preparation and characterization of structural, viscous and elastic properties by quantitative microinterferometry, *Langmuir* **12**: 4866–4876.
- Kühner, M., Tampé, R. and Sackmann, E. (1994). Lipid mono- and bilayer supported on polymer films: composite polymer-lipid films on solid substrates, *Biophys. J.* **76**: 217–226.
- Landau, L. D. and Lifschitz, E. M. (1970). *Lehrbuch der theoretischen Physik, Band VII (Elastizitätstheorie)*, Akademie-Verlag, Berlin.
- Lasic, D. (1993). *Liposomes, From Physics to Applications*, Elsevier, Amsterdam.
- Leckband, D. (1995). The surface forces apparatus - a tool for probing molecular protein interactions, *Nature* **376**: 617–618.
- Leckband, D. and Israelachvili, J. (2001). Intermolecular forces in biology, *Quarterly Reviews of Biophysics* **34**(2): 105–267.
- Lee, G., Zhang, F., Ishihara, A., McNeil, C. and Jacobson, K. (1993). Unconfined lateral diffusion and an estimate of pericellular matrix viscosity revealed by measuring the mobility of gold-tagged lipids, *J. Biol. Chem.* **120**: 25–35.
- Leibler, S. and Lipowsky, R. (1987). Complete unbinding and quasi-long-range order in lamellar phases, *Phys. Rev. B* **35**: 7004.
- Lipowsky, R. (1989). *Vesicles and Biomebranes*, Vol. 23 of *Encyclopedia of Applied Physics*, Wiley-VCH Verlag GmbH, pp. 199–222.

- Lipowsky, R. and Leibler, S. (1986). Unbinding transitions of interacting membranes, *Phys. Rev. Lett.* **56**(23): 2541–2544.
- Lipowsky, R. and Zielinska, B. (1989). Binding and unbinding of lipid membranes: A monte carlo study, *Phys. Rev. Lett.* **62**(13): 1572–1575.
- Lodish, H., Berk, A., Zipursky, S. L., Matwudaira, P., Baltimore, D. and Darnell, J. (2000). *Molecular Cell Biology*, 4 edn, W.H. Freeman and Company.
- Lorz, B. (2003). *In preparation*, Dissertation, Physikdepartment, Technische Universität München.
- Lorz, B., Simson, R., Nardi, J. and Sackmann, E. (2000). Weakly adhering vesicles in shear flow: Tanktreading and anomalous lift force, *Europhys. Lett.* **51**(4): 468–474.
- Lutz, R., Mitchell, L. and Chakrin, L. (1973). *Physical-Chemical factors in mucus rheology*, Rheology of Biological Systems, Thomas Publications, Springfield, Illinois, pp. 119–157.
- Majewski, J., Kuhl, T., Kjaer, K., Gerstenberg, M., Als-Nielsen, J., Israelachvili, J. and Smith, G. (1998). X-ray synchrotron study of pacing and protrusions of polymer-lipid monolayers at the air-water interface, *J. Am. Chem. Soc.* **120**: 1469–1473.
- Marchi-Artzner, V., Lorz, B., Hellerer, U., Kantlehner, M., Kessler, H. and Sackmann, E. (2001). Selective adhesion of endothelial cells to artificial membranes with a synthetic RGD-lipopeptide, *Chem.-Eur. J.* **7**(5): 1095–1101.
- Marra, J. and Israelachvili, J. (1985). Direct measurements of forces between phosphatidylcholine and phosphatidylethanolamine bilayers in aqueous-electrolyte solutions, *Biochem.* **24**(17): 4608–4618.
- Mehta, A., Rief, M., Spudich, J., Smith, D. and Simmons, R. (1999). Single-molecule biomechanics with optical methods, *Science* **283**: 1689–1695.
- Merkel, R. (2001). Force spectroscopy on single passive biomolecules and single biomolecular bonds, *Phys. Rep.* **346**(5): 344–385.
- Merkel, R., Nassoy, P., Leung, A., Ritchie, K. and Evans, E. (1999). Energy landscapes of receptor-ligand bonds explored with dynamic force spectroscopy, *Nature* **397**: 50–53.
- Merkel, R., Sackmann, E. and Evans, E. (1989). Molecular friction and epitactic coupling between monolayers in supported bilayers, *J. de Phys.* **50**(12): 1535–1555.

- Milner, S. and Roux, D. (1992). Flory theory of the unbinding transition, *J. de Phys. I* **2**(9): 1741–1754.
- Mooney, J., Hunt, A., J.R., M., Liberko, C., D.M., W. and Rogers, C. (1996). Patterning of functional antibodies and other proteins by photolithography of silane monolayers, *Proc. Nat. Acad. Sci. USA* **93**(22): 12287–12291.
- Müller, B., Zerwes, H., Tangemann, K., Peter, J. and Engel, J. (1993). 2-step binding mechanism of fibrinogen to alpha IIb beta 3 integrin reconstituted into planar lipid bilayers, *J. Biol. Chem.* **268**(9): 6800–6808.
- Mutz, M. and Helfrich, W. (1989). Unbinding transition of a biological model membrane, *Phys. Rev. Lett.* **62**(24): 2881–2884.
- Netz, R. and Pincus, P. (1995). Inhomogeneous fluid membranes: Segregation, ordering, and effective rigidity, *Phys. Rev. E* **52**(4): 4114–4128.
- Netz, R. R. (1995). Complete unbinding of fluid membranes in the presence of short-ranged forces, *Phys. Rev. E* **51**(3): 2286–2294.
- Nielsen, M., Thewalt, J., Miao, L., Ipsen, J., Bloom, M., Zuckermann, M. and Mouritsen, O. (2000). Sterol evolution and the physics of membranes, *Europhys. Lett.* **52**(3): 368–374.
- Nissen, J. (2001). *Über das Benetzungsverhalten von Phospholipidmembranen auf glatten und strukturierten Oberflächen*, Dissertation, Physikdepartment, Technische Universität München.
- Pawley, J. (1995). *Handbook of Biological Confocal Microscopy*, Plenum Press, New York.
- Peters, R. and Cherry, R. (1952). Lateral and rotational diffusion of bacteriorhodopsin in lipid bilayers: Experimental test of the Saffman-Delbrück equations, *Proc. Nat. Acad. Sci. USA* **79**: 4317–4321.
- Pierschbacher, M. and Ruoslahti, E. (1984). Cell attachment activity of fibronectin can be duplicated by small synthetic fragments of the molecule, *Nature* **309**: 30–33.
- Ploem, J. (1975). *Reflection Contrast microscopy as a tool for investigation of the attachment of living cells to a glass surface*, Mononuclear Phagocytes in Immunity, Infection and Pathology, Blackwell Scientific Publications, Oxford.
- Pohl, R. W. (1969). *Mechanik, Akustik und Wärmelehre*, 17. edn, Springer-Verlag, Berlin.

- Poo, M. and Cone, R. (1974). Lateral diffusion of rhodopsin in photoreceptor membrane, *Nature* **247**: 438–441.
- Prechtel, K., Bausch, A., Marchi-Artzner, V., Kantlehner, M., Kessler, H. and Merkel, R. (2002). Dynamic force spectroscopy to probe adhesion strength of living cells, *Phys. Rev. Lett.* **89**(2): 028101.
- Rädler, J. O. and Sackmann, E. (1992). On the measurement of weak repulsive and frictional colloidal forces by reflection interference contrast microscopy, *Langmuir* **8**: 848–853.
- Rädler, J. O. and Sackmann, E. (1993). Imaging optical thicknesses and separation distances of phospholipid vesicles at solid surfaces, *J. Phys. II France* **3**(5): 727–748.
- Rädler, J. O. and Sackmann, E. (1997). Functionalization of solids by ultrathin soft polymer films and polymer/lipid film composites: modelling of cell surfaces and cell recognition processes, *Langmuir* **8**: 848–853.
- Rehfeldt, F. and Tanaka, M. (2003). Hydration forces in ultrathin films of cellulose, *Langmuir* **19**(5): 1467–1473.
- Renault, J., Bernard, A., Juncker, D., Michel, B., Bosshard, H. and Delamarche, E. (2002). Fabricating microarrays of functional proteins using affinity contact printing, *Ang. Chemie - Int. Ed.* **41**(13): 2320–2323.
- Ruoslahti, E. (1996). RGD and other recognition sequences for integrins, *Ann. Rev. Cell Dev. Biol.* **12**: 697–715.
- Sackmann, E. (1994). Membrane bending energy concept of vesicle-shape and cell-shape and shape-transitions, *FEBS Lett* **346**: 3–16.
- Sackmann, E. (1996). Supported membranes: Scientific and practical applications, *Science* **271**: 43–48.
- Sackmann, E. and Bruinsma, R. (2002). Cell adhesion as wetting transition?, *ChemPhysChem* **3**: 262–269.
- Sackmann, E. and Tanaka, M. (2000). Supported membranes on soft polymer cushions: fabrication, characterization and applications, *Trends Biotechnol.* **18**: 58–64.
- Saffman, P. and Delbrück, M. (1975). Brownian motion in biological membranes, *Proc. Nat. Acad. Sci. USA* **72**(8): 3111–3113.
- Safinya, C., Roux, D., Smith, G., Sinha, S., Dimon, P., Clark, N. and Bellocq, A. (1986). Steric interactions in a model multimembrane system - a synchrotron x-ray study, *Phys. Rev. Lett.* **57**(21): 2718–2721.

- Salafsky, J., Groves, J. and Boxer, S. (1996). Architecture and function of membrane proteins in planar supported bilayers: A study with photosynthetic reaction centers, *Biochemistry* **35**(47): 14773–14781.
- Scalettar, B. and Abney, J. R. (1991). Molecular crowding and protein diffusion in biological membranes, *Comments Mol. Cell. Biophys.* **7**(2): 79–107.
- Schaub, M., Wenz, G., Wegner, G., Stein, A. and Klemm, D. (1993). Ultrathin films of cellulose on silicon wafers, *Advanced Materials* **5**: 919–922.
- Schilling, J. (1999). *Entwicklung einer Echtzeit-Bildverarbeitungssoftware und digitaler Videoaufnahmetechnik zur quantitativen Mikrorheometrie von Aktin-Netzwerken*, Diplomarbeit, Physikdepartment, Technische Universität München.
- Schilling, J. (2003). *In preparation*, Dissertation, Physikdepartment, Technische Universität München.
- Schmitt, L., Dietrich, C. and Tampé, R. (1994). Synthesis and characterization of chelator-lipids for reversible immobilization of engineered proteins at self-assembled lipid interfaces, *J. Am. Chem. Soc.* **116**(19): 8485–8491.
- Seifert, U. (1995). Self-consistent theory of bound vesicles, *Phys. Rev. Lett.* **74**(25): 5060–5063.
- Seifert, U. (2000). Rupture of multiple parallel molecular bonds under dynamic loading, *Phys. Rev. Lett.* **84**(12): 2750–2753.
- Seifert, U. and Lipowsky, R. (1990). Adhesion of vesicles, *Phys. Rev. A* **42**: 4768–4771.
- Sengupta, K., Schilling, J., Marx, S., Fischer, M., Bacher, A. and Sackmann, E. (2003). Mimicking tissue surfaces by supported membrane coupled ultra-thin layer of hyaluronic acid, *Langmuir* **19**(5): 1775–1781.
- Sigl, H., Brink, G., Schulze, M., Wegener, G. and Sackmann, E. (1997). Assembly of polymer/lipid composite films on solids based on hairy rod LB-films, *Eur. Biophys. J.* **25**: 249–259.
- Simson, D. A., Stringl, M., Hohenadl, M. and Merkel, R. (1999). Statistical breakage of single protein A-IgG bonds reveals crossover from spontaneous to force-induced bond dissociation, *Phys. Rev. Lett.* **83**: 652–655.
- Singer, S. and Nicolson, G. (1972). The fluid mosaic model of the structure of cell membranes, *Science* **175**: 720–731.

- Sivasankar, S., Subramaniam, S. and Leckband, D. (1998). Direct molecular level measurements of the electrostatic properties of a protein surface, *Proc. Nat. Acad. Sci. USA* **95**(22): 12961–12966.
- Soumpasis, D. (1983). Theoretical analysis of fluorescence photobleaching recovery experiments, *Biophys. J.* **41**: 95–97.
- Spinger, T. (1994). Traffic signals for lymphocyte recirculation and leukocyte emigration - the multistep paradigm, *Cell* **76**: 301–314.
- Strick, T., Allemand, J.-F., Bensimon, D., Bensimon, A. and Croquette, V. (1996). The elasticity of a single supercoiled dna molecule, *Science* **271**: 1835–1837.
- Swain, P. and Andelman, D. (1999). The influence of substrate structure on membrane adhesion, *Langmuir* **15**(26): 8902–8914.
- Tamm, L. and McConnell, H. (1985). Supported phospholipid bilayers, *Biophys. J.* **47**: 105–113.
- Tank, D., Wu, E., Meers, P. and Webb, W. (1982). Lateral diffusion of gramicidin c in phospholipid multibilayers. effects of cholesterol and high gramicidin concentration, *Biophys. J.* **40**: 129–135.
- Tha, S., Shuster, J. and Goldsmith, H. (1986). Interaction forces between red cells agglutinated by antibody. II Measurements of hydrodynamic force of breakup, *Biophys. J.* **50**: 1117–1126.
- Tozeren, A., Sung, K., Sung, L., Dustin, M., Chan, P., Springer, T. and Chien, S. (1992). Micromanipulation of adhesion of a jurkat cell to a planar bilayer membrane containing lymphocyte function-associated antigen 3 molecules, *Biophys. J.* **116**: 997–1006.
- Vestweber, D. and Blanks, J. (1999). Mechanisms that regulate the function of the selectins and their ligands, *Physiol. Rev.* **79**(1): 181–213.
- Voet, D., Voet, J. and Pratt, W. (1995). *Biochemistry*, 2 edn, John Wiley & Sons, Inc., New York.
- Wagner, M. and Tamm, L. (2000). Tethered polymer-supported planar lipid bilayers for reconstitution of integral membrane proteins: Silane-polyethyleneglycol-lipid as a cushion and covalent linker, *Biophys. J.* **79**(3): 1400–1414.
- Wagner, M. and Tamm, L. (2001). Reconstituted syntaxin 1A/SNAP25 interacts with negatively charged lipids as measured by lateral diffusion in planar supported bilayers, *Biophys. J.* **81**(1): 266–275.

- Watts, T., Gaub, H. and McConnell, H. (1986). T-cell-mediated association of peptide antigen and major histocompatibility complex protein detected by energy transfer in an evanescent field, *Nature* **320**: 179–181.
- Wegner, G. (1992). Ultrathin films of polymers: architecture, characterization and properties, *Thin Solid Films* **216**: 105–116.
- Wegner, G. (1993). Control of molecular and supramolecular architecture of polymer, polymersystems and nanocomposites, *Mol. Cryst. Liq. Cryst.* **235**: 1–34.
- Weisel, G., Nagaswami, C., Vilaire, G. and Bennett, J. (1992). Examination of the platelet membrane glycoprotein IIb-IIIa complex and its interaction with fibrinogen and other ligands by electron microscopy, *J. Biol. Chem.* **267**: 16637–16643.
- Wiegand, G., Neumaier, K. and Sackmann, E. (1998). Microinterferometry: three-dimensional reconstruction of surface microtopography for thin-film and wetting studies by reflection interference contrast microscopy (RICM), *Applied Optics* **37**(29): 6892–6905.
- Wong, J., Park, C., Seitz, M. and Israelachvili, J. (1999). Polymer-cushioned bilayers. II. an investigation of interaction forces and fusion using the surface forces apparatus, *Biophys. J.* **77**(3): 1458–1468.
- Wyman, J. and Gill, S. (1990). *Binding and Linkage. Functional Chemistry of Biological Macromolecules*, University Books, Springfield.
- Xia, Y. and Whitesides, G. (1998). Soft lithography, *Angew. Chem. - Int. Ed.* **37**: 551–575.
- Yagi, K. (1961). The mechanical and colloidal properties of amoeba protoplasm and their relations to the mechanism of amoeboid movement, *Comp. Biochem. Physiol.* **3**: 73–91.
- Yamada, K. and Geiger, B. (1997). Molecular interactions in cell adhesion complexes, *Curr. Opin. Cell Biol.* **9**(1): 76–85.
- Zamir, E., Katz, M., Posen, Y., Erez, N., Yamada, K., Katz, B., Lin, S., Lin, D., Bershadsky, A., Kam, Z. and Geiger, B. (2000). Dynamics and segregation of cell-matrix adhesions in cultured fibroblasts, *Nature Cell Biology* **2**(4): 191–196.
- Ziemann, F. (1997). *Untersuchungen der lokalen viskoelastischen Eigenschaften von Zellen und Zellmodellen mit einem Magnetkugel-Mikrorheometer ("Magnetic Tweezers")*, Dissertation, Physikdepartment, Technische Universität München.

- Ziemann, F., Rädler, J. and Sackmann, E. (1994). Local measurements of viscoelastic moduli of entangled actin networks using an oscillating magnetic bead micro-rheometer, *Biophys. J.* **66**: 2210–2216.

Danke...

an alle, die zum Gelingen dieser Arbeit beigetragen haben.

Prof. Sackmann für seine Unterstützung – und die freie Hand, die er mir bei der Arbeit gelassen hat. Sein unerschöpflicher Vorrat an Ideen und seine Begeisterung für die Physik waren immer wieder neue Motivation.

Prof. Bruinsma für die Hilfe bei der Interpretation unserer Flickerergebnisse.

Ganz E22 für die vielen Tips, die Diskussions- und Hilfsbereitschaft, und natürlich für die vielen lustigen Aktionen und die erholsamen Kaffeepausen, die immer wieder Aufmunterung und Unterstützung bedeuteten. Das war ein tollen Rahmen für die Doktorarbeit!

Besonders erwähnen möchte ich:

Jörg Schilling, ohne den ich noch immer vor der Flickerauswertung und Computerproblemen sitzen würde.

Barbara Lorz für die kurzweiligen Magnetic Tweezers Experimente an ihrem System und die schöne Paris-Konferenz.

Wolfgang Feneberg, Manfred Keller, Alexander Roth und Jörg Uhde für die Hilfe mit dem Magnetic Tweezers Aufbau.

Olli Purruicker, Florian Rehfeldt und Motomu Tanaka für ihre Unterstützung an der Filmwaage und mit den Hairy Rods.

Zeno Guttenberg für die Einführung in die Vesikel- und Integrinpräparation.

Roman Zantl für Tips beim FRAP Messen und Auswerten.

Monika Rusp für die Präparation des Integrins und der Integrinvesikel.

Stefan Kauffmann für geduldige Beantwortung meiner Fragen in der Biochemie.

Michael Nicolaides für eine wunderbare Erkundung von Boston.

Felix Linke für die gute Banknachbarschaft.

Berenike Maier für das Wiederentdecken des Kletterns.

Jan Klügge, Michael Nicolaides, Olli Purruicker, Kheya Sengupta, und Ana Smith für das Korrekturlesen.

Ganz lieben Dank an meine Eltern, die mir eine sorgenfreie Studienzeit ermöglicht haben.

Und ein ganz spezielles Dankeschön natürlich an Sebastian.

Curriculum Vitae

Name	Stefanie Gönnerwein
Birth name	Marx
DOB	February 16 th , 1973
POB	Reutlingen
Marital status	married

since 09/99	PhD work at the Biophysics Group of Prof. E. Sackmann, Technische Universität München.
11/98-06/99	Final thesis at the Universität Konstanz.
1995-1996	Graduate studies in physics at the Universit Joseph Fourier, Grenoble, France.
1994-1999	Graduate studies in physics, mathematics and sports at the Universität Konstanz.
1992-1994	Undergraduate studies in physics, mathematics and sports at the Universität Stuttgart.
1983-1992	Friedrich-List-Gymnasium, Reutlingen.
1979-1983	Freie Evangelische Grundschule, Reutlingen.

List of Publications

- Marx, S., Schilling, J., Sackmann, E. and Bruinsma, R. (2002). Helfrich Repulsion and Dynamical Phase-Separation of Multi-Component Surfactant Bilayers. *Phys. Rev. Lett.* **88**(13): 1380102.
- Sengupta, K., Schilling, J., Marx, S., Fischer, M., Bacher, A., and Sackmann, E. (2003). Mimicking tissue surfaces by supported membrane coupled ultra-thin layer of hyaluronic acid, *Langmuir* **19**(5): 1775–1781.
- Dahmen, C., Janotta, A., Dimova-Malinovska, D., Marx, S., Jeschke, B., Nies, B., Kessler, H., and Stutzmann, M. (2003) Surface functionalization of amorphous silicon and silicon suboxides for biological applications, *Thin Solid Films* **427**(1-2): 201-207.
- Goennenwein, S., Tanaka, M., Hu, B., Moroder, L., and E. Sackmann (2003). Functional Incorporation of Integrins into Solid Supported Membranes on Ultrathin Films of Cellulose - Impact on Adhesion. *Biophys. J.* (accepted for publication).
- Schilling, J., Sengupta, K., Goennenwein, S., Bausch, A., and E. Sackmann (2003). Absolute Interfacial Distance Measurements by Dual Wavelength Reflection Interference Contrast Microscopy. (*submitted to Phys. Rev. E*).